2009

Decoherence In Semiconductor Solid-state Quantum Computers

Diego Valente
University of Central Florida

DECOHERENCE IN SEMICONDUCTOR SOLID-STATE QUANTUM COMPUTERS

by

DIEGO CASTELO BRANCO VALENTE
M.Sc. Pontifical Catholic University of Rio de Janeiro, 2004
B.Eng. Pontifical Catholic University of Rio de Janeiro, 2002

A dissertation submitted in partial fulfillment of the requirements
for the degree of Doctor of Philosophy
in the Department of Physics
in the College of Sciences
at the University of Central Florida
Orlando, Florida

Fall Term
2009

Major Professor: Eduardo R. Mucciolo

ABSTRACT

In this dissertation we discuss decoherence in charge qubits formed by multiple lateral quantum dots in the framework of the spin-boson model and the Born-Markov approximation. We consider the intrinsic decoherence caused by the coupling to bulk phonon modes and electromagnetic environmental fluctuations. In the case of decoherence caused by phonon coupling, two distinct quantum dot configurations are studied and proposed as setups that mitigate its nocive effects : (i) Three quantum dots in a ring geometry with one excess electron in total and (ii) arrays of quantum dots where the computational basis states form multipole charge configurations. For the three-dot qubit, we demonstrate the possibility of performing one- and two-qubit operations by solely tuning gate voltages. Compared to a previous proposal involving a linear three-dot spin qubit, the three-dot charge qubit allows for less overhead on two-qubit operations. For small interdot tunnel amplitudes, the three-dot qubits have Q factors much higher than those obtained for double-dot systems. The high-multipole dot configurations also show a substantial decrease in decoherence at low operation frequencies when compared to the double-dot qubit. We also discuss decoherence due to electromagnetic fluctuations in charge qubits formed by two lateral quantum dots. We use effective circuit models to evaluate correlations of voltage fluctuations in the qubit setup. These correlations allows us to estimate energy (T_1) and phase (T_2) relaxation times of the the qubit system. We also discuss the dependence the quality factor Q shows with respect to parameters of the setup, such as temperature and capacitive coupling between the electrodes.

To my parents Myrthes and Geraldo, for always encouraging and believing in me.

ACKNOWLEDGMENTS

I would like to thank my parents, Myrthes and Geraldo, and my family for always supporting me in my career. It has not always been easy being away from you for such large stretches of time, but you still live in my heart.

During my years here in Orlando, I have been lucky to meet an important person in my life, Devoney. Your emotional support and your patience and understanding specially during this last year have inspired me to keep working hard even in the hardest days. I am happy to have also been "adopted" by your family here, who was also always very encouraging and helped make me feel at home even though I was away from home.

I will always be indebted to my adviser, Prof. Eduardo Mucciolo, for his relentless support during our years working together. You have been more than an adviser to me, but also a mentor and a friend with whom I could count on to listen to me but also who was always honest with me in every moment. It was a true honor to work with you for these past years.

To my friends here at UCF, Chris, Jorge, and Sabine, what can I say! I will never forget the times I was able to count on your help because I needed rides or needed help moving, or just when we would just hang out for a few beers and a friendly pool match.

I would like to thank the members of my dissertation committee, Profs. Enrique del Barco, Michael Leuenberger, and Pawel Wocjan, for their time and attention in reading my dissertation and providing me with useful insights and comments. I would also like to thank Profs. Talat Rahman, Richard Klemm, Viatcheslav Kokoouline, Leonid Chernyak, and Elena Flitsyian for making my experience here at UCF more complete. It has been a

pleasure interacting with you all, taking classes with some of you or working under your supervision as a teaching assistant. I am also grateful for our conversations that helped guide me in my career choices or just in life in general.

To the administrative staff members here at UCF, Mike, Felix, Monika, Pat, Shreya, and Teresa Dorman, my sincere thanks for your dedication and constant hard work. You were always gracious in helping me. I am particularly indebted to Prof. Harold Baranger and Eduardo Novais for their hospitality during my stay visiting their group at Duke University and the great discussions that made me learn a lot about quantum error correction. I am also grateful to A. Chang, R. Hanson, J. Kycia, J. M. Taylor, for providing us with information related to their experimental setups, as well as W. Coish, and A. Fowler for useful discussions. The work presented in this dissertation was supported in part by the NSF Grant No. CCF-0523603, as well as by the Office of Naval Research. I also acknowledge partial support from the Interdisciplinary Information Science and Technology Laboratory (I^2Lab) at UCF.

TABLE OF CONTENTS

LIST OF FIGURES

LIST OF TABLES

CHAPTER ONE: INTRODUCTION

We begin this chapter by giving a brief historic description of the main developments in quantum computation and quantum information. We subsequently present some of the keys ideas underlying quantum computers, and follow with a discussion of current limitations to the implementation of these devices. We also give motivation to our study of decoherence sources in solid-state qubit systems. Finally, we present an outline of the chapters in this dissertation.

1.1 A brief history of quantum computation and quantum information

In the 1960s, Ralph Landauer was the first to make a connection between information and physical processes [1]. He argued that when information is lost in an irreversible circuit, that information becomes entropy and an associated amount of energy is dissipated as heat. His findings ultimately established a new paradigm, that information was physical in nature, and that computation is a physical process. About a decade later, Charles Bennett showed that all computation could be in principle done in a reversible fashion [2]. Edward Fredkin and Tommaso Toffoli also came to the same result independently around the same time [3, 4].

In 1982, Richard Feynman argued that it would take a quantum system to efficiently simulate other quantum systems [5, 6], and introduced the idea of an *universal quantum simulator* [7]. He also claimed that these quantum machines would be able to perform other tasks more efficiently than their classical counterparts. In 1985, he further considered the possibility of reducing the size of computers until the bits were the size of atoms [8].

In that picture, quantum mechanics and its unique properties would clearly dictate the behavior of such machines. These ideas were later shown to be viable by several authors [9, 10, 11, 12, 13, 14, 15, 16], and the increasing miniaturization of transistors and other semiconductor based electronic devices led to the belief that the technology might be soon approaching a limit where quantum effects become dominant. Also in 1985, David Deutsch developed the very first quantum computational algorithm [17].

A few years later, in the 1990s, Peter Shor developed a quantum algorithm that could efficiently factor large integer numbers [18], showing exponential speed up over any classical factorization algorithms. This sparked renewed interest in the field as it proved to be the first major application of a quantum computer. Around the same time, Lov Grover showed that the problem of conducting a search through an unstructured search space could also be sped up, albeit just quadratically, by use of a quantum algorithm [19]. This increase in computation speed, though not as powerful as in the factorization algorithm, still proved to be significant. At around the same time, Charles Bennett and Gilles Brassard proposed quantum cryptography [20], and Yakir Aharonov and others utilized quantum random walks to design exponentially faster quantum algorithms [21, 22].

1.2 Quantum computers

The basic units of information in a quantum computer are called quantum bits (qubits). While their classical counterparts (bits) can take only one of two possible values, 0 or 1, qubits possess the unique capability of being 0, 1, or any linear superposition of both values. In fact, the superposition of states in a quantum computer, along with entanglement, represent

two of the underlying properties that make quantum computers so unique and so powerful in their capability of processing information in speeds unthinkable to the classical versions of these machines.

A true quantum computer obeys the laws and possesses the properties unique to quantum mechanical systems. As such, their evolution is governed by the Schrödinger equation. A quantum two-level system, utilized to define qubits, can be in a superposition of states $\psi\rangle = \alpha|0\rangle + \beta|1\rangle$, as mentioned before. Because any measurement on this system forces it into one of the possible measurement eigenstates, it is known from quantum mechanics [23] that even though the evolution of the system is deterministic, the measurement outcomes are not. In the state $\psi\rangle$, the probability of measuring $|0\rangle$ is $|\alpha|^2$, while the probability of attaining $|1\rangle$ is $|\beta|^2$. Due to the probabilistic interpretation of α and β, they are constrained to the equation $|\alpha|^2 + |\beta|^2 = 1$ for normalization purposes.

Another important feature distinguishing qubits from classical bits is that multiple qubits can exhibit quantum entanglement. Entanglement is a non-local quantum property that allows a set of qubits to express higher correlation than is possible in classical systems. In a simplistic way, this means that when two quantum two-level systems become entangled, one system cannot be fully described independently of the other. An example of an entangled state is $(|01\rangle + |10\rangle)/\sqrt{2}$. It gives a complete description of the system, and there is an equal probability 1/2 of measuring either state -$|01\rangle$ or $|10\rangle$-. The two subsystems do not possess a definite state, though. Because of the entangled state, if one measures one state, this immediately forces the state of the other subsytem to a definite value, even if they are not close to each other! It has been long speculated whether entanglement really exists, or

whether there exists some kind of hidden variables that due to our lack of knowledge of them make us uncapable of predicting a measurement outcome with certainty. However, it has been shown that entanglement is real by means of measurements of non-local correlations in EPR pairs of photons, whose name was inherited after a *gedanken* experiment proposed by Einstein, Podolsky, and Rosen [24]. This has essentially ruled out any local hidden variable theory and established entanglement as one of the cornerstones of quantum computation.

There are several different technologies that present themselves as candidates for physical implementations of a quantum computer. Technologies as diverse as superconducting devices, trapped ions, cold atoms, nuclear magnetic resonance (NMR), and quantum dots have been intensively studied in recent years, with considerable progress being made in the development of these quantum computing systems. In this dissertation we will restrict our attention to semiconductor quantum dot systems that use the charge degree of freedom of electrons to define the qubits.

1.3 Obstacles and limitations

It is known that quantum systems have a somewhat fragile existence. In order to retrieve any kind of information about a quantum system, it is necessary to be able to make some kind of measurement on the system. One of the consequences of the action of measuring on a quantum system is that it imparts an irreversible change to the quantum state of the system. The superposition states collapse, since the measurements project any initial state to just one of the basis states. This irreversibility is only avoided in the special case where the state is actually one of the eigenstates before measurement. This information though is not available

a priori to whoever is performing the measurement in the system, and the fact that one can only retrieve one result at a time through measurement makes the exponential computing power thus appear inaccessible. The measurement problem has been a long standing issue in quantum mechanics, and still today there seems to be no absolute understanding on what defines a measurement [25].

The fragility in quantum superposition states is not always undesirable, though. In applications of quantum cryptography, it is exactly this fragility that makes these systems reliable. Upon coding of any piece of information, any eavesdropper that tries to read that information will necessarily leave evidence of their interaction with the information, corrupting some of the data.

Any kind of interaction of the pure quantum system - be it with someone performing a measurement or with the uncontrolled environment - will create an irreversible process. This interaction with external degrees of freedom adds extra terms to the system Hamiltonian and what was originally a closed quantum system now becomes open. The additional entanglement of the system with environmental degrees of freedom introduces noise in the computation, as the delicate phase relations between quantum states in a superposition are irreversibly altered and the desired quantum evolution is disturbed. This process is what is known as decoherence, and its direct consequences are errors in the computations. As more errors occur due to flaws in the quantum operations, these errors propagate, significantly altering the computed states from what they should originally be. In principle this presents an unsurmountable challenge to any long computations. However, methods to control the propagation of errors have been shown, relying on efficient detection and correction of these

errors [26, 27]. This comes with a caveat though. These methods only work properly if error rates in computations are small enough that they are below an accuracy threshold [28, 29, 30, 31, 32, 33, 34, 35]. This ensures that errors are properly detected and handled, enabling arbitrarily long computations. The downside is that if these conditions are not met, the correction operations may actually create more errors than they correct. Current threshold estimates range from $10^{-2} - 10^{-6}$, and are strongly dependent on the actual qubit geometry and environment.

For the physical implementation of large scale quantum computations however, the issues mentioned present the biggest obstacles and motivate the work done in this dissertation. The development of quantum algorithms and error correction, combined with the ideas of fault-tolerant quantum computations, makes an actual quantum computer theoretically feasible. On the other hand, it is speculated that for most useful computations, more than a hundred qubits would be required, though a few dozen qubits may already be sufficient for simpler simulations. The challenge to building a large scale quantum computer and coping with the issue of decoherence is still open, though progress has been systematically made by research teams all over the world. Here we will not dwell on methods to detect and correct errors in quantum computations, but we will rather attempt to understand two important physical sources of decoherence in a particular realization of qubit systems, namely quantum dot charge-based qubit systems: interactions between electrons in the quantum dots and (i) phonon modes in the bath and (ii) electromagnetic fluctuations in the circuit leads and electrodes.

1.4 Outline of this dissertation

This dissertation describes a theoretical modeling of decoherence sources for semiconductor charge-based quantum dot setups utilized as candidates for quantum computing systems. We start with the description in Chapter 2 of some of the latest experimental results in measuring relaxation and decoherence times in this class of systems.

In Chapter 3, we calculate the effect of the quantum dots coupling to piezoelectric acoustic phonon modes in the bath, and propose the use of different geometrical quantum dot arrangements to mitigate the nocive effects of the coupling to phonons.

In Chapter 4, we estimate the effect that electromagnetic fluctuations in the circuit gates introduce into the qubit operation. We utilize the Fluctuation-Dissipation Theorem in calculating these effects, and evaluate the quality factor for several different parameter values.

Conclusions of this study are drawn out in Chapter 5, where we also discuss the limitations of the models used. We conclude the dissertation by discussing questions that still remain open regarding decoherence in these systems.

CHAPTER TWO: RECENT EXPERIMENTAL ADVANCES

2.1 Introduction

The realization of a solid-state qubit based on familiar and highly developed semiconductor technology would facilitate scaling to a many-qubit computer and make quantum computation more accessible [36]. Solid-state semiconductor lateral quantum dots are thus strong candidates for the physical realization of qubits. These artificial systems can be designed to allow for the observation of coherent oscillations between their quantum states. Since its first proposals [37, 38], a wide variety of experiments have demonstrated control over the spin degree of freedom of confined electrons in quantum dots [39, 40, 41], as well as charge states [42, 43, 44, 45, 46, 47]. Solid-state quantum computer architectures with qubits encoded in dopant atoms in semiconductor crystals have also been proposed [48, 49].

Quantum dots present the ubiquitous advantages of being manufactured from highly developed semiconductor technology and may offer easier scalability, the latter being key in enabling the manufacturing of large-scale quantum computers in the future. A drawback to their use in quantum computers is that they also couple rather effectively to external degrees of freedom which lead to decoherence.

The earliest proposal of a quantum dot qubit relied on the manipulation of the spin degree of freedom of a single confined electron [37]. An attractive point of that proposal is the large spin decoherence time characteristic of semiconductors; a drawback is that it requires local control of intense magnetic fields. As an alternative, a spin-based logical qubit involving a

multi-quantum dot setup and voltage-controlled exchange interactions was devised [39], but at the price of considerable overhead in additional operations.

While spin qubits remain promising in the long term – note in particular several recent experimental advances [40, 41] as well as further theoretical development of multi-quantum dot spin qubits [50, 51, 52] – charge-based qubits in quantum dots, in analogy to superconducting Cooper-pair box devices, [53, 54, 55, 56] are also worthy of investigation. Employing the charge degree of freedom of electrons rather than their spin brings a few important practical advantages: No local control of magnetic fields is required and all operations can be carried out by manipulating gate voltages. The simplest realization of a charge qubit is a double quantum dot (DQD) system with an odd number of electrons [38, 42, 43, 57, 58, 59, 60, 61, 62], as shown schematically in Fig. 2.1.

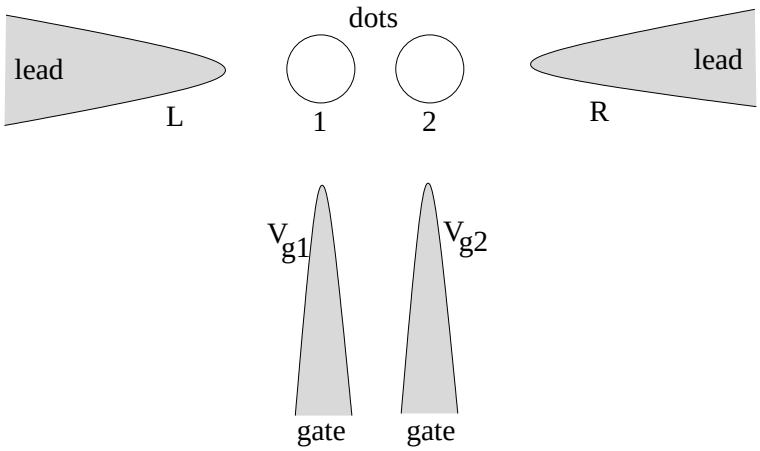

Figure 2.1: Schematic representation of a double quantum dot setup.

One can view this system as a double well potential: The unpaired electron moves between the two wells (i.e., quantum dots) by tunneling through the potential barrier. The logical states $|0\rangle, |1\rangle$ correspond to the electron being on the left or right. The barrier height

determines the tunneling rate between the dots and can be adjusted by a gate voltage. The resulting bonding and antibonding states can also be used as the computational basis. Recently, three groups have implemented the double-dot charge qubit experimentally [44, 45, 46, 47].

Semiconductor qubits are susceptible to various decoherence mechanisms. The effects of hyperfine coupling to lattice nuclear spins can compromise the long phase coherence of electron spins [63, 64]. Charge-based qubits, on the other hand are susceptible to various decoherence mechanisms related to charge motion. A change in the state of the qubit involves electron motion between quantum dots, which can in general couple very effectively to external degrees of freedom such as phonons, charges trapped in the substrate, and electromagnetic environmental fluctuations. These noise sources lead to decoherence times much shorter than those observed in spin qubit systems. Thus, one is tempted to try to find new setups where oscillations between qubit states involve a minimum amount of charge motion. For instance, in qubits based on multiple quantum dots one can pick logical states where charge is homogeneously distributed in space. Another approach is to create a multi-dot structure with symmetries that forbid coupling to certain environmental modes within the logical subspace [65], as will be shown in Chapter 3.

So far measurements of quality (Q) factors of coherent oscillations in these systems have yielded rather low values in the range of 3-10 [44, 45, 46, 47], representing strong damping. In an effort to identify the main sources of decoherence, theoretical estimates of the Q factor have been carried out assuming mainly the coupling to acoustic phonons [57, 58, 59, 60, 61, 62, 65, 66, 67, 68, 69]. However, a discrepancy of at least one order of magnitude remains

between the experimental value and the theoretical estimates, with the latter indicating larger Q factors. This discrepancy leads to the belief that the phonons may not be the dominant noise source. Thus, an investigation of other possible environmetal decoherence mechanisms is in order. In Chapter 4 we consider the coupling of the DQD charge-based qubit systems to voltage fluctuations in the gates.

CHAPTER THREE: PHONON DECOHERENCE IN MULTIPLE-QUANTUM-DOT CHARGE QUBITS

3.1 Introduction

In this chapter we discuss decoherence in charge qubits formed by multiple lateral quantum dots in the framework of the spin-boson model and the Born-Markov approximation. We consider the intrinsic decoherence caused by the coupling to bulk phonon modes. Two distinct quantum dot configurations are studied: (i) Three quantum dots in a ring geometry with one excess electron in total and (ii) arrays of quantum dots where the computational basis states form multipole charge configurations. For the three-dot qubit, we demonstrate the possibility of performing one- and two-qubit operations by solely tuning gate voltages. Compared to a previous proposal involving a linear three-dot spin qubit, the three-dot charge qubit allows for less overhead on two-qubit operations. For small interdot tunnel amplitudes, the three-dot qubits have Q factors much higher than those obtained for double dot systems. The high-multipole dot configurations also show a substantial decrease in decoherence at low operation frequencies when compared to the double-dot qubit.

We also argue that it is not generally possible to avoid decoherence in multi-quantum-dot charge qubits by simple geometrical constructions. The spreading of charge uniformly over a multi-quantum-dot logical qubit does not avoid decoherence. However, the coupling to bosonic environmental modes, such as phonons and photons, can be very substantially attenuated in some circumstances.

In order to demonstrate these assertions, we analyze in detail two prototypical extensions of the double-quantum dot charge qubit. We first consider a qubit consisting of three quantum dots forming a ring-like structure and only one extra electron, as shown in Fig. 3.1. Multi-quantum-dot qubits with a ring-like structure resemble a proposal by Kulik and coauthors [70] to use persistent current states in metallic rings for quantum computation. Unlike the double-dot qubit case, the ground state in a three-dot qubit can be truly degenerate with corresponding wave functions having a uniform charge distribution. At first, this raises the hope that decoherence mechanisms involving charge inhomogeneities (such as phonons or charge traps) would be inhibited due to mutual cancellations. However, we shall see below that the computational basis states can be distinguished by phonon and electromagnetic baths through the electron phase variations along the ring. That, in turn, leads to dephasing and decoherence. This problem is intrinsic to all quantum-dot-based charge qubits. Nevertheless, the Q factor in these three dot qubits can be one to two orders of magnitude larger than in the corresponding double-dot qubits, a substantial improvement in coherence.

Second, we show that planar quantum dot arrays in the form of high-order multipoles can be more efficient in reducing the coupling to acoustic phonons in multi-quantum dot qubits. This dissertation extends and analyzes in detail a recent proposal to create a decoherence-free subspace with charge qubits [66].

While it is well known that condensed-matter environments tend to produce time and spatial correlations in their interaction with qubits [67], here we assume that the Markov approximation provides reasonable estimates of decoherence rates. In particular, we employ

the Redfield equations in the weak-coupling, Born-Markov approximation to describe the time evolution of the reduced density matrix of the qubit system [71].

3.2 The three-dot charge qubit

A simple example of a multi-dot qubit with charge delocalization consists of three quantum dots in a ring-like geometry, as shown in Fig. 3.1. In practice, this system is created by laterally confining electrons in a two-dimensional plane; the confinement is electrostatic, controlled through electrodes sittingabove the plane. Consider gate voltages on the electrodes such that the three dots share one excess, unpaired electron, while all configurations with a different number of excess electrons become energetically inaccessible due to the large charging energy of the dots. The detailed electronic structure of model quantum dots in a triangular configuration has been studied in, for instance, Refs. [72] and [73].

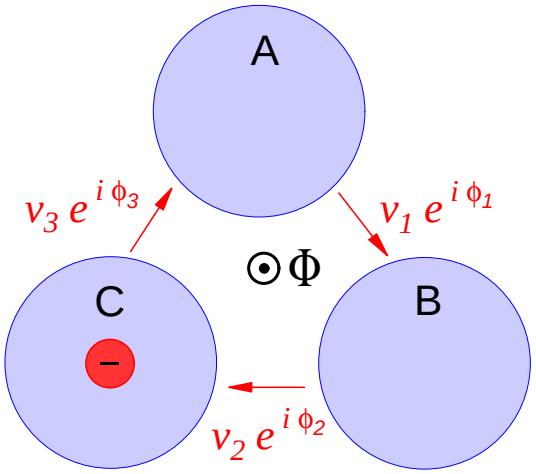

Figure 3.1: Schematic illustration of a three-quantum-dot qubit with only one extra, unpaired electron. The external tuning parameters are the strength of the tunneling couplings (v_1, v_2, and v_3) and the magnetic flux $\Phi = \phi_1 + \phi_2 + \phi_3$ through the qubit. The latter is used solely to define the working point of the qubit.

The spin degree of freedom is not relevant for our discussion and electrons will be assumed spinless unless otherwise specified. Thus, the system lives in a three-dimensional Hilbert space. The electron can hop between dots through tunneling. The tunneling matrix elements and the on-site energies are controlled by the gate voltages. As will be clear shortly, it is convenient to apply a weak magnetic field perpendicular to the plane containing the dots.

The three natural basis states place the electron on dot A, B, or C:

$$|A\rangle = c_A^\dagger\,|\text{vac.}\rangle, \quad |B\rangle = c_B^\dagger\,|\text{vac.}\rangle, \quad |C\rangle = c_C^\dagger\,|\text{vac.}\rangle, \tag{3.1}$$

where $c_\alpha^\dagger$ are creation operators and $|\text{vac.}\rangle$ is a reference state where all dots have an even

number of electrons. In this basis, the Hamiltonian takes the matrix form

$$H = \begin{pmatrix} E_A & -v_1\, e^{i\phi_1} & -v_3\, e^{-i\phi_3} \\ -v_1\, e^{-i\phi_1} & E_B & -v_2\, e^{i\phi_2} \\ -v_3\, e^{i\phi_3} & -v_2\, e^{-i\phi_2} & E_C \end{pmatrix}, \tag{3.2}$$

where E_A, E_B, and E_C are the on-site energies, v_i are the tunneling strengths between pairs of quantum dots, and $\phi_1+\phi_2+\phi_3 = \Phi$ is the total magnetic flux through the ring. Let us specify the qubit by setting $v_1 = v_2 = v_3 \equiv v > 0$, $E_A = E_B = E_C \equiv 0$, and $\phi_1 = \phi_2 = \phi_3 = \Phi/3 \equiv \pi$. In this configuration, two degenerate eigenstates $|+\rangle$ and $|-\rangle$ have the lowest energy, $E_\pm = -v$ (Fig. 3.2). They carry clockwise and counterclockwise persistent currents and form the computational basis. By working with 1 hole per three-dot qubit (*i.e.* 5 electrons in 3 levels) instead of 1 electron, the degeneracy between eigenstates $|+\rangle$ and $|-\rangle$ occurs at $B=0$, which may have some advantages. The third, excited, eigenstate $|T\rangle$ has energy $E_e = 2v$ and is current-free. The eigenvectors are

$$|T\rangle = \frac{1}{\sqrt{3}}\left(|A\rangle + |B\rangle + |C\rangle\right), \tag{3.3}$$

$$|+\rangle = \frac{1}{\sqrt{3}}\left(|A\rangle + e^{i\beta}|B\rangle + e^{-i\beta}|C\rangle\right), \tag{3.4}$$

$$|-\rangle = \frac{1}{\sqrt{3}}\left(|A\rangle + e^{-i\beta}|B\rangle + e^{i\beta}|C\rangle\right), \tag{3.5}$$

with $\beta = 2\pi/3$. Clearly, the charge distribution is spatially uniform for all three states.

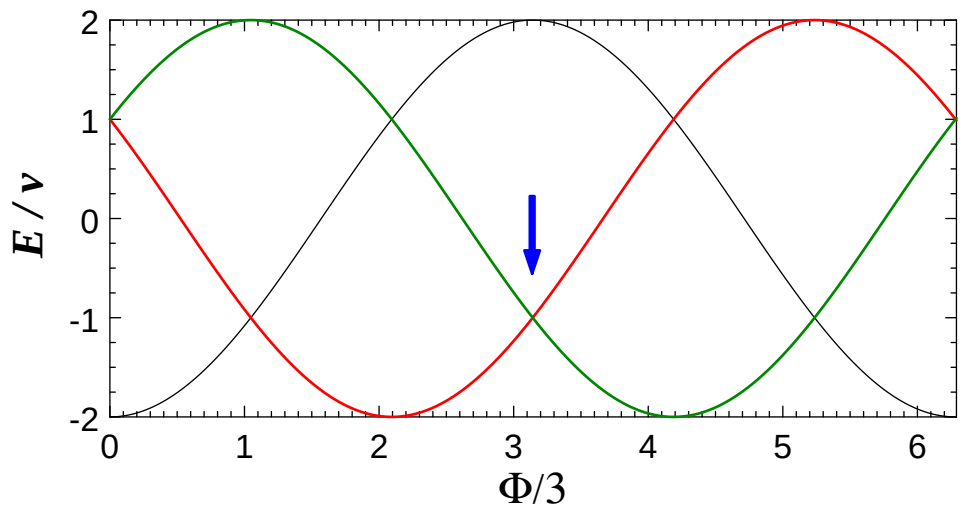

Figure 3.2: Eigenenergies of the three-dot qubit as function of the magnetic flux. The working point at $\Phi/3 = \phi = \pi$ per bond is indicated by the arrow. At this point, clockwise and counterclockwise persistent current states are degenerate, and the charge distribution is homogeneous throughout the space spanned by the computational basis.

It is worth noting that the topology of the three-dot qubit and its use of persistent currents of opposite direction as logical states closely resemble the Josephson persistent current qubit studied in Ref [74]. or the proposed atomic Josephson junction arrays [75]. However, the similarities stop here as the underlying physics is very different. We will focus our discussion on the quantum dot charge qubit case only.

3.2.1 Single-qubit operations

In order to be able to perform quantum gate operations, we have to allow for deviations from the degeneracy point. This is done by varying the tunneling coupling and/or the

magnetic flux. It is convenient to introduce the (small) parameters δ_1, δ_2, δ_3, and φ such that $v_1 = v + \delta_1$, $v_2 = v + \delta_2$, $v_3 = v + \delta_3$, and $\varphi \ll 1$ with $\varphi = \Phi - 3\pi$. To linear order and using a $\{|T\rangle, |+\rangle, |-\rangle\}$ basis, we find that the Hamiltonian expanded around the degeneracy point can be written as

$$H = \begin{pmatrix} 2v + \frac{2}{3}(\delta_1 + \delta_2 + \delta_3) & -\frac{1}{3}\left(\delta_1 e^{-i\beta} + \delta_2 + \delta_3 e^{i\beta}\right) & -\frac{1}{3}\left(\delta_1 e^{i\beta} + \delta_2 + \delta_3 e^{-i\beta}\right) \\ -\frac{1}{3}\left(\delta_1 e^{i\beta} + \delta_2 + \delta_3 e^{-i\beta}\right) & -v - \frac{v\varphi}{\sqrt{3}} - \frac{1}{3}(\delta_1 + \delta_2 + \delta_3) & \frac{2}{3}\left(\delta_1 e^{-i\beta} + \delta_2 + \delta_3 e^{i\beta}\right) \\ -\frac{1}{3}\left(\delta_1 e^{-i\beta} + \delta_2 + \delta_3 e^{i\beta}\right) & \frac{2}{3}\left(\delta_1 e^{i\beta} + \delta_2 + \delta_3 e^{-i\beta}\right) & -v + \frac{v\varphi}{\sqrt{3}} - \frac{1}{3}(\delta_1 + \delta_2 + \delta_3) \end{pmatrix} \tag{3.6}$$

The computational subspace corresponds to the lower-right 2×2 block. Evidently, we stay within the computational subspace as long as $\delta_1 = \delta_2 = \delta_3$. However, this also implies that there is no coupling between the computational basis states $|+\rangle$ and $|-\rangle$. For $\delta_1 e^{i\beta} + \delta_2 + \delta_3 e^{-i\beta} \neq 0$, coupling within the computational subspace is possible, but there is a finite probability of leaking out into the state $|T\rangle$. The leakage can be kept small as long as $v \gg |\delta_{1,2,3}|$. Alternatively, one can incorporate the third level into the single-qubit operations, as in Ref. [70]. For the following case study, we assume that the leakage from the computational subspace is negligible.

Using the Pauli matrices σ_1, σ_2, and σ_3, as well as the identity matrix σ_0, we can express the Hamiltonian in the computational basis in terms of a pseudospin in a pseudomagnetic field $\vec{h}$ plus a constant,

$$H_S = E_0\,\sigma_0 + h_x\,\sigma_1 + h_y\,\sigma_2 + h_z\,\sigma_3, \tag{3.7}$$

where $E_0 = -v - (\delta_1 + \delta_2 + \delta_3)/3$ and

$$h_x = \frac{2}{3}\left(\delta_2 - \frac{\delta_1 + \delta_3}{2}\right), \tag{3.8}$$

$$h_y = \frac{\delta_1 - \delta_3}{\sqrt{3}}, \tag{3.9}$$

$$h_z = -v\varphi/\sqrt{3}. \tag{3.10}$$

We only need to vary two out of the three pseudomagnetic field components in order to perform single-qubit operations. Thus, we can operate the qubit at constant magnetic flux (and set $\varphi = 0$, $h_z = 0$) and vary only the δ_i via gate voltages. If we furthermore fix the coupling $v_2 \equiv v$, $\delta_2 = 0$, we find that the qubit is controlled by the sum and difference of the variation of two intra-qubit couplings, $h_x \propto (\delta_1 + \delta_3)$ and $h_y \propto (\delta_1 - \delta_3)$, that can be adjusted by tuning the respective gate voltages around the symmetry point.

3.2.2 Two-qubit operations

In order to perform two-qubit operations, such as the SWAP or CNOT gate, we have to couple two three-dot qubits (called I and II hereafter). In principle, this can be done in either a tip-to-tip or base-to-base coupling scheme, as shown in Fig. 3.3.

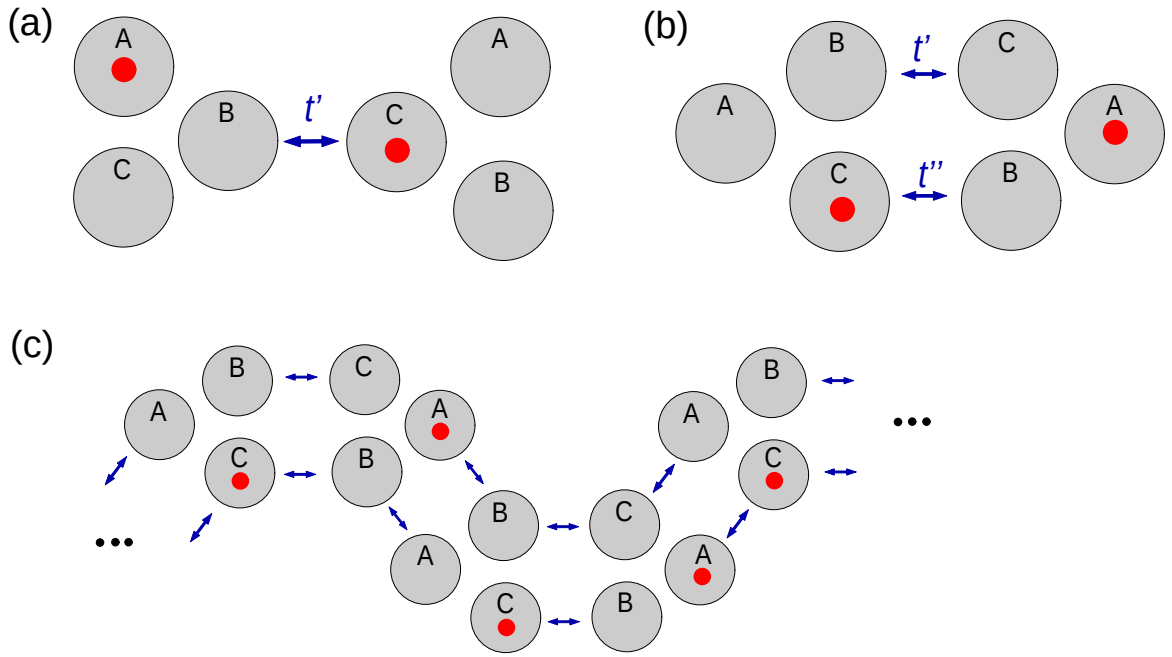

Figure 3.3: Possible implementations of two-qubit gates using three-dot qubits. (a) Coupling via a single dot (tip-tip geometry); (b) coupling via two dots (base-base geometry). (c) A possible implementation of a qubit chain in the base-base configuration.

Since the number of excess electrons in the composite system is equal to two, states where two electrons occupy the same qubit have to be included in the basis of the two-qubit Hilbert space. The basis of the two-qubit Hilbert space reads thus

$$|1\rangle = |+\rangle_{\mathrm{I}}\,|+\rangle_{\mathrm{II}}, \tag{3.11}$$

$$|2\rangle = |+\rangle_{\mathrm{I}}\,|-\rangle_{\mathrm{II}}, \tag{3.12}$$

$$|3\rangle = |-\rangle_{\mathrm{I}}\,|+\rangle_{\mathrm{II}}, \tag{3.13}$$

$$|4\rangle = |-\rangle_{\mathrm{I}}\,|-\rangle_{\mathrm{II}}, \tag{3.14}$$

$$|5\rangle = c^\dagger_{A\mathrm{I}}\, c^\dagger_{B\mathrm{I}}\, |\mathrm{vac.}\rangle, \tag{3.15}$$

$$|6\rangle = c^\dagger_{A\mathrm{I}}\, c^\dagger_{C\mathrm{I}}\, |\mathrm{vac.}\rangle, \tag{3.16}$$

$$|7\rangle = c^\dagger_{B\mathrm{I}}\, c^\dagger_{C\mathrm{I}}\, |\mathrm{vac.}\rangle, \tag{3.17}$$

$$|8\rangle = c^\dagger_{A\mathrm{II}}\, c^\dagger_{B\mathrm{II}}\, |\mathrm{vac.}\rangle, \tag{3.18}$$

$$|9\rangle = c^\dagger_{A\mathrm{II}}\, c^\dagger_{C\mathrm{II}}\, |\mathrm{vac.}\rangle, \tag{3.19}$$

$$|10\rangle = c^\dagger_{B\mathrm{II}}\, c^\dagger_{C\mathrm{II}}\, |\mathrm{vac.}\rangle. \tag{3.20}$$

Here, two types of states have been neglected: First, states with double occupancy of a single dot since the charging energy is assumed to be very large. Second, although the $|T\rangle_{\mathrm{I}}$ and $|T\rangle_{\mathrm{II}}$ states couple to the double-occupied states $|5\rangle$ to $|10\rangle$ through the inter-qubit hopping terms, they are gapped by an energy of order v, which is assumed much larger than the effective two-qubit interaction amplitude t'^2/U_i (see below). Therefore, they were not included in the two-qubit Hilbert subspace. A more technical argument for neglecting the states $|T\rangle_{\mathrm{I}}$ and $|T\rangle_{\mathrm{II}}$ can be constructed as follows. First, keep all such states while performing a first Schrieffer-Wolff transformation to find the effect of virtual excitation to the doubly-occupied states. This yields an effective Hamiltonian in the space of singly-occupied states with magnitude of order t'^2/U_i. It includes off-diagonal terms between the computational basis and the $|T\rangle$ states. Now, perform a second Schrieffer-Wolff transformation relying on the fact that $t'^2/U_i \ll v$ to integrate out the $|T\rangle$ states. The contribution of this second transformation to the effective Hamiltonian in the computational basis is of order $(t'^2/U_i)^2/v$. As this is much smaller than t'^2/U_i, the effect of the $|T\rangle$ states may be safely neglected.

The Hamiltonian for the inter-qubit interaction in the tip-tip setting shown in Fig. 3.3(a)

reads

$$H_{\mathrm{I-II}}^{\mathrm{tip}} = -t'(c_{B\mathrm{I}}^{\dagger}\, c_{C\mathrm{II}} + c_{C\mathrm{II}}^{\dagger}\, c_{B\mathrm{I}}). \tag{3.21}$$

Similarly, the base-base coupling presented in Fig. 3.3(b) is governed by the Hamiltonian (see also Appendix A)

$$H_{\mathrm{I-II}}^{\mathrm{base}} = -t'(c_{B\mathrm{I}}^{\dagger}\, c_{C\mathrm{II}} + c_{C\mathrm{II}}^{\dagger}\, c_{B\mathrm{I}}) - t''(c_{C\mathrm{I}}^{\dagger}\, c_{B\mathrm{II}} + c_{B\mathrm{II}}^{\dagger}\, c_{C\mathrm{I}}), \tag{3.22}$$

where we have chosen the gauge for the vector potential associate to the perperdincular magnetic field to be parallel to the inter-qubit tunneling paths. We assume that the inter-qubit tunneling amplitudes t' and t'' satisfy $0 < t', t'' \ll v \ll U_i$, where U_i is the inter-dot charging or capacitive coupling energy (i.e., the change in the energy of one dot when an electron is added to one of the neighboring dots). In other words, the capacitive coupling between dots must be sufficiently strong so that states with two or zero excess electrons in a qubit are forbidden. Due to the proximity between dots of neighboring qubits, some small inter-qubit capacitive coupling will also exist. Although we will neglect such coupling in the discussion below, these additional charging energies can be included without substantially modifying our results. In particular, we note that the inter-qubit capacitive coupling does not interfere with single-qubit operations. Note also that the presence of a magnetic flux requires the dots A, B, and C to be always arranged in a clockwise order.

Next, the large charging energy separation between the single-occupancy states $|1\rangle$ to $|4\rangle$ and the double-occupancy states $|5\rangle$ to $|10\rangle$ allows us to separate the two-qubit computational subspace from the rest of the Hilbert space. In order to do so, we use a Schrieffer-Wolff transformation [76], which amounts to a second-order perturbative expansion of the effective

Hamiltonian in the ratio of the inter-qubit tunneling magnitude to the charging energy. To this end we insert the expressions for $|+\rangle$ and $|-\rangle$ from Eqs. (3.4)-(3.5) into Eqs. (3.11)-(3.14) and express the computational basis states $|1\rangle$ to $|4\rangle$ in terms of creation operators acting on the vacuum state. Further, using the basis vectors in Eqs. (3.11) to (3.20), one can easily compute the full six-dot Hamiltonian in the basis of states $|1\rangle$ to $|10\rangle$. Noting that one can obtain the tip-tip Hamiltonian from the expression for the base-base case by setting $t'' = 0$, we evaluate the more general case of the base-base coupling, see Fig. 3.3b and Eq. (3.22). The details of the computation, i.e. the full matrix representation of this Hamiltonian, as well as its reduction to the two-qubit computational basis by performing the Schrieffer-Wolff transformation, are shown in Appendix A. The result for the reduced Hamiltonian takes a rather compact form which, for the tip-tip case, reads

$$\tilde{H}^{\text{tip}}_{\text{I}-\text{II}} = -\frac{t'^{\,2}}{9\,U_i} \begin{pmatrix} 4 & e^{-i\beta} & e^{i\beta} & -2 \\ e^{i\beta} & 4 & -2e^{-i\beta} & e^{i\beta} \\ e^{-i\beta} & -2e^{i\beta} & 4 & e^{-i\beta} \\ -2 & e^{-i\beta} & e^{i\beta} & 4 \end{pmatrix}. \tag{3.23}$$

Note that this reduced Hamiltonian acts on the subspace formed by the states $\{|1\rangle, \ldots |4\rangle\}$ defined in Eqs. (3.11) to (3.14). Up to the common prefactor $-t'^{\,2}/(9\,U_i)$, the eigenvalues of

$\tilde{H}^{\rm tip}_{\rm I-II}$ are $E_1 = 0$, $E_2 = 4$, $E_3 = 6$, and $E_4 = 6$, with the respective eigenvectors equal to

$$|E_1\rangle = \frac{1}{2}\Big(|1\rangle - e^{i\beta}|2\rangle - e^{-i\beta}|3\rangle + |4\rangle\Big), \tag{3.24}$$

$$|E_2\rangle = \frac{1}{2}\Big(|1\rangle + e^{i\beta}|2\rangle + e^{-i\beta}|3\rangle + |4\rangle\Big), \tag{3.25}$$

$$|E_3\rangle = \frac{1}{\sqrt{2}}\big(|1\rangle - |4\rangle\big), \tag{3.26}$$

$$|E_4\rangle = \frac{1}{\sqrt{2}}\Big(e^{i\beta}|2\rangle - e^{-i\beta}|3\rangle\Big). \tag{3.27}$$

The critical question now is whether this setup permits a convenient two-qubit operation, such as a full SWAP. It is straightforward to show that the answer is positive, even in the simple tip-tip coupling scheme. To see that, suppose we initialize the qubits in state $|2\rangle$ and now search for the time τ after which the qubits have evolved onto the (swapped) state $|3\rangle$ under the action of $\tilde{H}^{\rm tip}_{\rm I-II}$. The square of the resulting condition, $\Big|\langle 3|e^{-i\tilde{H}^{\rm tip}_{\rm I-II}\tau}|2\rangle\Big|^2 \equiv 1$, is readily evaluated and yields $\tau_S = \pi/2\ [t'^2/(9\,U_i)]^{-1}$ as the (shortest) time for which the tip-tip coupling t' has to be turned on in order to implement the SWAP gate.

For a comparison with the (linear) three-dot spin qubit scheme proposed by DiVincenzo *et al.* [39], let us briefly discuss the implementation of the CNOT quantum gate. A CNOT can be done straightforwardly using two $\sqrt{\rm SWAP}$ operations (SWAP gates of duration $\tau_S/2$) and seven one-qubit gates [37, 77], e.g., by utilizing the scheme in Ref. [77]. Consequently, we find that the realization of one- and two-qubit operations for the present three-dot charge qubit is considerably simpler than for the proposal by DiVincenzo et al. where many more steps were necessary to implement a CNOT. One reason is the complexity of the one-qubit rotations – for the logical spin-qubit, one-qubit operations alone require three spin exchange interaction pulses. For the CNOT gate, this implies at least 19 pulses with 11 different operation times.

Compared to the 9 pulses needed for the three-dot charge qubit, the practical advantages of the qubit and computation scheme proposed here are evident.

3.2.3 Coupling to a bosonic bath

The charge qubit couples to a variety of environmental degrees of freedom. We study in particular the decoherence caused by gapless bosonic modes that sense charge fluctuations in the dots, such as phonons. We assume that all quantum dots couple to the same bath. The Hamiltonian describing the non-interacting bosonic modes in this case is

$$H_B = \sum_{\mathbf{q}} \omega_{\mathbf{q}}\, b^\dagger_{\mathbf{q}} b_{\mathbf{q}}, \tag{3.28}$$

with $\mathbf{q}$ denoting the boson linear momentum and $\omega_{\mathbf{q}}$ its dispersion relation. The coupling between the dots and the bosons is assumed to be governed by the bilinear Hamiltonian

$$H_{\mathrm{dot-boson}} = \sum_{\mathbf{q}} (\alpha_A N_A + \alpha_B N_B + \alpha_C N_C)(b^\dagger_{\mathbf{q}} + b_{-\mathbf{q}}), \tag{3.29}$$

which can be easily derived for the case of phonons, as seen for example in Ref [78]. N_k is the number operator of the kth dot, and

$$\alpha_k = \lambda_{\mathbf{q}}\, P^{(k)}_{\mathbf{q}}\, e^{i\mathbf{R}_k\cdot\mathbf{q}}\,. \tag{3.30}$$

Here, $\lambda_{\mathbf{q}}$ represents the electron-boson coupling constant and $P^{(k)}_{\mathbf{q}}$ and $\mathbf{R}_k$ are form factor and position vector of the kth dot, respectively. Note that all geometrical information is contained in the coefficients α_k. Since we have exactly one excess electron on the three-dot system, the constraint $N_A + N_B + N_C = 1$ must be satisfied. Therefore, the system-bath

Hamiltonian in the basis $\{|A\rangle, |B\rangle, |C\rangle\}$ reads

$$H_{\rm SB} = \sum_{\mathbf{q}} \begin{pmatrix} \alpha_A & 0 & 0 \\ 0 & \alpha_B & 0 \\ 0 & 0 & \alpha_C \end{pmatrix} \left(b_{\mathbf{q}}^\dagger + b_{-\mathbf{q}}\right) . \tag{3.31}$$

Projection of this Hamiltonian onto the subspace spanned by $|+\rangle$ and $|-\rangle$ defined in Eqs. (3.4) and (3.5) constrains the coupling to that subspace, yielding

$$\tilde{H}_{\rm SB} = \frac{1}{3} \sum_{\mathbf{q}} \left[\left(\alpha_A - \frac{\alpha_B + \alpha_C}{2} \right) \sigma_1 - \frac{\sqrt{3}}{2} \left(\alpha_B - \alpha_C \right) \sigma_2 \right] \left(b_{\mathbf{q}}^\dagger + b_{-\mathbf{q}} \right) , \tag{3.32}$$

where a term proportional to σ_0 has been dropped. The presence of two terms with different functional dependence on $\mathbf{q}$ indicates the coupling to two bath modes, which will be denoted by the indices 1 and 2 in the following. There would be a third bath mode, proportional to σ_3, if the charge distribution were not the same for the two logical states. *The advantage of having a homogeneous charge distribution for both states in the computational basis, leading directly to the cancellation of this third mode of decoherence, is evident here.* It is important to remark that charge homogeneity can be achieved without the assumptions of homogeneous tunneling or equal capacitances: as long as one can tune the gate voltages in the quantum dots independently, one can arrange to have one extra electron equally shared among the three dots.

It is convenient to rewrite the system-bath Hamiltonian in the standard spin-boson form [79]

$$\tilde{H}_{\rm SB} \equiv K_1 \Phi_1 + K_2 \Phi_2 , \tag{3.33}$$

where

$$K_1 \equiv \sigma_1/6 \quad \text{and} \quad K_2 \equiv -\sigma_2/2\sqrt{3} \tag{3.34}$$

describe the system part and the corresponding bath part is given by

$$\Phi_{1,2} = \sum_q g_{\mathbf{q}}^{(1,2)} \left(b_{\mathbf{q}}^\dagger + b_{-\mathbf{q}} \right), \tag{3.35}$$

with

$$g_{\mathbf{q}}^{(1)} = 2\alpha_A - \alpha_B - \alpha_C, \tag{3.36}$$

$$g_{\mathbf{q}}^{(2)} = \alpha_B - \alpha_C \, . \tag{3.37}$$

Assuming all $P_{\mathbf{q}}^{(k)}$ to be the same, the following relations among the α_k can be obtained:

$$\alpha_A = \lambda_{\mathbf{q}} P_{\mathbf{q}}, \tag{3.38}$$

$$\alpha_B = \alpha_A e^{i(\mathbf{R}_B - \mathbf{R}_A)\cdot\mathbf{q}} \equiv \alpha_A e^{i\eta_B}, \tag{3.39}$$

$$\alpha_C = \alpha_A e^{i(\mathbf{R}_C - \mathbf{R}_A)\cdot\mathbf{q}} \equiv \alpha_A e^{i\eta_C} \tag{3.40}$$

where the last two equations define the phases η_B and η_C. This completes the specification of the qubit-bath coupling.

3.2.4 The Redfield equation

We now investigate the qubit decoherence due to the bosonic bath by determining the time relaxation of the system's reduced density matrix. We use the Born and Markov approximations and the Redfield equation [71]. In this formalism the reduced density matrix of the system (qubit) is obtained by integrating out the bath degrees of freedom and assuming that:

(i) The Electron-phonon interaction *i.e.*, the coupling to the bath is weak, so leading order perturbation theory is applicable (the Born approximation).

(ii) The relaxation time of the bath is small compared to the evolution of the system. This ultimately means that the bath has very short memory, resulting in a correlation time much shorter than the typical time scale of operation of the qubit, so that system-bath interaction events are uncorrelated in time (the Markov approximation).

When these conditions are satisfied, the bath can be assumed to remain in thermal equilibrium, and the system-bath interaction may be treated perturbatively up to second-order. We can then describe the time evolution of the reduced density matrix is by means of the Redfield equation [71, 80],

$$\begin{aligned} \dot{\rho}(t) &= -i\,[\tilde{H}_S(t), \rho(t)] \\ &\quad + \sum_{\alpha=1,2} \Big\{\, [\Lambda_\alpha(t)\rho(t), K_\alpha] + \big[K_\alpha, \Lambda_\alpha^\dagger(t)\rho(t)\big] \,\Big\}, \end{aligned} \tag{3.41}$$

which is a dissipative form of the Liouville-von-Neumann equation

$$\dot{\rho_{\text{Total}}}(t) = -i\,[\tilde{H}, \rho_{\text{Total}}(t)], \tag{3.42}$$

where ρ_{Total} is the total density matrix, as opposed to ρ in Eq. 3.41. There the time-dependent auxiliary matrices $\Lambda_\alpha(t)$ which encode the bath correlation properties are defined by

$$\Lambda_\alpha(t) = \sum_{\beta=1,2} \int_0^\infty dt' B_{\alpha\beta}(t')\, e^{-it'\tilde{H}_S(t)} K_\beta\, e^{it'\tilde{H}_S(t)}. \tag{3.43}$$

The thermal-average bath correlation functions,

$$B_{\alpha\beta}(t) = \langle \Phi_\beta(t)\, \Phi_\alpha(0) \rangle, \tag{3.44}$$

can be written in terms of spectral functions,

$$\nu_{\alpha\beta}(\omega) = \sum_{\mathbf{q}} g_{\mathbf{q}}^{(\alpha)} g_{\text{-}\mathbf{q}}^{(\beta)} \delta(\omega - \omega_{\mathbf{q}}), \tag{3.45}$$

and the boson occupation number $n_B(\omega) = (e^{\omega/T} - 1)^{-1}$:

$$B_{\alpha\beta}(t) = \int_0^\infty d\omega \, \nu_{\alpha\beta}(\omega) \left\{ e^{i\omega t} n_B(\omega) + e^{-i\omega t} \left[1 + n_B(\omega) \right] \right\} \ . \tag{3.46}$$

Performing the sum over $\mathbf{f}q$ in Eq. (3.45), we find

$$\begin{aligned}
\nu_{11} &= 2 \sum_{\mathbf{q}} |\lambda_{\mathbf{q}} P_{\mathbf{q}}|^2 \, \delta(\omega - \omega_{\mathbf{q}}) \left[3 - 2(\cos\eta_B - \cos\eta_C) + \cos(\eta_B - \eta_C) \right], & (3.47) \\
\nu_{22} &= 2 \sum_{\mathbf{q}} |\lambda_{\mathbf{q}} P_{\mathbf{q}}|^2 \, \delta(\omega - \omega_{\mathbf{q}}) \left[1 - \cos(\eta_B - \eta_C) \right], & (3.48) \\
\nu_{12} &= 2 \sum_{\mathbf{q}} |\lambda_{\mathbf{q}} P_{\mathbf{q}}|^2 \, \delta(\omega - \omega_{\mathbf{q}}) \left[e^{-i\eta_B} - e^{-i\eta_C} + i \sin(\eta_B - \eta_C) \right], & (3.49)
\end{aligned}$$

with $\nu_{21} = \nu_{12}^*$. When the bath is sufficiently large, the sums over the vector $\mathbf{q}$ in Eqs. (3.47)-(3.49) can be converted into three-dimensional integrals.

A few simplifying but realistic assumptions can be made at this point. Let us first assume that the coupling constant $\lambda_{\mathbf{q}}$ and the dispersion relation $\omega_{\mathbf{q}}$ are both isotropic. Second, let us assume that the electronic density in the dots has a Gaussian profile,

$$\rho(\mathbf{r}) = \delta(z) \, e^{-r^2/(2\,a^2)} / (2\pi a^2), \tag{3.50}$$

resulting in

$$P_{\mathbf{q}} = \int d^3r \, \rho(r) \, e^{-i\mathbf{q}\cdot\mathbf{r}} = e^{-(aq\sin\theta)^2/2}, \tag{3.51}$$

where (q, θ, φ) are the spherical coordinates of the boson wave vector. Then, the three-fold symmetry in the plane causes $\nu_{12}(\omega)$ to vanish and

$$\nu_{11}(\omega) = 3\,\nu(\omega) \ , \quad \nu_{22}(\omega) = \nu(\omega), \tag{3.52}$$

with

$$\nu(\omega) = \frac{\Omega\, q^2}{2\pi^2}|\lambda_q|^2 \left|\frac{d\omega_q}{dq}\right|^{-1} \int_0^{\pi/2} d\theta\, \sin\theta\, e^{-(qa\sin\theta)^2} \left[1 - J_0\left(qD\sin\theta\right)\right], \tag{3.53}$$

where $\omega = \omega_q$, Ω is the crystal unit cell volume, and D is the distance between dots.

For III-V semiconductor materials at low temperatures, the most relevant bosonic modes are piezoelectric acoustic phonons [81], for which we have $\lambda_q = \pi s\sqrt{g_{\rm ph}/q\Omega}$ and $\omega_q = sq$. Here, $g_{\rm ph}$ is the dimensionless electron-phonon coupling constant and s is the phonon velocity (for GaAs, $g_{\rm ph} \approx 0.05$ and $s \approx 5 \times 10^3$ m/s) [60].

3.2.5 Decoherence rates

We now solve the equation-of-motion for the reduced density matrix explicitly for a case in which the decoherence rate can be obtained directly. Consider a constant pulse applied to the qubit at $t = 0$ such that $h_y = h_z = 0$ and $h_x = \Delta > 0$. For $t > 0$, the Λ_α matrices are constant and given by

$$\Lambda_1 = \gamma_0\, \sigma_1/2\,, \tag{3.54}$$

$$\Lambda_2 = -(1/2\sqrt{3})\, (\gamma_c\, \sigma_2 + \gamma_s\, \sigma_3)\,. \tag{3.55}$$

The (complex) relaxation rates are given by

$$\gamma_0 \equiv \int_0^\infty dt\, B_{22}(t), \tag{3.56}$$

$$\gamma_c \equiv \int_0^\infty dt\, B_{22}(t)\, \cos(2\Delta t), \tag{3.57}$$

$$\gamma_s \equiv \int_0^\infty dt\, B_{22}(t)\, \sin(2\Delta t). \tag{3.58}$$

The relaxation part of Eq. (3.41) then reads

$$\sum_{\alpha=1,2}\left\{[\Lambda_\alpha\,\rho,K_\alpha]+\text{h.c.}\right\} = \frac{\gamma_0'}{6}\begin{pmatrix}\rho_{22}-\rho_{11} & \rho_{12}^*-\rho_{12}\\ \rho_{12}-\rho_{12}^* & \rho_{11}-\rho_{22}\end{pmatrix}+\frac{\gamma_c'}{6}\begin{pmatrix}\rho_{22}-\rho_{11} & -\rho_{12}^*-\rho_{12}\\ -\rho_{12}-\rho_{12}^* & \rho_{11}-\rho_{22}\end{pmatrix} + i\frac{\gamma_s'}{6}\begin{pmatrix}\rho_{12}-\rho_{12}^* & 0\\ 0 & \rho_{12}^*-\rho_{12}\end{pmatrix}+\frac{\gamma_s''}{6}\begin{pmatrix}0 & 1\\ 1 & 0\end{pmatrix}, \tag{3.59}$$

where the single and double primes denote real and imaginary parts, respectively. They can be easily evaluated, yielding

$$\gamma_0' = 0, \tag{3.60}$$

$$\gamma_c' = \gamma_s'' = \frac{\pi}{2}\,\nu(2\Delta)\coth\left(\frac{\Delta}{T}\right), \tag{3.61}$$

$$\gamma_s' = -\fint_0^\infty \frac{dy}{y^2-1}\,\nu(2\Delta y)\coth\left(\frac{\Delta y}{T}\right), \tag{3.62}$$

where the $\fint$ in the expression for γ_s' denotes the Cauchy principal value of the improper integral. A change of variable is needed to deal with the infinity at the upper limit of the integral. The integral may then be solved numerically by means of the trapezoidal method and a modified Simpson's method, and both results are interpolated to yield the final estimate to γ_s'. The Liouville term in Eq. (3.41) is obtained straightforwardly:

$$-i\,[\tilde{H}_S,\rho] = -i\Delta\,[\sigma_1,\rho] = -i\Delta\begin{pmatrix}\rho_{12}^*-\rho_{12} & \rho_{22}-\rho_{11}\\ \rho_{11}-\rho_{22} & \rho_{12}-\rho_{12}^*\end{pmatrix}. \tag{3.63}$$

Introducing Eqs. (3.59) and (3.63) into (3.41), we obtain

$$\dot{\rho}_{11} = -2\left(\Delta+\frac{\gamma_s'}{6}\right)\rho_{12}''+\frac{\gamma_c'}{6}\,(1-2\rho_{11}), \tag{3.64}$$

$$\dot{\rho}_{12}' = -\frac{\gamma_c'}{3}\,\rho_{12}'+\frac{\gamma_c'}{6}, \tag{3.65}$$

$$\dot{\rho}_{12}'' = -\Delta\,(1-2\rho_{11}), \tag{3.66}$$

where we have split the off-diagonal term ρ_{12} into real and imaginary parts, $\rho'_{12} + i\rho''_{12}$.

In order to identify energy and phase relaxation rates, we rewrite the elements of the reduced matrix in the eigenbasis of the system Hamiltonian,

$$|E = \pm\Delta\rangle = \frac{1}{\sqrt{2}}\left(|+\rangle \pm |-\rangle\right), \tag{3.67}$$

resulting in

$$\dot{\tilde{\rho}}_{11} = -\frac{\gamma'_c}{3}\tilde{\rho}_{11} + \frac{\gamma'_c}{3}, \tag{3.68}$$

$$\dot{\tilde{\rho}}'_{12} = -\left(2\Delta + \frac{\gamma'_s}{3}\right)\tilde{\rho}''_{12} - \frac{\gamma'_c}{3}\tilde{\rho}'_{12}, \tag{3.69}$$

$$\dot{\tilde{\rho}}''_{12} = 2b\,\tilde{\rho}'_{12}. \tag{3.70}$$

The solution of the diagonal term is straightforward,

$$\tilde{\rho}'_{11}(t) = 1 + [\tilde{\rho}'_{11}(0) - 1]\; e^{-\gamma'_c t/3}, \tag{3.71}$$

which allows us to read directly the energy relaxation time,

$$T_1 = \frac{3}{\gamma'_c}. \tag{3.72}$$

For the off-diagonal term, one finds that the real part is given by

$$\tilde{\rho}'_{12}(t) = \tilde{\rho}'_{12}(0)\, e^{-t/T_2}\, \cos(\omega_c t), \tag{3.73}$$

where the phase relaxation time is equal to

$$T_2 = \frac{6}{\gamma'_c} \tag{3.74}$$

and the frequency of quantum oscillations is given by

$$\omega_c = \sqrt{2\Delta\left(2\Delta + \frac{\gamma'_s}{3}\right) - \frac{{\gamma'_c}^2}{36}}. \tag{3.75}$$

Note that $T_2 = 2T_1$, as well-known for the super-ohmic spin-boson model in the weak-coupling regime [82, 83].

Except for a factor of three in the relaxation rates, Eqs. (3.72)-(3.75) are identical to those found in Ref. [60] for a double-dot charge qubit. However, one has to recall that while in the double-dot qubit Δ is the interdot hopping matrix element v, for the three-dot qubit it takes a much smaller value, of the order of $\delta_{1,2,3}$. The decoherence times will be longer for the three-dot qubit, but so will be the quantum oscillation period and the single-qubit gate pulses. Therefore, it is meaningful to compare the quality factor of the the three-dot qubit to that obtained for the double-dot qubit for a *fixed magnitude* of v, which is a common experimental parameter to both setups. The comparison for the case of piezoelectric acoustic phonons and realistic GaAs quantum dot geometries (data for the double-dot qubit was obtained from Ref. [60]) is shown in Fig. 3.4. The Q factor is defined as

$$Q = \frac{\omega_c T_2}{2\pi}. \tag{3.76}$$

We assume $\omega_c \approx 2\Delta$ since $\Delta \gg \gamma_c', \gamma_s'$ in the weak-coupling regime.

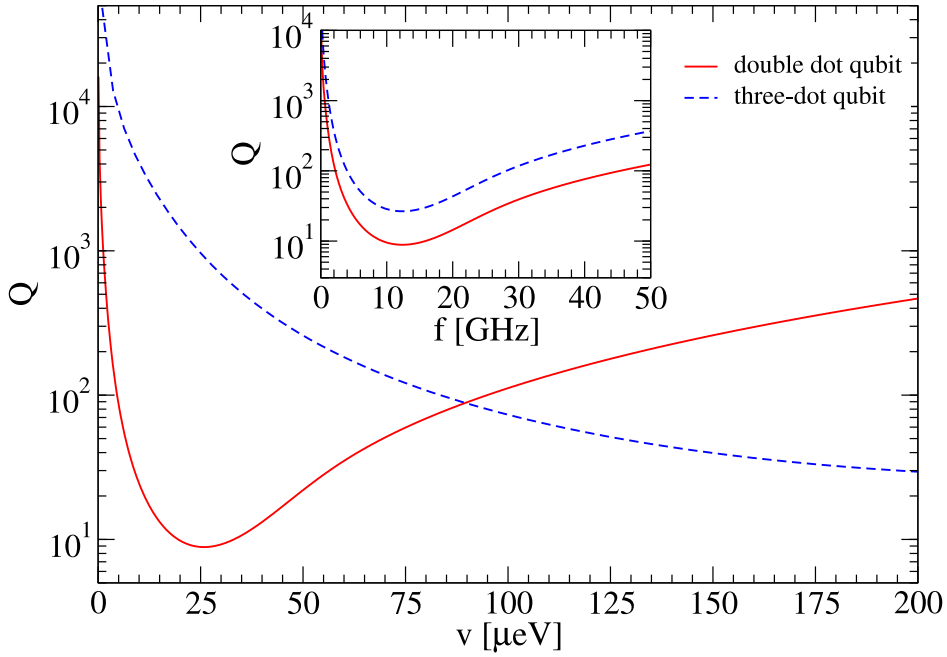

Figure 3.4: Comparison between the Q factors of a three-dot and a double-dot charge qubit coupled to piezoelectric acoustic phonons. The parameters used are: $a = 60$ nm, $D = 180$ nm, $s = 5 \times 10^3$ m/s, $T = 15$ mK, and $g_{\rm ph} = 0.05$, which correspond to realistic lateral quantum dot systems in GaAs. Here the variable v denotes the interdot tunnel amplitude. Note that for double dot qubits, $\Delta = v$, while for three-dot qubits we assumed $\Delta = 0.1\, v$. The inset shows the same Q factors when the oscillation frequency (rather than v) is fixed. In this case the curves only differ by a factor of 3.

The improvement in the Q factor is substantial for small tunnel amplitudes. A similar result was previously found by Storcz *et al.* in Ref. [68] when considering the phonon-induced

decoherence in a system of two double-dot charge qubits with a small tunnel splitting ("slow tunneling"). There, the dominant quadrupolar contribution to the *two-qubit* decoherence yields a ω_c^5 dependence for the Q factor. In our case, the extra protection in the three-dot qubit compared to the slow tunneling double-dot system arises mainly because the oscillation frequency ω_c (i.e., the amplitude of the transverse pseudomagnetic field) is smaller in the three-dot qubit by the ratio Δ/v [see Eq. (3.2)]. This ratio must be kept small in order to avoid leakage from the computational basis. In Fig. 3.4 it was set to 0.1. However, for a fixed oscillation frequency (see inset in Fig. 3.4), the Q factors for these two qubits differ by only an overall factor of three.

To summarize up to this point, our study indicates that using a computational basis with a homogeneous charge distribution improves the quality of the qubit but does not rid it from decoherence completely. The reason lies in the fact that bosonic modes propagating in the xy plane can pick up distinct phase shifts when interacting with different dots [see Eqs. (3.38) to (3.40)]. However, there is no complete destructive interference along any direction of propagation in the plane, as can be seen from Eqs. (3.36) and (3.37). In fact, one can show that the same is true for any ringlike array of dots that share a single excess electron.

3.3 Charge qubits in multipole configurations

As recently proposed by Oi *et al.* [66], there is another way in which the geometry of the quantum dot qubit array and its charge distribution can be chosen to minimize the coupling to environmental degrees of freedom. Here we demonstrate how their idea can be extended to multiple-dot charge qubits coupled to gapless bosonic modes. It turns out that by reducing

the computational space to particular multipole charge configurations one can substantially reduce the coupling to bath modes at low frequencies. We consider qubits and basis states as shown in Fig. 3.5. The qubit consists of a planar array of dots with alternating excess charge. Note that the operation of such a qubit is straightforward: The excess charge is only allowed to hop between every other pair of neighboring dots, namely, between dots numbered $2n-1$ and $2n$, with $n = 1, \ldots, 2^{p-1}$, where p is the multipole order, $l = 2^p$ (see Fig. 3.5). Tunnel barriers between alternating pairs of dots must be maintained small and fixed (to avoid leakage), while the remaining barriers have to be modulated in time to implement an X gate. The Z gate is implemented by inducing a small bias between even- and odd-numbered dots. Two-qubit operations can be implemented in analogy to the procedure discussed in Ref. [10]

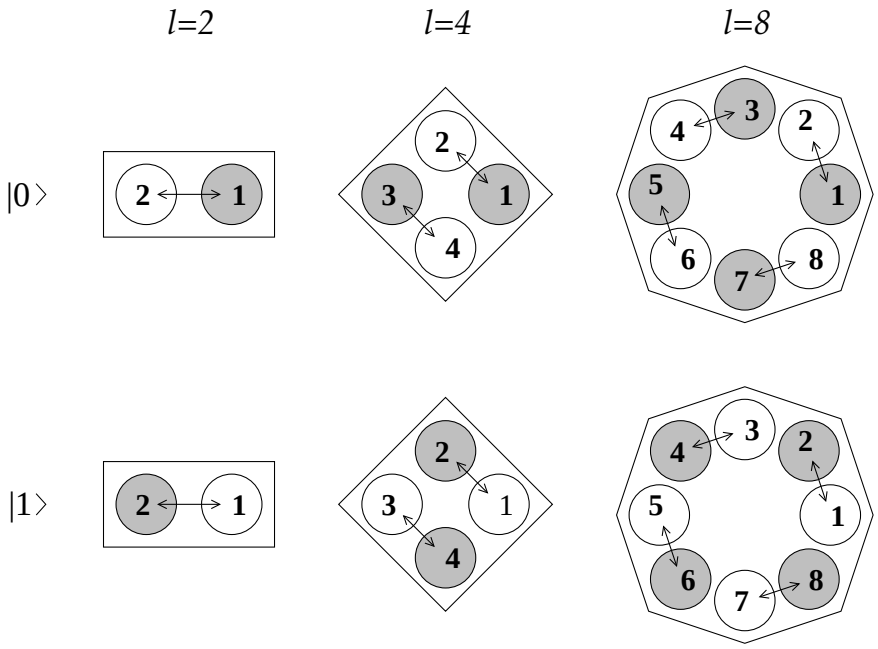

Figure 3.5: The three lowest multipole charge qubit configurations (dipole, quadrupole, and octopole). The two computational basis states, $|0\rangle$ and $|1\rangle$, are indicated for for each configuration. Empty (filled) circles correspond to empty (occupied) quantum dots. The arrows indicate the pairs of quantum dots where excess charge can hop.

The basis states for each multipole configuration have complementary charge distributions that tend to cancel out the coupling to phonon modes propagating along certain directions in the xy plane. The number of such directions increases with the multipole order, resulting in an attenuation of the overall coupling to phonons at low frequencies (large wavelengths). The crossover frequency where this attenuation occurs is $\omega_{\rm cross}^{(l)} \sim s/d_l$, where d_l is the radius of the dot array. At high frequencies, however, when the phonon wavelength is much smaller than the radius d_l, decoherence becomes stronger because phonons can resolve the internal structure of the qubit and disturb charge motion between individual pairs of dots.

In order to demonstrate these effects, let us derive an expression for the spectral function of the qubit-bath system. For simplicity, we assume that all dots in the qubit are identical. In this case, the bath modes couple to charge variations in the dots according to the Hamiltonian

$$H_{\rm SB} = \sum_{\mathbf{q}} \sum_{k=1}^{l} \alpha_k \, N_k \, (b_{\mathbf{q}}^{\dagger} + b_{\text{-}\mathbf{q}}), \tag{3.77}$$

where $l = 2^p$ and N_k is the excess charge in the kth dot. For the case of acoustic phonons, the coefficients α_k were defined in Eq. (3.30). Projecting this Hamiltonian onto the computational basis (as shown in Fig. 3.5), we find that, up to a constant term,

$$H_{\rm SB} = K \, \Phi_l, \tag{3.78}$$

where $K = -\sigma_z/2$ acts on the qubit space and

$$\Phi_l = \sum_{\mathbf{q}} g_{\mathbf{q}}^{(l)} (b_{\mathbf{q}}^{\dagger} + b_{\text{-}\mathbf{q}}), \tag{3.79}$$

acts on the phonon bath, with

$$g_{\mathbf{q}}^{(l)} = \sum_{k=1}^{l} (-1)^k \alpha_k = \lambda_{\mathbf{q}} \, P_{\mathbf{q}} \sum_{k=1}^{l} (-1)^k e^{i \mathbf{R}_k \cdot \mathbf{q}}. \tag{3.80}$$

It is convenient to choose the position vectors of the dots as $\mathbf{R}_k = d_l(\hat{x} \cos\varphi_k + \hat{y} \sin\varphi_k)$, where $\varphi_k = (2\pi/l)(k-1)$ and d_l is the array radius: $d_l = D/2\sin(\pi/l)$, where D is the distance between neighboring dots. This yields

$$\left| g_{\mathbf{q}}^{(l)} \right|^2 = |\lambda_{\mathbf{q}} \, P_{\mathbf{q}}|^2 \sum_{k,j=1}^{l} (-1)^{k+j} \exp\Big[2i d_l q \sin\theta \sin\Big(\varphi - \frac{\varphi_k + \varphi_j}{2}\Big) \sin\Big(\frac{\varphi_k - \varphi_j}{2}\Big)\Big], \tag{3.81}$$

where (q, θ, φ) are the spherical coordinates of the wave vector $\mathbf{f}q$. It is not difficult to see that $g_{\mathbf{f}q} = 0$ for $\theta = \pi/2$ and $\varphi = (2m-1)\pi/l$, with $m = 1, \ldots, l$.

The spectral function can now be obtained in analogy to the calculation shown in Sec. 3.2.4. For a thermal bath of acoustic piezoelectric phonons, we find

$$\begin{aligned}\nu_l(\omega) &= \sum_{\mathbf{q}} \left|g_{\mathbf{q}}^{(l)}\right|^2 \delta(\omega-\omega_{\mathbf{f}q}) \\ &= \frac{g_{\rm ph}\,\omega\,l}{2}\int_0^{\pi/2} d\theta\,\sin\theta\,\exp\!\left(-\frac{a^2\omega^2\sin^2\theta}{s^2}\right)\Bigg\{1+(-1)^{l/2}J_0\left(\frac{2d_l\omega}{s}\sin\theta\right) \\ &\quad +2\sum_{m=1}^{l/2-1}(-1)^m J_0\left[\frac{2d_l\omega}{s}\sin\theta\sin\left(\frac{m\pi}{l}\right)\right]\Bigg\}. \end{aligned} \tag{3.82}$$

Implicit in Eq. (3.82) are the assumptions of in-plane isotropy of $\lambda_{\mathbf{q}}$, $P_{\mathbf{q}}$, and $\omega_{\mathbf{q}}$. Note that for $l=2$ one recovers the spectral function for a double dot qubit obtained in Ref. [60]. The low-frequency behavior of the spectral density becomes apparent when we expand the Bessel functions in a power series, resulting in

$$\nu_l(\omega) = \frac{g_{\rm ph}\,\omega\,l}{2}\int_0^{\pi/2} d\theta\,\sin\theta\,\exp\left(-\frac{\omega^2a^2}{s^2}\sin^2\theta\right)\sum_{k=1}^{\infty}\frac{(-1)^k}{(k!)^2}\left(\frac{d_l\omega}{s}\sin\theta\right)^{2k} a_k^{(l)}, \tag{3.83}$$

where

$$a_k^{(l)} = (-1)^{l/2} + 2\sum_{m=1}^{l/2-1}(-1)^m \sin^{2k}\left(\frac{m\pi}{l}\right). \tag{3.84}$$

It is possible to show that $a_k^{(l)}=0$ for $k<l/2$ when l is an integer power of 2. Therefore, $\nu_l(\omega\to 0)\sim\omega^{l+1}$. For large l, this amounts to the appearance of a pseudo gap in the spectral function at low frequencies. The asymptotic behavior of the spectral function at high frequencies is also straightforward to obtain: One finds $\nu_l(\omega\to\infty)\sim l/\omega$. Thus, the tail of the spectral function raises with increasing multipole order.

The structure of the computational basis is simple enough to allow for the qubit to couple to just one bath mode (in contrast to the three-dot qubit, where two modes couple to the

qubit). Thus, the standard expressions for the relaxation times in the spin-boson model can be used [83]. The result is

$$\gamma^{(l)} = \frac{\pi}{2}\nu_l(2v)\coth\left(\frac{v}{T}\right), \tag{3.85}$$

where v is the inter-dot tunnel amplitude. Note that Eq. (3.85) reduces to the result found in Ref. [60] when $l = 2$, as expected. Provided that v is sufficiently smaller than the temperature, $\gamma^{(l)} \sim v^l$. Thus, by increasing the order of the multipole and maintaining a low frequency of operation, one can decrease the qubit relaxation rate by orders of magnitude without affecting the frequency of quantum oscillations. In Fig. 3.6 we show the Q factor of several multipole charge qubits as a function of the inter-dot coupling v. Note that at low frequencies high quantum oscillations are much less damped for high multipole configurations. This translates into single-qubit gates of much higher fidelity. Clearly, this gain in the Q factor has to be contrasted with the high complexity of operating a logical qubit comprised by a large number of quantum dots, as well with the slowness in operation. As the gating becomes slower, other sources of decoherence may become more relevant.

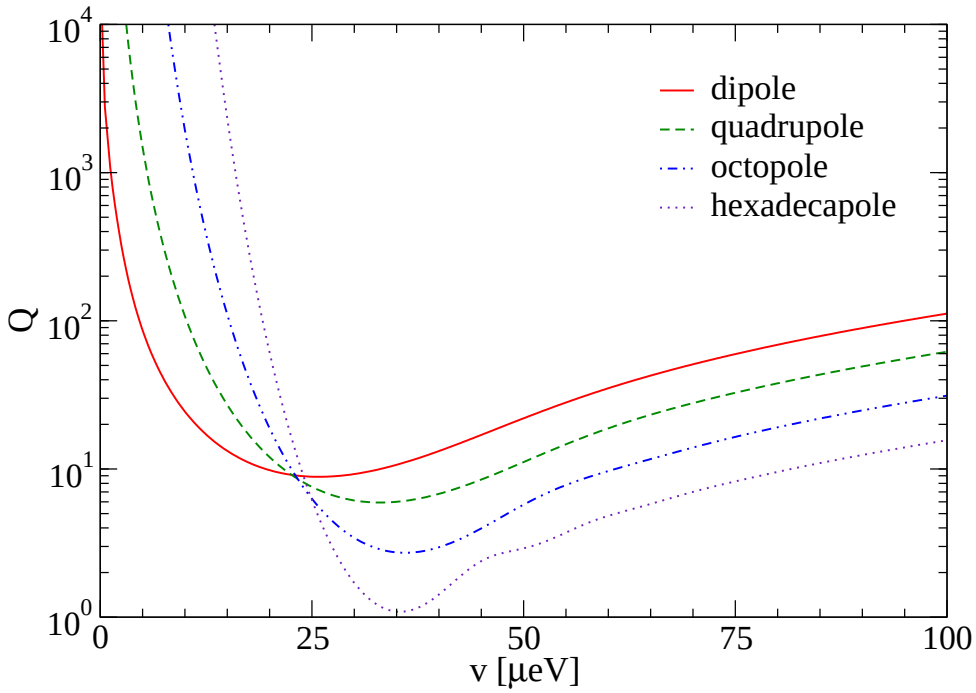

Figure 3.6: Q factors for multipole charge qubits ($l = 2, 4, 8, 16$) coupled to piezoelectric acoustic phonons: $Q_l = \omega_c/\pi\gamma^{(l)}$, where $\omega_c \approx 2v$ [for $\gamma^{(l)}$, see Eq. (3.85)]. Physical and geometrical parameters are the same as those used in Fig. 3.4. In particular, note that the inter-dot distance is fixed, $D = 120$ nm, for all configurations.

It is also important to remark that, in practice, the pseudogap width, $\omega_{\rm cross}^{(l)}$, will shrink with increasing multipole order. This is because the dot array radius scales as $d_l \approx l\,D/2\pi$ for $l \gg 1$. Therefore, for a fixed value of D, one has $\omega_{\rm cross}^{(l)} \sim 2\pi\, s/(l\,D)$ for $l \gg 1$. Finally, we note that the results discussed above are valid for any gapless bosonic bath. Different dependences on q for the coupling constant λ_q and dispersion relation ω_q will only change the power of the frequency-dependent prefactor in Eq. (3.83).

In the following chapter we will analyze the influence of electromagnetic fluctuations in generating decoherence in a double-quantum-dot charge-based qubit.

CHAPTER FOUR: DECOHERENCE BY ELECTROMAGNETIC FLUCTUATIONS IN DOUBLE-QUANTUM-DOT CHARGE QUBITS

4.1 Introduction

In this chapter we discuss decoherence due to electromagnetic fluctuations in charge qubits formed by two lateral quantum dots. We use effective circuit models and the spin-boson model to evaluate correlations of voltage fluctuations in the qubit setup. These correlations allows us to estimate energy (T_1) and phase (T_2) relaxation times of the the qubit system.

4.2 Hamiltonian of the double quantum dot system

The Hamiltonian of a DQD can be separated into a quantum part related to the occupation of energy levels on each dot and a classical part that quantifies the charging energy:

$$H = \sum_n \varepsilon_{1n}\, c_{1n}^\dagger c_{1n} + \sum_n \varepsilon_{2n}\, c_{2n}^\dagger c_{2n} + E(N_1, N_2), \tag{4.1}$$

where $c_{in}^\dagger, c_{in}$ are creation and annihilation operators of the state with energy ε_{in} in the left ($i = 1$) or right dot ($i = 2$). The dot occupation numbers are defined as $N_i = \sum_n c_{in}^\dagger c_{in}$ while the total charging energy is given by [84]

$$\begin{aligned} E(N_1, N_2) \;=\; & \frac{E_{C1}}{2}N_1^2 + \frac{E_{C2}}{2}N_2^2 + N_1 N_2 E_{Cm} - \frac{1}{|e|}[C_{g1}V_{g1}(N_1 E_{C1} + N_2 E_{Cm})] \\ & -\frac{1}{|e|}[C_{g2}V_{g2}(N_1 E_{Cm} + N_2 E_{C2})] + \frac{1}{2e^2}[C_{g1}^2 V_{g1}^2 E_{C1} + C_{g2}^2 V_{g2}^2 E_{C2}] \\ & +\frac{1}{e^2}[C_{g1}V_{g1}C_{g2}V_{g2}E_{Cm}], \end{aligned} \tag{4.2}$$

with the individual charging energies defined as

$$E_{C1} = \frac{e^2}{C_1}\left(1-\frac{C_m^2}{C_1C_2}\right)^{-1}, \tag{4.3}$$

$$E_{C2} = \frac{e^2}{C_2}\left(1-\frac{C_m^2}{C_1C_2}\right)^{-1}, \tag{4.4}$$

$$E_{Cm} = \frac{e^2}{C_m}\left(\frac{C_1C_2}{C_m^2}-1\right)^{-1}. \tag{4.5}$$

The capacitances and voltages shown in Eqs. (4.2) to (4.5) are defined in Fig. 4.1. $C_{1,2}$ is the sum of all capacitances attached to dot 1 or 2: $C_{1,2} = C_{T1,2} + C_{g1,2} + C_m$.

For the purpose of our analysis, the Hamiltonian can be greatly simplified. Notice that the DQD qubit can be viewed as a double-well potential where an unpaired electron oscillates between both quantum dots by tunneling through the potential barrier. Spin degrees of freedom can be neglected. By adjusting the gate voltages, one can set the system near the degeneracy point $E(1,0) = E(0,1)$, in which case the logical states of the qubit correspond to the electron being on the left or right, $|L\rangle$ ($N_1 = 1$ and $N_2 = 0$) and $|R\rangle$ ($N_1 = 0$ and $N_2 = 1$), respectively. The typical single-particle level spacing within each quantum dot is assumed sufficiently large so that only one level on each dot needs to be considered at low enough temperatures. The barrier height Δ determines the tunneling rate between the dots and can be adjusted by a gate voltage while a bias ε between the two dots can also be applied through two independent plunger gate voltages. The dynamics in the DQD qubit is then governed by the reduced two-level Hamiltonian

$$H_S = \frac{\varepsilon}{2}\left(|L\rangle\langle L| - |R\rangle\langle R|\right) + \frac{\Delta}{2}\left(|L\rangle\langle R| + |R\rangle\langle L|\right), \tag{4.6}$$

with the constraint that $|L\rangle\langle L| + |R\rangle\langle R| = 1$. On the other hand, if we define

$$|L\rangle = \begin{pmatrix} 1 \\ \\ 0 \end{pmatrix} \quad |R\rangle = \begin{pmatrix} 0 \\ \\ 1 \end{pmatrix}, \tag{4.7}$$

$$\tag{4.8}$$

it is easy to see that

$$|L\rangle\langle L| - |R\rangle\langle R| = \sigma_z = \begin{pmatrix} 1 & 0 \\ \\ 0 & -1 \end{pmatrix}. \tag{4.9}$$

Electromagnetic noise is introduced into the DQD qubit system by means of gate voltage fluctuations. These fluctuations may originate from the voltage sources and the thermal noise in the transmission lines, and introduce decoherence into the qubit system through interactions with the electrons in the quantum dots. While the former can be substantially reduced by careful filtering, the latter is less controlled. Here we will focus on the noise coming from the plunger gates. In general, the effect of voltage fluctuations in the gate electrodes is to introduce an additional term in the qubit Hamiltonian,

$$H_{SB} = e\left(\delta V_{g1} - \delta V_{g2}\right)\left(|L\rangle\langle L| - |R\rangle\langle R|\right). \tag{4.10}$$

Depending on the particular qubit setup, other sources of electromagnetic noise may also exist, such as bias and current voltage fluctuations. They can affect not only the qubit coherent dynamics but also the state measurement. For the sake of maintaining some generality in our study, we will only treat electromagnetic fluctuations which can be expressed as Eq. (4.10). In addition, we will model the voltage fluctuations through frequency-dependent impedances along the gate transmission lines.

4.3 Hamiltonian for the electromagnetic environment

The effective circuit of a double quantum dot setup is shown in Fig. 4.1. The effect of the electromagnetic environment is modeled by the frequency-dependent impedances $Z_{1,2}(\omega)$. In the experimental setups, the voltage lines typically run parallel to each other over several microns or more. In order to take into account any capacitive coupling between the lines, we introduced capacitance C_{12} into the circuit.

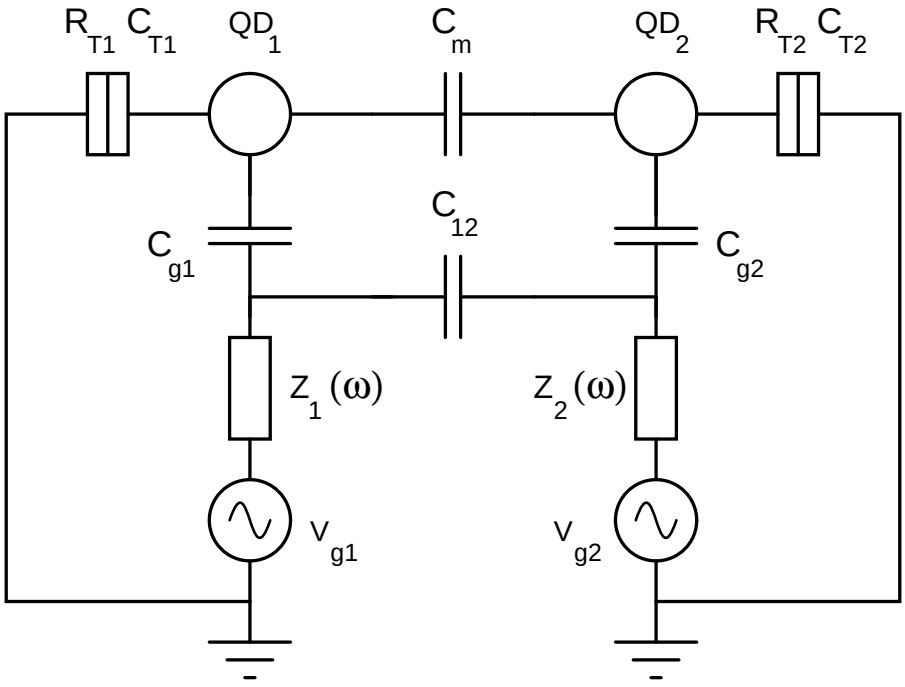

Figure 4.1: Circuit representation of a double quantum dot system coupled to an electromagnetic environment through metallic gate electrodes.

The impedances $Z_{1,2}(\omega)$ can be modeled by means of a transmission line with distributed elements, which stems from the fact that the source of noise in our circuit is spatially distributed along a finite length. Let us consider first each transmission line independently, as

shown in Fig. 4.2, whose impedance $Z_i(\omega)$ can be represented by an infinite ladder network of identical inductors L_{ti} and capacitors C_{ti} [87]:

$$Z_i(\omega) = \frac{1}{2}\left(i\omega L_{ti} + \sqrt{-\omega^2 L_{ti}^2 + 4\frac{L_{ti}}{C_{ti}}}\right). \tag{4.11}$$

A detailed solution to the infinite ladder network is presented in Appendix B. Typically it would be necessary to estimate the values of the spatially distributed resistance, capacitance and inductance in the circuit, but the choice to model the impedance as a LC transmission line can be made because it is known that through a (not necessarily trivial) normal mode transformation, any RLC or RC transmission line can be written as an infinite LC ladder network. The elements C_{ti} and L_{ti} of the transmission line can be determined from two real parameters of the real: the cutoff frequency ω_c and the low frequency asymptotic limit to the characteristic impedance $Z(\omega = 0)$. The high cutoff frequency is the frequency for which $\mathrm{Re}\{Z(\omega)\} = 0$ when $\omega \geq \omega_c$,

$$\omega_c = \frac{2}{\sqrt{L_{ti}C_{ti}}}. \tag{4.12}$$

$Z_i(\omega = 0)$, on the other hand, can be calculated by taking the low frequency asymptotic limit of Eq. (4.11). It is straightforward to see that this limit yields

$$Z_i(\omega = 0) = \sqrt{\frac{L_{ti}}{C_{ti}}} = R, \tag{4.13}$$

where R is an ohmic resistance.

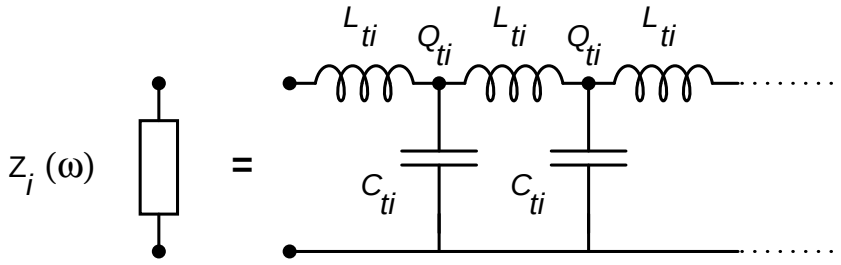

Figure 4.2: Circuit representation of the electromagnetic environment as a transmission line.

We now wish to represent the transmission line in terms of its normal modes. In quantized form, the charge at the lth node, $Q_{l,i}$, and the flux $\phi_{l,i}$ are conjugated variables obeying the commutation relation $[\phi_{l,i}, Q_{l',i'}] = ie\delta_{i,i'}\delta_{l,l'}$. Following the standard procedure, we define the Hamiltonian governing the flux and charge fluctuations along such transmission as

$$H_{T,i} = \frac{Q_{0,i}^2}{2C_{gi}} + \sum_{l=1}^{+\infty}\left[\frac{Q_{l,i}^2}{2C_{ti}} + \frac{\hbar^2}{e^2}\frac{(\phi_{l,i}-\phi_{l-1,i})^2}{2L_{ti}}\right]. \tag{4.14}$$

Notice that C_{gi} represent the capacitive coupling between the quantum dots and their respective gates, while C_{ti} and L_{ti} represent the capacitive and inductive term, respectively, at each rung in the transmission line. The diagonalization of the semi-infinite transmission line when $C_{gi} \neq C_{ti}$ is nontrivial since this asymmetry breaks translation invariance. The solution is presented in Appendix C.

Adding the capacitive coupling between the voltage transmission lines, we obtain the following environmental noise Hamiltonian:

$$H_B = H_{T,1} + H_{T,2} + \frac{Q_{0,1}Q_{0,2}}{C_{12}}. \tag{4.15}$$

The cross term complicates the task of finding the normal models of the environment.

4.4 Single dot-junction case

This problem was treated in detail by Ingold and Nazarov [86], and we reproduce it here for the sake of clarity and completeness, as the double junction solution will be based on their original solution. The main difference here from Ref. [86] is that we include the gate capacitance in the description of the junction (see Fig. 4.3). Notice that

$$V = i\,Z + V_g \qquad \text{and} \qquad V_g = \frac{Q}{\tilde{C}}, \tag{4.16}$$

with the effective junction capacitance $\tilde{C}^{-1} = C^{-1} + C_g^{-1}$ (since the capacitors are in series, the charge in the junction is the same as in the gate). Since $i = \dot{Q}$, we arrive at

$$V = Z\,\dot{Q} + \frac{Q}{\tilde{C}}. \tag{4.17}$$

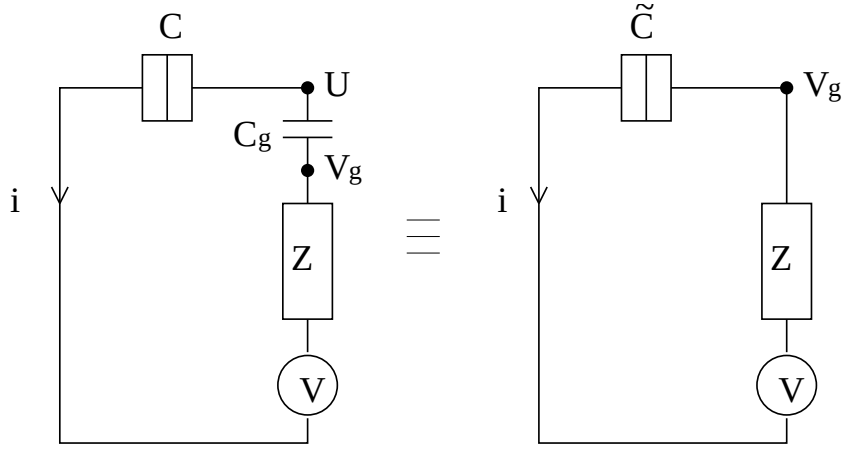

Figure 4.3: Circuit of a single-dot junction coupled to a voltage source through a noisy line.

The environment Hamiltonian can be written as

$$H_{\rm env} = H_{\rm charge} + \sum_{n=1}^{\infty}\left[\frac{1}{2C_n}q_n^2 + \left(\frac{\hbar}{e}\right)^2\frac{1}{2L_n}\left(\tilde{\varphi}_g - \varphi_n\right)^2\right], \tag{4.18}$$

where $\tilde{\varphi}_g(t) = \varphi_g(t) - \frac{e}{\hbar} V\, t$. This variable is conjugated to the charge fluctuation: $\left[\varphi_g, \tilde{Q}\right] = ie$, where $\tilde{Q} = Q - \tilde{C}\, V$. The first term in Eq. (4.18) describes the charging energy in the circuit. Let us derive the equation of motion for the charge fluctuation $\tilde{Q}(t)$ in detail since we will use it later for the coupled dot case. We begin with Hamilton's equations:

$$\frac{\partial H_{\rm env}}{\partial q_n} = \frac{\hbar}{e}\dot{\varphi}_n \qquad \rightarrow \qquad q_n = \frac{\hbar C_n}{e}\,\dot{\varphi}_n \tag{4.19}$$

$$\frac{\partial H_{\rm env}}{\partial \varphi_n} = -\frac{\hbar}{e}\dot{q}_n \qquad \rightarrow \qquad \frac{\hbar}{eL_n}\,(\tilde{\varphi}_g - \varphi_n) = \dot{q}_n. \tag{4.20}$$

From these equations it follows that

$$\ddot{\varphi}_n + \omega_n^2\,\varphi_n = \omega_n^2\,\tilde{\varphi}_g, \tag{4.21}$$

with $\omega_n = 1/\sqrt{L_n C_n}$. We will solve this equation by utilizing the Laplace transform method. The Laplace transform of a function can be defined as

$$\hat{F}(s) = \mathcal{L}\{f(t)\} = \int_0^\infty e^{-st} f(t) dt, \tag{4.22}$$

where the complex parameter $s = \sigma + i\omega$ and both σ and ω are real numbers. In order to solve Eq. (4.21), we will need the general expression for the Laplace transform of the nth derivative of a function

$$\mathcal{L}\{f^{(n)}(t)\} = s^n \hat{F}(s) - s^{(n-1)} f(0) - \ldots - f^{(n-1)}(0). \tag{4.23}$$

Using this expression in Eq. (4.21) yields

$$s^2\hat{\varphi}_n(s) - s\,\varphi_n(0) - \dot{\varphi}_n(0) + \omega_n^2\hat{\varphi}_n(s) = \omega_n^2\,\hat{\tilde{\varphi}}_g(s). \tag{4.24}$$

Solving for $\hat{\varphi}_n(s)$ and inverse Laplace transforming, we get

$$\varphi_n(t) = F_n(t) + \omega_n \int_0^t dt'\, \sin\left[\omega_n(t-t')\right]\, \tilde{\varphi}_g(t'), \tag{4.25}$$

where the inhomogeneous part contains the initial conditions,

$$F_n(t) = \frac{1}{\omega_n}\sin(\omega_n t)\,\dot{\varphi}_n(0) + \cos(\omega_n t)\,\varphi_n(0). \tag{4.26}$$

Using Eq. (4.19), we then obtain

$$q_n(t) = \frac{\hbar C_n}{e}\dot{F}_n(t) + \frac{\hbar}{eL_n}\int_0^t dt'\,\cos\left[\omega_n(t-t')\right]\,\tilde{\varphi}_g(t') \tag{4.27}$$

and

$$\dot{q}_n(t) = G_n(t) + \frac{\hbar}{eL_n}\int_0^t dt'\,\cos\left[\omega_n(t-t')\right]\,\dot{\tilde{\varphi}}_g(t'), \tag{4.28}$$

where

$$G_n(t) = \frac{\hbar C_n}{e}\ddot{F}_n(t). \tag{4.29}$$

Now, using the following Hamilton's equation,

$$\frac{\partial H_{\text{env}}}{\partial \tilde{\varphi}_g} = -\frac{\hbar}{e}\dot{\tilde{Q}} \qquad \rightarrow \qquad \left(\frac{\hbar}{e}\right)\sum_{n=1}^{\infty}\frac{(\varphi_n - \tilde{\varphi}_g)}{L_n} = -\dot{\tilde{Q}} \tag{4.30}$$

and combining it with Eq. (4.20), we obtain

$$\dot{\tilde{Q}} = -\sum_{n=1}^{\infty}\dot{q}_n. \tag{4.31}$$

Therefore,

$$\dot{\tilde{Q}}(t) + \frac{1}{\tilde{C}}\int_0^t dt'\,y(t-t')\,\tilde{Q}(t') = I_N(t), \tag{4.32}$$

where the parameters $\{C_n, L_n\}$ must be chosen such that

$$y(t) = \sum_{n=1}^{\infty}\frac{1}{L_n}\cos(\omega_n t) \tag{4.33}$$

and

$$I_N(t) = -\sum_{n=1}^{\infty} \frac{\hbar C_n}{e} \ddot{F}_n(t). \tag{4.34}$$

The Fourier transform of $y(t)$, as defined by

$$Y(\omega) = \mathcal{F}\{y(t)\} = \int_{-\infty}^{\infty} e^{-i\omega t} y(t) dt, \tag{4.35}$$

is

$$Y(\omega) = \frac{1}{Z(\omega)}, \tag{4.36}$$

which is the admittance of the transmission line as seen in Fig. 4.2. Notice that in Eq. (4.32) we have used that

$$\frac{\partial H_{\text{env}}}{\partial \tilde{Q}} = \frac{\hbar}{e} \dot{\tilde{\varphi}}_g \qquad \rightarrow \qquad \dot{\tilde{\varphi}}_g = \frac{e}{\hbar} \frac{\tilde{Q}}{\tilde{C}}, \tag{4.37}$$

since

$$H_{\text{charge}} = \frac{\tilde{Q}^2}{2\tilde{C}}. \tag{4.38}$$

In fact, one can also arrive at Eq. (4.37) through these steps:

$$\dot{\tilde{\varphi}}_g = \frac{e}{\hbar} (V_g - V) \tag{4.39}$$

and

$$V_g = \frac{Q}{\tilde{C}} = \frac{\tilde{Q}}{\tilde{C}} + V. \tag{4.40}$$

Substituting Eq. (4.40) into (4.39), we arrive at

$$\dot{\tilde{\varphi}}_g = \frac{e}{\hbar} \frac{\tilde{Q}}{\tilde{C}}. \tag{4.41}$$

4.4.1 Fluctuation-dissipation theorem and voltage fluctuations

Starting from Eq. (4.32) and using Eq. (4.41), we can also obtain an equation-of-motion for the phase fluctuations:

$$\tilde{C}\,\ddot{\tilde{\varphi}}_g(t) + \int_0^t dt'\, Y(t-t')\,\dot{\tilde{\varphi}}_g(t') = \frac{e}{\hbar} I_N(t). \tag{4.42}$$

Following Ingold and Nazarov [86], let us Fourier transform this expression. Also, instead of the random internal noise to the transmission line represented by the inhomogeneous term $I_N(t)$, let us include an external driving current $I_{\rm pert}(t)$ in order to evaluate the system's linear response. We then get

$$\begin{aligned} \frac{e}{\hbar}\, I_{\rm pert}(\omega) &= \left[-\omega^2\,\tilde{C} + \frac{i\omega}{Z(\omega)}\right] \tilde{\varphi}(\omega) \\ &= \frac{i\omega}{Z_t(\omega)}\,\tilde{\varphi}_g(\omega), \end{aligned} \tag{4.43}$$

where

$$\frac{1}{Z_t(\omega)} = \frac{1}{Z(\omega)} + i\omega\,\tilde{C}. \tag{4.44}$$

The generalized force associated to the phase fluctuation $\tilde{\varphi}_g(t)$ has dimensions of angular momentum. Let us write its Fourier transform as $F_g(\omega) = (\hbar/e)\, I_{\rm pert}(\omega)$. Therefore, we arrive at the linear response relation

$$\tilde{\varphi}_g(\omega) = \chi_{\varphi_g}(\omega)\, F_g(\omega), \tag{4.45}$$

where the dynamical susceptibility is given by

$$\chi_{\varphi_g}(\omega) = \chi_{\varphi_g}(\omega)' + i\chi''_{\varphi_g}(\omega) \tag{4.46}$$

$$= \left(\frac{e}{\hbar}\right)^2 \frac{Z_t(\omega)}{i\omega}, \tag{4.47}$$

with its imaginary part given by

$$\chi''_{\varphi_g}(\omega) = -\left(\frac{e}{\hbar}\right)^2 \frac{\mathrm{Re}\left\{Z_t(\omega)\right\}}{\omega}. \tag{4.48}$$

We can now invoke the fluctuation-dissipation theorem [88], which says that

$$\left\langle |\tilde{\varphi}_g(\omega)|^2 \right\rangle = \int_{-\infty}^{\infty} dt\, e^{-i\omega t} \left\langle \tilde{\varphi}_g(t)\, \tilde{\varphi}_g(0) \right\rangle = \frac{-2\hbar\, \chi''_{\varphi_g}(\omega)}{1 - e^{-\beta\hbar\omega}}. \tag{4.49}$$

Therefore,

$$\left\langle |\tilde{\varphi}_g(\omega)|^2 \right\rangle = \left(\frac{e}{\hbar}\right)^2 \frac{2\hbar}{\omega} \frac{\mathrm{Re}\left\{Z_t(\omega)\right\}}{1 - e^{-\beta\hbar\omega}}. \tag{4.50}$$

The fluctuations in the phase are related to the fluctuations in the voltage at the dot location, δU: Since $\dot{\varphi}_g = (e/\hbar)\, V_g$ and $V_g = (C/\tilde{C})\, U$, we can write

$$i\omega\, \tilde{\varphi}_g(\omega) = \frac{e}{\hbar} \frac{C}{\tilde{C}}\, \delta U(\omega). \tag{4.51}$$

As a result, we obtain the power spectrum of the voltage fluctuations at the dot location,

$$\left\langle |\delta U(\omega)|^2 \right\rangle = \frac{2\hbar\omega}{1 - e^{-\beta\hbar\omega}} \left(\frac{\tilde{C}}{C}\right)^2 \mathrm{Re}\left\{Z_t(\omega)\right\}, \tag{4.52}$$

which resembles the usual Johnson-Nyquist noise formula.

4.5 Double dot-junction case

We start with the setup shown in Fig. 4.4. Then, following a straightforward application of Kirchhoff's laws, we find the relations

$$V_1 = (i_1 + i_{12} + i_m)\, Z_1 + V_{g1}, \tag{4.53}$$

$$V_2 = (i_1 - i_{12} - i_m)\, Z_2 + V_{g2}, \tag{4.54}$$

with

$$V_{g1} - V_{g2} = i_{12}\, Z_{12} \tag{4.55}$$

and

$$U_1 - U_2 = i_m\, Z_m, \tag{4.56}$$

where $Z_{12} = (i\omega C_{12})^{-1}$ and $Z_m = (i\omega C_m)^{-1}$.

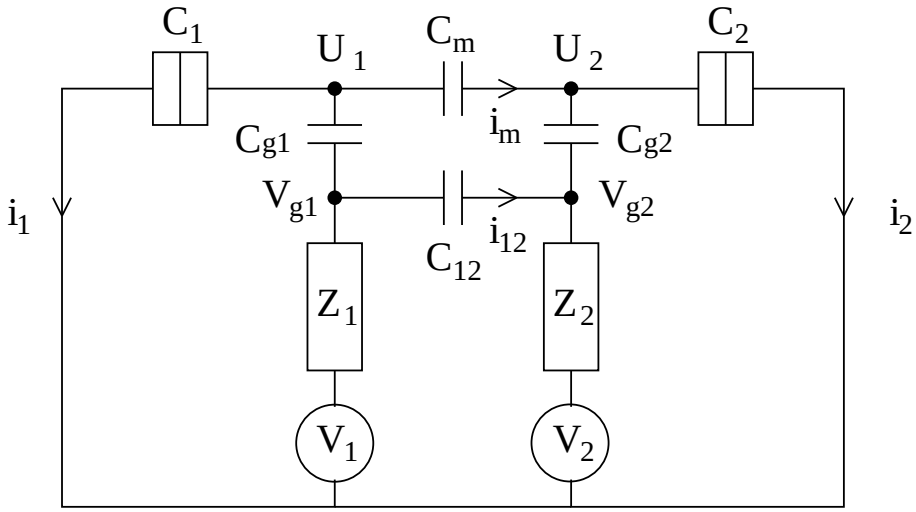

Figure 4.4: Circuit of a double-dot junction system coupled to two voltage sources through noisy lines.

We begin by eliminating i_{12} and i_m in Eqs. (4.53) and (4.54) with the help of Eqs. (4.55) and (4.56):

$$V_1 = i_1\, Z_1 + U_1 \frac{Z_1}{Z_m} - U_2 \frac{Z_1}{Z_m} + V_{g1}\left(1 + \frac{Z_1}{Z_{12}}\right) - V_{g2}\frac{Z_1}{Z_{12}}, \tag{4.57}$$

$$V_2 = i_2\, Z_2 + U_2 \frac{Z_2}{Z_m} - U_1 \frac{Z_2}{Z_m} + V_{g2}\left(1 + \frac{Z_2}{Z_{12}}\right) - V_{g1}\frac{Z_2}{Z_{12}}. \tag{4.58}$$

The next step is to write V_{g1} and V_{g2} in terms of U_1 and U_2. For this purpose, we notice that

$$V_{g1} = U_1 + (i_1 + i_m)\, Z_{g1}, \tag{4.59}$$

$$V_{g2} = U_2 + (i_2 - i_m)\, Z_{g2}. \tag{4.60}$$

Therefore, eliminating i_m, we get

$$V_{g1} = U_1 \left(1 + \frac{Z_{g1}}{Z_m}\right) - U_2 \frac{Z_{g1}}{Z_m} + i_1\, Z_{g1}, \tag{4.61}$$

$$V_{g2} = U_2 \left(1 + \frac{Z_{g2}}{Z_m}\right) - U_1 \frac{Z_{g2}}{Z_m} + i_2\, Z_{g2}. \tag{4.62}$$

In order to eliminate i_1 and i_2, we relate them to the charge in the junction capacitors:

$$C_1\, U_1 = Q_1, \qquad i_1 = \dot{Q}_1, \tag{4.63}$$

$$C_2\, U_2 = Q_2, \qquad i_2 = \dot{Q}_2. \tag{4.64}$$

Rewriting V_{g1} and V_{g2}, and afterwards V_1 and V_2 results in

$$V_{g1} = U_1 \left(1 + \frac{C_m}{C_{g1}}\right) - U_2 \frac{C_m}{C_{g1}} + \frac{Q_1}{C_{g1}}, \tag{4.65}$$

$$V_{g2} = U_2 \left(1 + \frac{C_m}{C_{g2}}\right) - U_1 \frac{C_m}{C_{g2}} + \frac{Q_2}{C_{g2}} \tag{4.66}$$

and

$$V_1 = V_{g1} + (V_{g1} - V_{g2}) \frac{Z_1}{Z_{12}} + U_1 \frac{Z_1}{Z_m} - U_2 \frac{Z_1}{Z_m} + i_1 Z_1, \tag{4.67}$$

$$V_2 = V_{g2} + (V_{g2} - V_{g1}) \frac{Z_2}{Z_{12}} + U_2 \frac{Z_2}{Z_m} - U_1 \frac{Z_2}{Z_m} + i_2 Z_2. \tag{4.68}$$

Eliminating V_{g1}, V_{g2} and rewriting V_1, V_2 in terms of i_1, i_2, Q_1 and Q_2, we obtain

$$
\begin{aligned}
V_1 &= \left(Z_1\left[1+\frac{C_m}{C_1}\right]+Z_1C_{12}\left[\frac{1}{C_1}\left(1+\frac{C_m}{C_{g1}}\right)+\frac{1}{C_{g1}}+\frac{C_m}{C_{g2}C_1}\right]\right)i_1 \\
&+ \left(-Z1\frac{C_m}{C_2}-Z_1C_{12}\left[\frac{C_m}{C_{g1}C_2}+\left(1+\frac{C_m}{C_{g2}}\right)\frac{1}{C_2}+\frac{1}{C_{g2}}\right]\right)i_2 \\
&+ \left(\left[1+\frac{C_m}{C_{g1}}\right]\frac{1}{C_1}+\frac{1}{C_{g1}}\right)Q_1 \\
&+ \left(\frac{-C_m}{C_{g1}C_2}\right)Q_2 \qquad (4.69)
\end{aligned}
$$

and

$$
\begin{aligned}
V_2 &= \left(-Z_2\frac{C_m}{C_1}-Z_2C_{12}\left[\frac{C_m}{C_{g2}C_1}+\left(1+\frac{C_m}{C_{g1}}\right)\frac{1}{C_1}+\frac{1}{C_{g1}}\right]\right)i_1 \\
&+ \left(Z_2\left[1+\frac{C_m}{C_2}\right]+Z_2C_{12}\left[\frac{1}{C_2}\left(1+\frac{C_m}{C_{g2}}\right)+\frac{1}{C_{g2}}+\frac{C_m}{C_{g1}C_2}\right]\right)i_2 \\
&+ \left(\frac{-C_m}{C_{g2}C_1}\right)Q_1 \\
&+ \left(\left[1+\frac{C_m}{C_{g2}}\right]\frac{1}{C_2}+\frac{1}{C_{g2}}\right)Q_2 \qquad (4.70)
\end{aligned}
$$

Finally, using Eqs. (4.63) and (4.64) and rewriting the result in matrix notation, we arrive at

$$
\begin{pmatrix} V_1 \\ V_2 \end{pmatrix} = \mathcal{Z}\cdot\begin{pmatrix} \dot{Q}_1 \\ \dot{Q}_2 \end{pmatrix} + \tilde{C}^{-1}\cdot\begin{pmatrix} Q_1 \\ Q_2 \end{pmatrix}, \qquad (4.71)
$$

where

$$
\mathcal{Z} = \begin{pmatrix} \mathcal{Z}_{11} & \mathcal{Z}_{12} \\ \mathcal{Z}_{21} & \mathcal{Z}_{22} \end{pmatrix}, \qquad (4.72)
$$

with

$$\mathcal{Z}_{11} = Z_1\left[1+\frac{C_m}{C_1}\right]+Z_1C_{12}\left[\frac{1}{C_1}\left(1+\frac{C_m}{C_{g1}}\right)+\frac{1}{C_{g1}}+\frac{C_m}{C_{g2}C_1}\right], \quad (4.73)$$

$$\mathcal{Z}_{12} = -Z1\frac{C_m}{C_2}-Z_1C_{12}\left[\frac{C_m}{C_{g1}C_2}+\left(1+\frac{C_m}{C_{g2}}\right)\frac{1}{C_2}+\frac{1}{C_{g2}}\right], \quad (4.74)$$

$$\mathcal{Z}_{21} = -Z_2\frac{C_m}{C_1}-Z_2C_{12}\left[\frac{C_m}{C_{g2}C_1}+\left(1+\frac{C_m}{C_{g1}}\right)\frac{1}{C_1}+\frac{1}{C_{g1}}\right], \quad (4.75)$$

$$\mathcal{Z}_{22} = Z_2\left[1+\frac{C_m}{C_2}\right]+Z_2C_{12}\left[\frac{1}{C_2}\left(1+\frac{C_m}{C_{g2}}\right)+\frac{1}{C_{g2}}+\frac{C_m}{C_{g1}C_2}\right]. \quad (4.76)$$

$\tilde{C}$, on the other hand, can be defined as

$$\tilde{C} = \frac{1}{\det(\tilde{C}^{-1})}\begin{pmatrix} \left[1+\frac{C_m}{C_{g2}}\right]\frac{1}{C_2}+\frac{1}{C_{g2}} & \frac{C_m}{C_{g1}C_2} \\ \frac{C_m}{C_{g2}C_1} & \left[1+\frac{C_m}{C_{g1}}\right]\frac{1}{C_1}+\frac{1}{C_{g1}} \end{pmatrix}, \quad (4.77)$$

where

$$\det(\tilde{C}^{-1}) = \left(\left[1+\frac{C_m}{C_{g1}}\right]\frac{1}{C_1}+\frac{1}{C_{g1}}\right)\left(\left[1+\frac{C_m}{C_{g2}}\right]\frac{1}{C_2}+\frac{1}{C_{g2}}\right)-\frac{C_m^2}{C_{g1}C_{g2}C_1C_2}. \quad (4.78)$$

Notice that when we decouple the two halves of the circuit by setting $C_m = 0$ and $C_{12} = 0$ in Eq. (4.71), we obtain two equations similar to Eq. (4.17) for each half of the circuit.

In analogy to the single dot-junction circuit, the Hamiltonian for the environment in this case can be written as

$$H_{\rm env} = H_{\rm charge}+\sum_{n=1}^{\infty}\left[\frac{q_{n1}^2}{2C_{n1}}+\left(\frac{\hbar}{e}\right)^2\frac{\left(\tilde{\varphi}_{g1}-\varphi_{n1}\right)^2}{2L_{n1}}+\frac{q_{n2}^2}{2C_{n2}}+\left(\frac{\hbar}{e}\right)^2\frac{\left(\tilde{\varphi}_{g2}-\varphi_{n2}\right)^2}{2L_{n2}}\right]. \quad (4.79)$$

Following exactly the same steps used in deriving Eq. (4.28), we find that

$$\dot{q}_{n1}(t) = G_{n1}(t)+\frac{\hbar}{eL_{n1}}\int_0^t dt'\,\cos\left[\omega_{n1}(t-t')\right]\,\dot{\tilde{\varphi}}_{g1}(t'), \quad (4.80)$$

$$\dot{q}_{n2}(t) = G_{n2}(t)+\frac{\hbar}{eL_{n2}}\int_0^t dt'\,\cos\left[\omega_{n2}(t-t')\right]\,\dot{\tilde{\varphi}}_{g2}(t'), \quad (4.81)$$

where $\omega_{n1} = 1/\sqrt{L_{n1}C_{n1}}$, $\omega_{n2} = 1/\sqrt{L_{n2}C_{n2}}$, and

$$G_{n1}(t) = -\frac{\hbar}{eL_{n1}}\left[\frac{1}{\omega_{n1}}\sin(\omega_{n1}t)\,\dot{\varphi}_{n1}(0) + \cos(\omega_{n1}t)\,\varphi_{n1}(0)\right], \tag{4.82}$$

$$G_{n2}(t) = -\frac{\hbar}{eL_{n2}}\left[\frac{1}{\omega_{n2}}\sin(\omega_{n2}t)\,\dot{\varphi}_{n2}(0) + \cos(\omega_{n2}t)\,\varphi_{n2}(0)\right]. \tag{4.83}$$

In addition, it is easy to show that the analogous relations to Eq. (4.31), namely,

$$\dot{\tilde{Q}}_1 = -\sum_{n=1}^{\infty}\dot{q}_{n1}, \tag{4.84}$$

$$\dot{\tilde{Q}}_2 = -\sum_{n=2}^{\infty}\dot{q}_{n2}, \tag{4.85}$$

also hold. Thus, we can write

$$\dot{\tilde{Q}}_1(t) + \frac{\hbar}{e}\int_0^t dt'\,Y_1(t-t')\,\dot{\tilde{\varphi}}_{g1}(t') = I_{N1}(t), \tag{4.86}$$

$$\dot{\tilde{Q}}_2(t) + \frac{\hbar}{e}\int_0^t dt'\,Y_2(t-t')\,\dot{\tilde{\varphi}}_{g2}(t') = I_{N2}(t), \tag{4.87}$$

where the parameters $\{C_{n1}, L_{n1}\}$ and $\{C_{n2}, L_{n2}\}$ must be chosen such that

$$Y_1(t) = \sum_{n=1}^{\infty}\frac{\cos(\omega_{n1}t)}{L_{n1}} \qquad \rightarrow \qquad Y_1(\omega) = \frac{1}{Z_1(\omega)}, \tag{4.88}$$

$$Y_2(t) = \sum_{n=1}^{\infty}\frac{\cos(\omega_{n2}t)}{L_{n2}} \qquad \rightarrow \qquad Y_2(\omega) = \frac{1}{Z_2(\omega)}, \tag{4.89}$$

and

$$I_{N1}(t) = -\sum_{n=1}^{\infty}G_{n1}(t), \tag{4.90}$$

$$I_{N2}(t) = -\sum_{n=1}^{\infty}G_{n2}(t). \tag{4.91}$$

$$\tag{4.92}$$

4.5.1 Voltage correlation functions

Here we follow steps in analogy to Sec. 4.4.1. First we turn the equation-of-motion of charge into one for phase fluctuations:

$$\tilde{\mathcal{C}} \cdot \begin{bmatrix} \ddot{\tilde{\varphi}}_{g1}(t) \\ \ddot{\tilde{\varphi}}_{g2}(t) \end{bmatrix} + \int_0^t dt' \, \mathcal{Y}(t-t') \begin{bmatrix} \dot{\tilde{\varphi}}_{g1}(t') \\ \dot{\tilde{\varphi}}_{g2}(t') \end{bmatrix} = \frac{e}{\hbar} \begin{bmatrix} I_{N1}(t) \\ I_{N2}(t) \end{bmatrix}. \tag{4.93}$$

Fourier transforming it and substituting the random internal currents by external ones, we get

$$\begin{aligned} \left[-\omega^2 \tilde{\mathcal{C}} + i\omega \, \mathcal{Z}^{-1}(\omega)\right] \cdot \begin{bmatrix} \tilde{\varphi}_{g1}(\omega) \\ \tilde{\varphi}_{g2}(\omega) \end{bmatrix} &= \frac{e}{\hbar} \begin{bmatrix} I_{\text{pert }1}(\omega) \\ I_{\text{pert }2}(\omega) \end{bmatrix} \\ i\omega \, \mathcal{Z}_t^{-1}(\omega) \cdot \begin{bmatrix} \tilde{\varphi}_{g1}(\omega) \\ \tilde{\varphi}_{g2}(\omega) \end{bmatrix} &= \frac{e}{\hbar} \begin{bmatrix} I_{\text{pert }1}(\omega) \\ I_{\text{pert }2}(\omega) \end{bmatrix}, \end{aligned} \tag{4.94}$$

where

$$\mathcal{Z}_t^{-1}(\omega) = \mathcal{Z}^{-1}(\omega) + i\omega \, \tilde{\mathcal{C}}. \tag{4.95}$$

Now, substituting the external currents by appropriate generalized forces,

$$\begin{bmatrix} F_{g1}(\omega) \\ F_{g2}(\omega) \end{bmatrix} = \frac{\hbar}{e} \begin{bmatrix} I_{\text{pert }1}(\omega) \\ I_{\text{pert }2}(\omega) \end{bmatrix}, \tag{4.96}$$

we obtain

$$\begin{bmatrix} \tilde{\varphi}_{g1}(\omega) \\ \tilde{\varphi}_{g2}(\omega) \end{bmatrix} = \mathcal{X}_{\varphi_g}(\omega) \cdot \begin{bmatrix} F_{g1}(\omega) \\ F_{g2}(\omega) \end{bmatrix}, \tag{4.97}$$

where the dynamical susceptibility matrix is given by

$$\mathcal{X}_{\varphi_g}(\omega) = \left(\frac{e}{\hbar}\right)^2 \frac{1}{i\omega} \mathcal{Z}_t(\omega), \tag{4.98}$$

whose imaginary part is given by

$$\mathcal{X}''_{\varphi_g}(\omega) = -\left(\frac{e}{\hbar}\right)^2 \frac{1}{\omega} \operatorname{Re}\left\{\mathcal{Z}_t(\omega)\right\}. \tag{4.99}$$

Assuming that both transmission lines are at the same temperature, the generalized form of the fluctuation-dissipation theorem reads

$$\begin{aligned}\begin{bmatrix} \left\langle|\tilde{\varphi}_{g1}(\omega)|^2\right\rangle & \left\langle\tilde{\varphi}^*_{g1}(\omega)\,\tilde{\varphi}_{g2}(\omega)\right\rangle \\ \left\langle\tilde{\varphi}^*_{g2}(\omega)\,\tilde{\varphi}_{g1}(\omega)\right\rangle & \left\langle|\tilde{\varphi}_{g2}(\omega)|^2\right\rangle \end{bmatrix} &= \int_{-\infty}^{\infty} dt\, e^{-i\omega t} \begin{bmatrix} \langle\tilde{\varphi}_{g1}(t)\,\tilde{\varphi}_{g1}(0)\rangle & \langle\tilde{\varphi}_{g1}(t)\,\tilde{\varphi}_{g2}(0)\rangle \\ \langle\tilde{\varphi}_{g2}(t)\,\tilde{\varphi}_{g1}(0)\rangle & \langle\tilde{\varphi}_{g2}(t)\,\tilde{\varphi}_{g2}(0)\rangle \end{bmatrix} \\ &= \frac{-2\hbar}{1-e^{-\beta\hbar\omega}}\,\mathcal{X}''_{\varphi_g}(\omega). \end{aligned} \tag{4.100}$$

Hence,

$$\begin{bmatrix} \left\langle|\tilde{\varphi}_{g1}(\omega)|^2\right\rangle & \left\langle\tilde{\varphi}^*_{g1}(\omega)\,\tilde{\varphi}_{g2}(\omega)\right\rangle \\ \left\langle\tilde{\varphi}^*_{g2}(\omega)\,\tilde{\varphi}_{g1}(\omega)\right\rangle & \left\langle|\tilde{\varphi}_{g2}(\omega)|^2\right\rangle \end{bmatrix} = \left(\frac{e}{\hbar}\right)^2 \frac{2\hbar}{\omega}\,\frac{1}{1-e^{-\beta\hbar\omega}} \operatorname{Re}\left\{\mathcal{Z}_t(\omega)\right\}. \tag{4.101}$$

We now turn to the fluctuations of the voltage at the dots. Since

$$\begin{pmatrix} \delta U_1 \\ \delta U_2 \end{pmatrix} = \mathcal{C}^{-1} \cdot \begin{pmatrix} \delta\tilde{Q}_1 \\ \delta\tilde{Q}_2 \end{pmatrix} = \frac{\hbar}{e}\,\mathcal{C}^{-1} \cdot \tilde{\mathcal{C}} \cdot \begin{pmatrix} \dot{\tilde{\varphi}}_{g1} \\ \dot{\tilde{\varphi}}_{g2} \end{pmatrix}, \tag{4.102}$$

where

$$\mathcal{C} = \begin{pmatrix} C_1 & 0 \\ 0 & C_2 \end{pmatrix} \tag{4.103}$$

we find

$$\begin{bmatrix} \left\langle|\delta U_1(\omega)|^2\right\rangle & \left\langle\delta U_1^*(\omega)\,\delta U_2(\omega)\right\rangle \\ \left\langle\delta U_2^*(\omega)\,\delta U_1(\omega)\right\rangle & \left\langle|\delta U_2(\omega)|^2\right\rangle \end{bmatrix} = \frac{2\hbar\omega}{1-e^{-\beta\hbar\omega}}\,\mathcal{C}^{-1} \cdot \tilde{\mathcal{C}} \cdot \operatorname{Re}\left\{\mathcal{Z}_t(\omega)\right\} \cdot \tilde{\mathcal{C}}^{\dagger} \cdot \left(\mathcal{C}^{-1}\right)^{\dagger}. \tag{4.104}$$

4.6 Estimate of circuit parameters

We now proceed to make realistic estimates of the effective circuit parameters. The double dot system is maintained at very low temperatures, in the tens of mK [85]. Typically, $k_BT \ll \Delta E$, E_{C1}, E_{C2}, where ΔE is the mean level spacing in the dots. The wires leading to the double quantum dot are thermally anchored to a fridge at several temperature stages (4 K, 1 K, 100 mK, and 10 mK). The transmission line resistance R_L is estimated to be 50 Ω for low temperatures (at or below 4 K) inside the dilution refrigerator, or 250 Ω in the copper leads residing at room temperature [89].

The resistance of the two-dimensional electron gas (2DEG) can be calculated using Drude's theory [90]. The typical electron density in a high-moblity GaAs 2DEG is approximately $n = 10^{11}$ cm^{-2}, which leads to an average Fermi velocity of about $v_F = 10^5$ m/s. At subKelvin temperatures, mean free paths in the 2DEG range from a few to up to one hundred microns [91]. Choosing $l = 10$ μm, we arrive at a relaxation time $\tau = l/v_F \approx 100$ ps, leading to an estimate of the low-temperature conductivity of

$$\begin{aligned} \sigma &= \frac{ne^2\tau}{m^\star} \\ &\simeq 4.2 \times 10^{-2} \quad \text{S}, \end{aligned} \tag{4.105}$$

with $m^\star = 0.067m_e = 0.61 \times 10^{-31}$ kg being the electron effective mass in GaAs. To calculate the resistance, we considered a length $l = 10$ μm and a width $w = 2.5$ μm, yielding a sheet resistance for the 2DEG underneath the gate electrodes

$$\begin{aligned} R &= \rho\frac{l}{w} \\ &\simeq 95 \quad \Omega/\square, \end{aligned} \tag{4.106}$$

where $\rho = 1/\sigma$ is the resistivity of the 2DEG. This resistance is responsible for a dissipative drag effect [92], that for the sake of simplicity will not be considered in our model.

There is still one resistance left to be determined, which is the resistance of the metallic electrodes. This resistance can be determined by

$$R = \rho \frac{l}{bc}, \tag{4.107}$$

where ρ is the resistivity of the electrodes, approximately 0.022×10^{-8} Ωm for a Au electrode at low temperature (< 4 K). If we consider the electrodes to have a 10 μm length and a 30 nm $\times$ 60 nm cross section, we can estimate the electrode resistance to be around 1 Ω, a small value that will also not be considered in our model.

The capacitance C between the transmission line and the 2DEG was estimated by solving the electromagnetic problem of a cylindrical conducting wire of radius $r = 20$ nm placed at a distance of $d = 100$ nm from an infinite grounded conducting plate. Using the method of images, we can estimate the total electric potential of this system by integrating the electric field along the line connecting the centers of the real and the image wires. This results in a capacitance per unit length of 25 aF/μm, and a total capacitance of 250 aF for a wire of 10 μm in length.

Any inductive couplings along our voltage lines can be estimated as follows. For a metal electrode with rectangular cross section, the self inductance is approximated as [93]

$$L_{rod} \sim 2l \left[\ln\left(\frac{2l}{b+c}\right) - \ln \epsilon + \frac{1}{2} \right] \times 10^{-7} \quad \text{H/m}, \tag{4.108}$$

where ϵ is the aspect ratio of the electrode. For an electrode with an aspect ratio of 2, this equation yields $L \approx 1$ pH/μm. Thus, a 10 μm long electrode gives us an inductance of

10 pH. The parameters $C = 250$ aF and $L = 10$ pH, though useful as rough estimates to characterize circuits, will not be used in our model since they are very specific to the given circuit. In fact, in order to estimate these circuit elements more precisely, more physical parameters of the circuit in question would be necessary. To determine the transmission line parameters in our model, we will make use of Eqs. (4.12) and (4.13) from Sec. 4.3 to give us a more general approach where we can model any transmission line given these two operating parameters. To give us a large enough window to operate our qubits, we set our cutoff frequency to $\omega_c = 200 \times 10^9$ rad/s. Table 4.6 summarizes the transmission line parameters that fully describe $Z_i(\omega)$.

Table 4.1: Estimates for the transmission line parameters.

Transmission Line Parameters	
Length l	10 μm
Transmission Line Capacitance C_t	10 pF
Transmission Line Inductance L_t	10 pH
Cutoff Frequency ω_c	200 $\times 10^9$ rad/s
$Z(\omega = 0) = R$	1 Ω

The gate capacitance C_{gi} $(i = 1, 2)$ for each quantum dot is given by

$$C_{gi} = \frac{|e|}{\Delta V_{gi}}. \tag{4.109}$$

If we consider $\Delta V_{gi} \approx 4.5$ mV [84, 85], we find $C_{gi} \approx 40$ aF.

Finally, we now estimate the tunneling parameters between the quantum dots and the 2DEG. These are given by a tunneling junction with an impedance $Z_T = R_T + jX_{C_T}$. We can obtain a lower bound for the tunneling resistance R_T by estimating the inverse of the

Coulomb blockade peak conductance. In the regime $\Gamma \ll k_B T$, $G_{\max}$ is given by [94]

$$G_{\max} = \frac{e^2}{4k_B T} \frac{\Gamma^l \Gamma^r}{\Gamma^l + \Gamma^r}, \tag{4.110}$$

where tunneling rates of an electron through the potential barrier into (or out of) each dot are assumed equal for the sake of simplicity ($\Gamma^l = \Gamma^r$) For an electron temperature in the dot $T \approx 150$ mK and a peak conductance height of $2 \times 10^{-3} e^2/h$ [46], we find the tunneling resistance to be larger than or of the order of 10 MΩ. We can estimate the tunneling capacitance indirectly. We know the expression for the total capacitance of a flat disc to be

$$C_i = 8\epsilon_r \epsilon_0 R. \tag{4.111}$$

Assuming $R \simeq 80$ nm as the radius of the quantum dot and $\epsilon_r \approx 11$ for GaAs at high frequencies, yielding a total capacitance $C_i \approx 60$ aF for each quantum dot.

From the total capacitance we can estimate the interdot capacitance between dots 1 and 2, since

$$C_m = \frac{\Delta V_{gi}^m}{\Delta V_{gi}} C_j, \tag{4.112}$$

where $i \neq j$. For $\Delta V_{gi}^m \approx 0.4$ mV [84, 85], we find $C_m \approx 5$ aF.

The total capacitance for each quantum dot, as seen previously, is the sum of all capacitances attached to the dot. As such, by knowing $C_m = 5$ aF and $C_{Ti} = 40$ aF, we find $C_{gi} \approx 15$ aF.

Using these estimates for the circuit elements, we are able to determine the distributed parameters of our noisy transmission lines. According to Eq. (4.13), if we assume a cutoff frequency of $\omega_c \sim 10^{11}$ Hz, we find $L_{ti} \sim 1$ pH/μm and $C_{ti} \sim 1$ pF/μm.

In principle, one can also consider the ground (2DEG) to be a source of noise, and as such it can also be modeled by means of a frequency-dependent impedance. This would require however an appropriate estimate of the inductance along the 2DEG. In this dissertation, we did not attempt such estimate.

We can also take into account the coupling between the quantum dot leads. This coupling is given by the lumped capacitance C_{12}, as shown in Fig. 4.1. This capacitance was estimated to be approximately 20 aF by means of numerical multipole expansion calculations performed by a field solver software [95]. We present more details of these numerical calculations in Appendix D.

We summarize below in Table 4.6 the relevant circuit parameters necessary to fully characterize the DQD setup.

Table 4.2: Estimates for the DQD circuit parameters.

Circuit Parameters	
Transmission Line Capacitance C_{ti}	1 pF/μm
Transmission Line Inductance L_{ti}	1 pH/μm
Interdot Capacitance C_m	5 aF
Tunneling Capacitance C_{Ti}	40 aF
Tunneling Resistance R_{Ti}	$\gtrapprox$ 10 MΩ
Gate Capacitance C_{gi}	15 aF
Total quantum dot capacitance C_i	60 aF
Capacitive coupling between transmission lines C_{12}	$\simeq$ 20 aF
Electrode Resistance R_i	1 Ω

$i = 1, 2$, corresponding to each of the quantum dots.

4.7 Bounds on decoherence rates and Q factors

Through the fluctuation-dissipation theorem we can relate to the impedance $Z_{1,2}(\omega)$ a source of electromagnetic gate fluctuations $\delta V_{g1,2}$. These gate fluctuations $\delta V_{gi} = Q_{0,i}/C_{gi} (i = 1, 2)$ can be determined through the diagonalization of the Hamiltonian in Eq. (4.14). Using the method described in Appendix C, we are able to rewrite Eq. (4.14) in the second quantization formalism

$$H_B = \sum_{i=1,2} \int_0^1 dx \hbar \omega_{xi} \left(\hat{a}_{xi}^\dagger \hat{a}_{xi} + \frac{1}{2} \right) \tag{4.113}$$

as well as the dispersion relation $\omega_{xi} = \omega_{ci} \sin(\pi x/2)$ with a high-frequency cutoff of $\omega_{ci} = 2/\sqrt{L_{ti} C_{ti}}$.

We consider in this paper the case of Johnson-Nyquist noise [83]. The Fourier transform of the time correlator of the gate voltage fluctuations contain the information necessary to quantify the decoherence originating from these gate voltages, as seen in Eq. (4.104). The energy relaxation rate γ_1 is found to be

$$\begin{aligned} \gamma_1 &= \frac{\omega}{R_K} \coth(\hbar\omega/2k_BT) \Big\{ \left\langle |\delta U_1(\omega)|^2 \right\rangle + \left\langle |\delta U_2(\omega)|^2 \right\rangle \\ &\quad - \langle \delta U_1^*(\omega)\, \delta U_2(\omega) \rangle - \langle \delta U_2^*(\omega)\, \delta U_1(\omega) \rangle \Big\}, \end{aligned} \tag{4.114}$$

where R_K is the resistance quantum ($= h/e^2 \simeq 25.8\text{k}\Omega$). From this expression we can easily calculate the energy relaxation and dephasing times:

$$T_1 = 1/\gamma_1 \tag{4.115}$$

$$= \frac{R_K}{\omega} \frac{\tanh(\hbar\omega/2k_BT)}{\left\langle |\delta U_1(\omega)|^2 \right\rangle + \left\langle |\delta U_2(\omega)|^2 \right\rangle - \langle \delta U_1^*(\omega)\, \delta U_2(\omega) \rangle - \langle \delta U_2^*(\omega)\, \delta U_1(\omega) \rangle}, \tag{4.116}$$

and

$$T_2 = 2T_1, \tag{4.117}$$

for bosonic baths in the Born-Markov approximation. Finally, the quality factor is defined as

$$\begin{aligned} Q &= \frac{\omega_{\rm osc}}{\pi\gamma_1} && (4.118)\\ &= \frac{R_K}{\pi}\frac{\tanh(\hbar\omega/2k_BT)}{\left\langle|\delta U_1(\omega)|^2\right\rangle + \left\langle|\delta U_2(\omega)|^2\right\rangle - \langle\delta U_1^*(\omega)\,\delta U_2(\omega)\rangle - \langle\delta U_2^*(\omega)\,\delta U_1(\omega)\rangle}, && (4.119)\end{aligned}$$

where $\omega_{\rm osc}$ is the frequency of quantum oscillations observed in the DQD system, as defined by [83]

$$\omega_{\rm osc} = \sqrt{2\Delta\left(2\Delta + \frac{\gamma_2}{2}\right) - \frac{\gamma_1^2}{4}}, \tag{4.120}$$

with Δ being the potential barrier height between quantum dots, as shown in Eq. (4.6), and γ_2 being defined as

$$\gamma_2 = -\fint_0^\infty \frac{dy}{y^2-1}\,\nu(2\Delta y)\coth\left(\frac{\Delta y}{T}\right), \tag{4.121}$$

where ν is the bath spectral function, defined as

$$\begin{aligned} \nu(\omega) &= \frac{2}{\pi}\frac{\omega}{R_K}\Big\{\left\langle|\delta U_1(\omega)|^2\right\rangle + \left\langle|\delta U_2(\omega)|^2\right\rangle \\ &\quad - \langle\delta U_1^*(\omega)\,\delta U_2(\omega)\rangle - \langle\delta U_2^*(\omega)\,\delta U_1(\omega)\rangle\Big\}. \end{aligned} \tag{4.122}$$

The operating frequency $\omega = 2\Delta/\hbar$ is fed to the circuit by the voltage generators and carried through the gates. The other terms in Eq. (4.120), as it turns out, are small enough corrections to the operating frequency so that they may be ignored. Thus, from now on we will assume $\omega_{\rm osc} = \omega$.

We will now analyze in detail two different scenarios: one where the transmission lines are decoupled, while the other includes the capacitive coupling C_{12} between transmission lines, as seen in Fig. 4.1.

4.7.1 Case (i): Decoupled transmission lines

It is useful to look at the case where there is no coupling between the electrodes. The decoherence introduced by the electromagnetic voltage fluctuations can still be analyzed using Eqs. (4.114) through (4.119), but some simplifications to the impedance matrix are now possible. This case corresponds to having $C_{12} = 0$, so the matrix $\mathcal{Z}$ from Eq.4.72 is reduced to

$$\mathcal{Z} = \begin{pmatrix} Z_1\left[1+\frac{C_m}{C_1}\right] & -Z_1\frac{C_m}{C_2} \\ -Z_2\frac{C_m}{C_1} & Z_2\left[1+\frac{C_m}{C_2}\right] \end{pmatrix}. \tag{4.123}$$

In this case we observe the highest possible quality factors for our double-quantum-dot setup, as seen in Figs. 4.5, and 4.6.

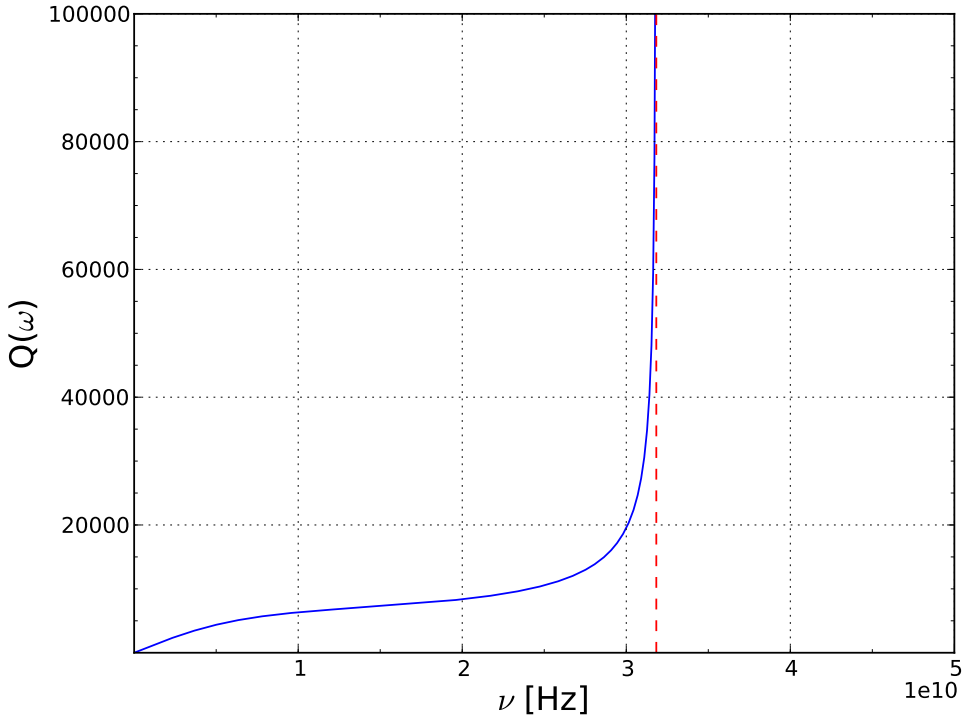

Figure 4.5: Qubit quality factor as a function of frequency for two decoupled semi-infinite transmission lines, with temperature $T = 150$ mK and the circuit parameters presented in Table 4.6.

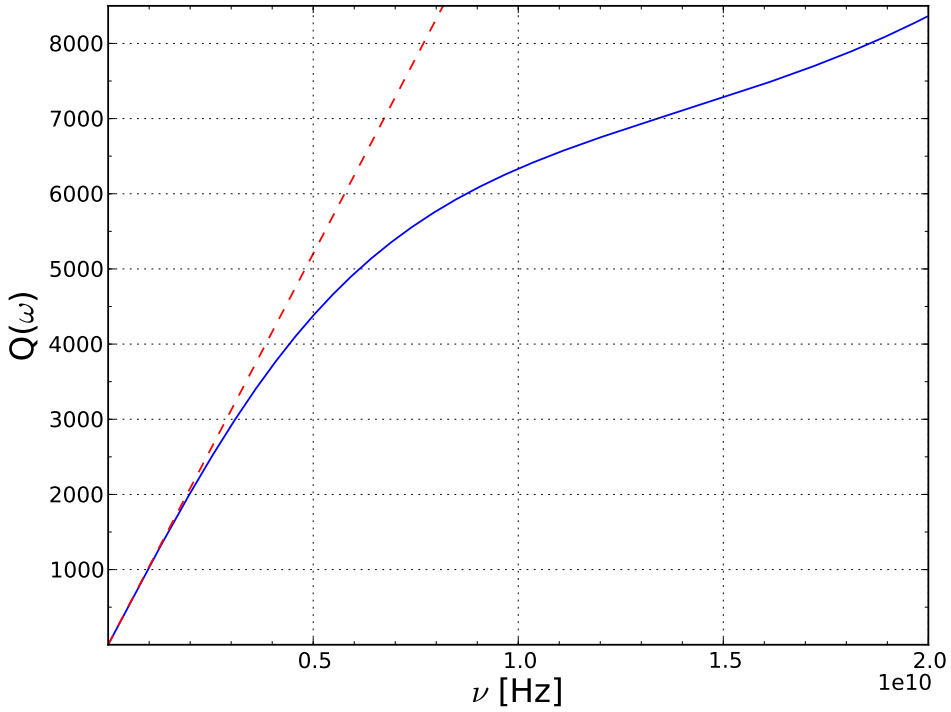

Figure 4.6: Qubit quality factor as a function of frequency for $\nu < 20$ GHz and two decoupled semi-infinite transmission lines with the same parameter values as in Fig. 4.5.

If we look back at Eq. (4.119) and take its asymptotic limit for low frequencies, it is important to first notice that

$$\tanh(\hbar\omega/2k_BT) \approx \hbar\omega/2k_BT. \tag{4.124}$$

Equation (4.123) is then reduced to

$$\mathcal{Z} = \begin{pmatrix} R_1\left[1+\frac{C_m}{C_1}\right] & -R_1\frac{C_m}{C_2} \\ -R_2\frac{C_m}{C_1} & R_2\left[1+\frac{C_m}{C_2}\right] \end{pmatrix}, \tag{4.125}$$

where $R_i = \mathcal{Z}(\omega = 0) = \sqrt{L_{ti}/C_{ti}}$, as reported earlier, and with the assumption that $C_1 = C_2$, $C_{g1} = C_{g2}$, and $R_1 = R_2$. This, combined with the fact that $\mathrm{Re}\{\mathcal{Z}_t(\omega)\} \to \mathrm{Re}\{\mathcal{Z}(\omega)\}$

for $\omega \to 0$, yields

$$\lim_{\omega \to 0} Q(\omega) = (8.9 \times 10^{-7}[s])\nu, \tag{4.126}$$

where we notice a linear dependence of Q with respect to ν, as can also be evidenced in the log-log graph shown in Fig. 4.7. While R_i is an important modeling parameter for the transmission lines, it is also clear that C_{ti} and L_{ti} ultimately influence how quickly this linear regime establishes itself once we move to lower frequencies.

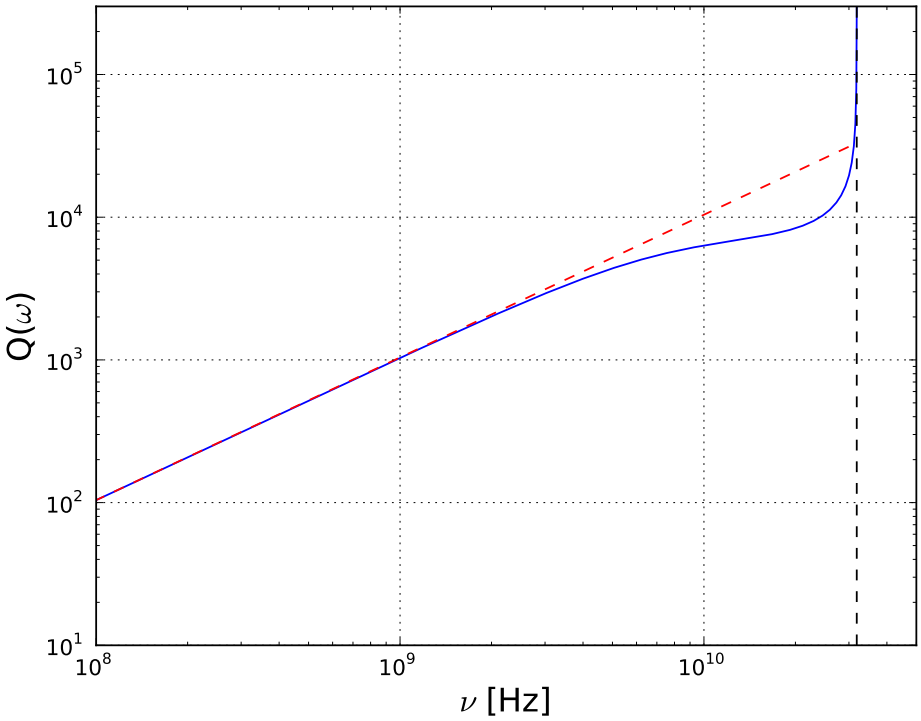

Figure 4.7: Quality factor as a function of frequency for two decoupled transmission lines represented in a logarithmic scale with the same parameter values as in Fig. 4.5.

Turning our attention now to higher frequencies, we notice an important characteristic of the transmission lines. The real part of the transmission line impedance $\mathrm{Re}\{\mathcal{Z}(\omega)\}$ has

a cutoff frequency given by $\nu_c = \omega_c/2\pi$. In Fig. 4.8, it can be seen that as $\omega \to \omega_c$, $\mathrm{Re}\{\mathcal{Z}(\omega)\} \to 0$, making $\mathrm{Re}\{\mathcal{Z}_t(\omega)\} \to 0$ as well, causing the quality factor Q to diverge at $\omega = \omega_c$.

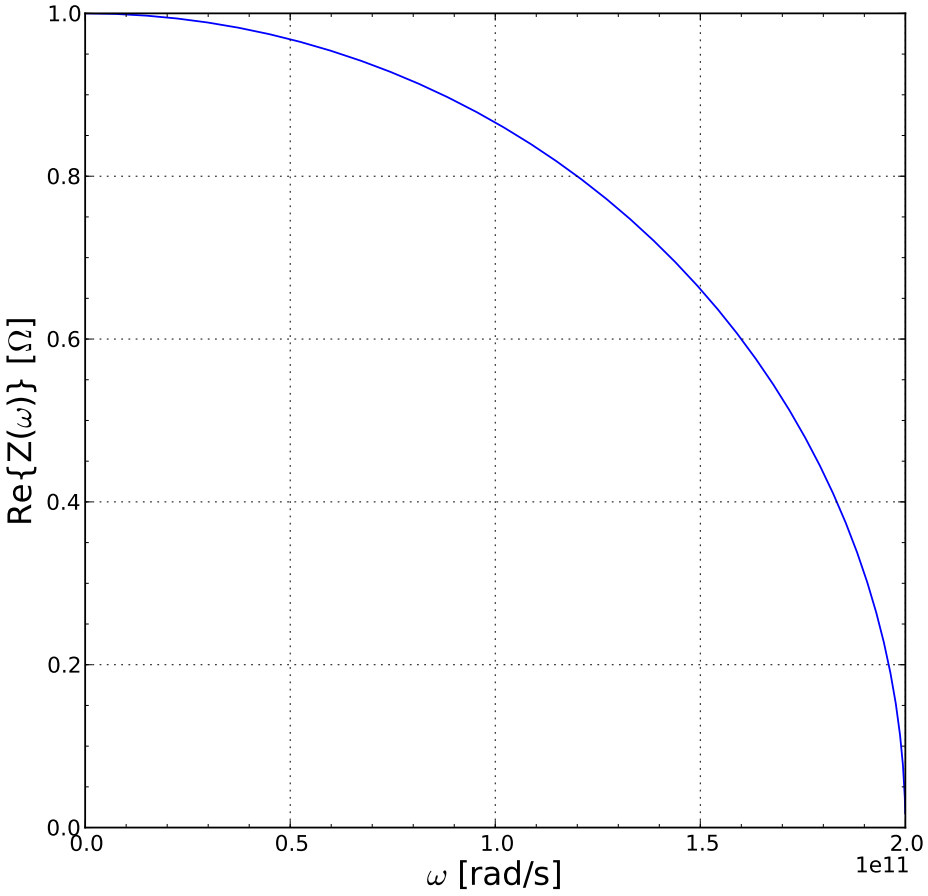

Figure 4.8: Real part of the impedance $\mathcal{Z}(\omega)$ as a function of the frequency ω. Transmission line parameters are defined in Table 4.6.

4.7.2 Case (ii): Capacitively coupled transmission lines

Inserting now the inter-capacitive coupling C_{12} estimated in Section 4.6, we obtain the quality factor Q as a function of frequency ν shown in Figs. 4.9, 4.10, and 4.11. In Fig. 4.9, we can clearly observe the quality factor diverge at the frequency $\nu_c \simeq 320$ GHz, corresponding to the cutoff frequency.

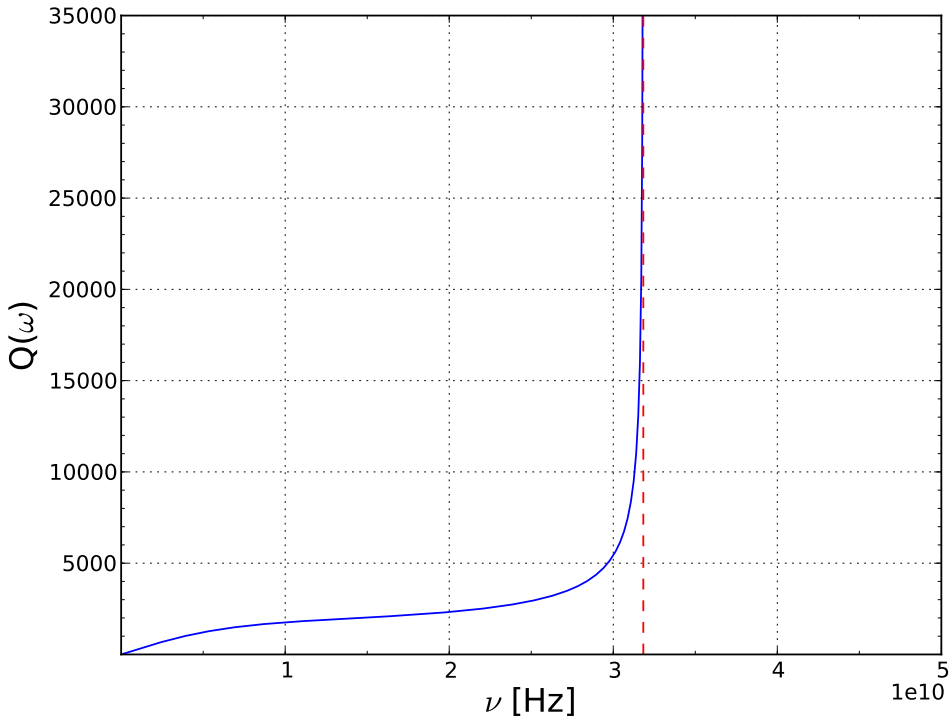

Figure 4.9: Qubit quality factor as a function of frequency, with temperature $T = 150$ mK. The circuit parameters utilized are presented in Table 4.6.

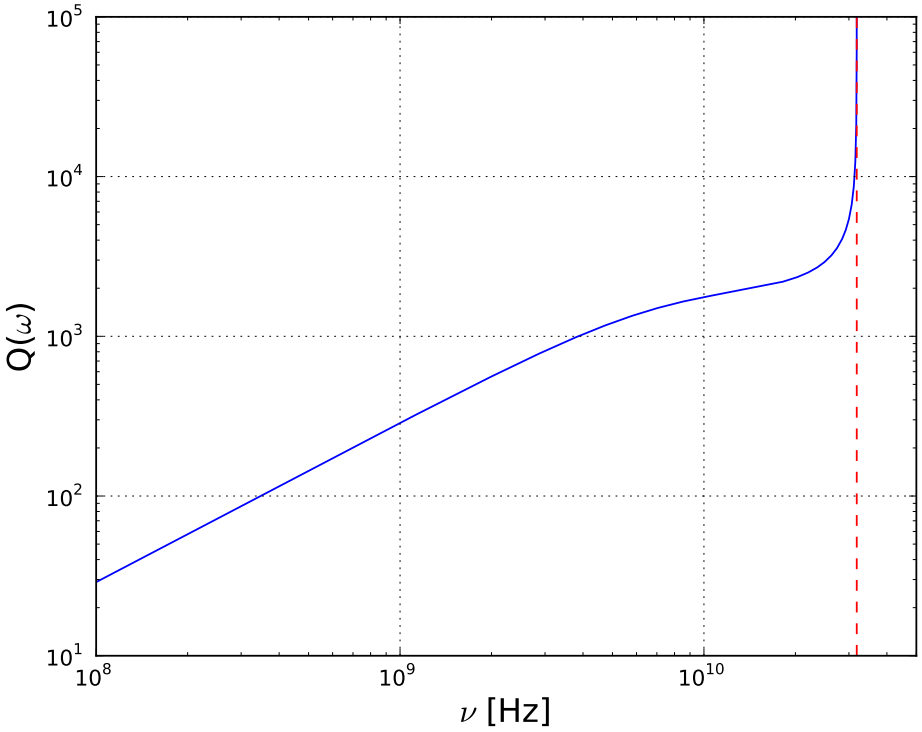

Figure 4.10: Qubit quality factor as a function of frequency represented in a logarithmic scale. The circuit parameters utilized are the same as in Fig. 4.9.

From now on we shall restrict our discussion to operating frequencies under 20 GHz (Fig. 4.11), which are more realistic for practical implementations of qubit operations.

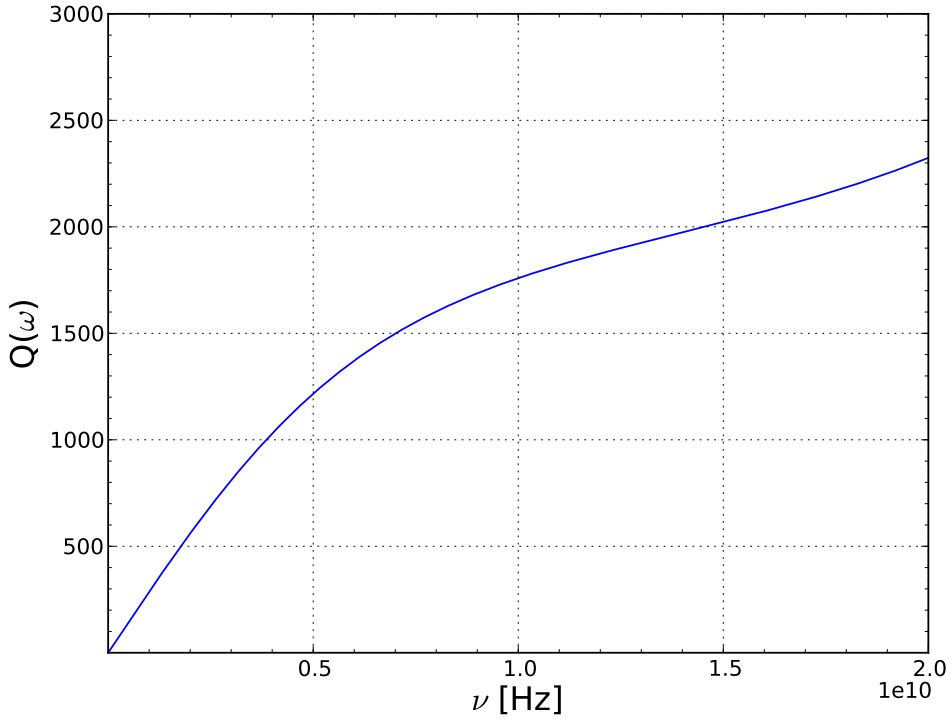

Figure 4.11: Quality factor as a function of frequency for $\nu < 20$ GHz and two decoupled semi-infinite transmission lines with the same parameter values as in Fig. 4.9.

It is interesting to observe the influence of temperature on the decoherence introduced into the system by voltage fluctuations. We show below, in Figs. 4.12 and 4.13, a family of Q factor curves as a function of operating frequency ν for temperatures ranging from 50 mK all the way to room temperature. As temperature increases, more environmental modes are available for the system to couple with, effectively increasing dissipative effects.

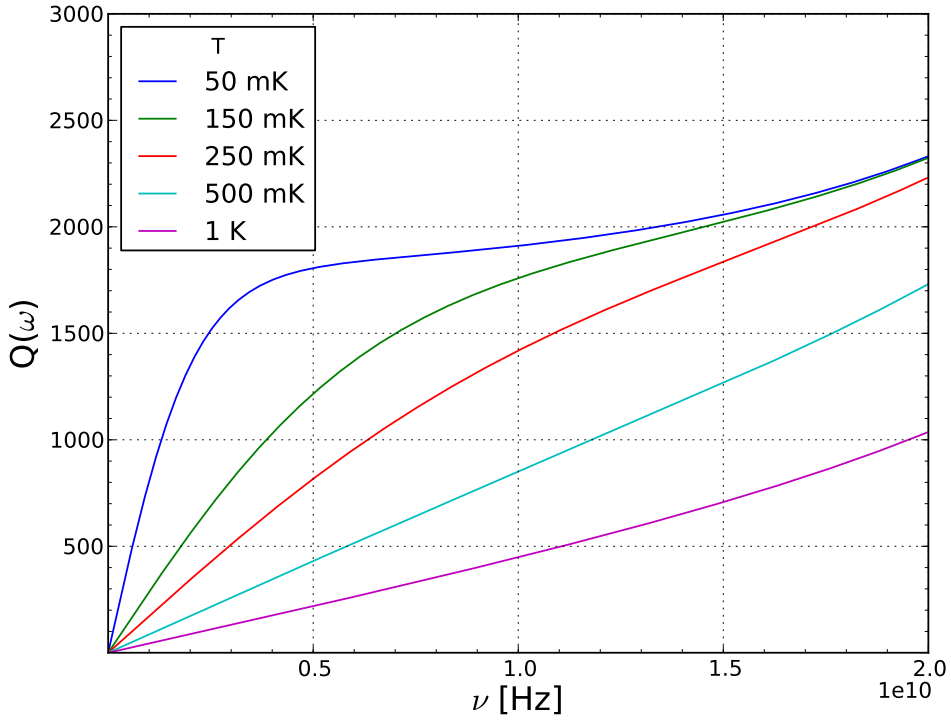

Figure 4.12: Qubit quality factor as a function of operating frequency for temperatures $T = 50, 150, 250, 500$ mK, and 1 K. The circuit parameters utilized are presented in Table 4.6.

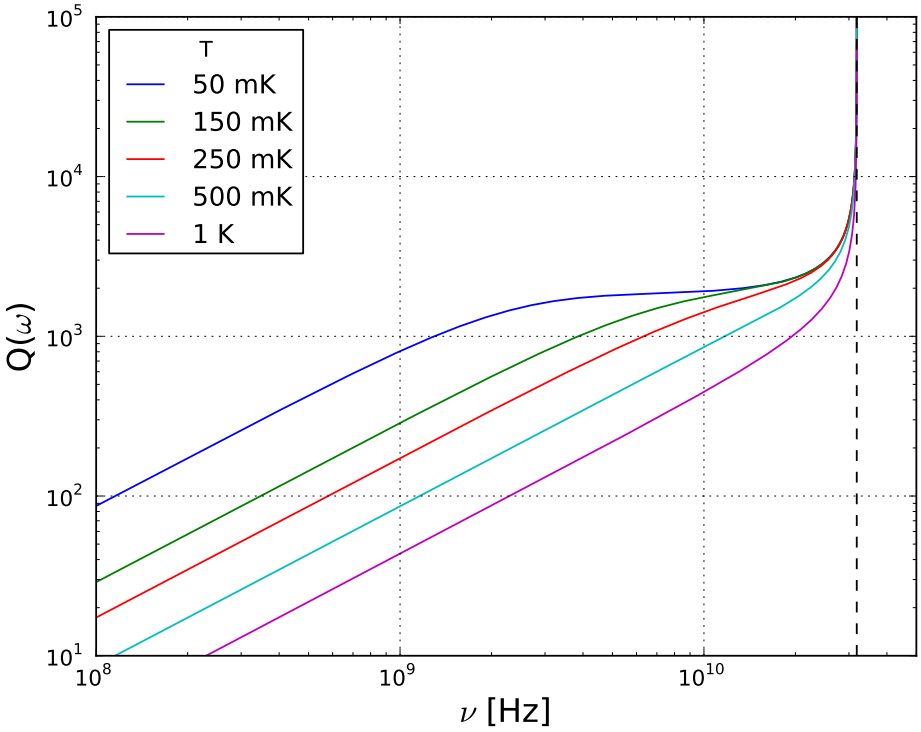

Figure 4.13: Logarithmic representation of the qubit quality factor as a function of operating frequency for temperatures $T = 50, 150, 250, 500$ mK, and 1 K. The circuit parameters utilized are presented in Table 4.6.

We can also observe the influence of the inter-capacitive coupling C_{12} on the quality factor, as seen in Figs. 4.14 and 4.15. For weaker coupling, i.e., smaller C_{12}, the quality factors are higher, as C_{12} approaches the limiting case of decoupled lines. Note that $Q(\omega)$ will still not reach the same levels of the decoupled case due to the presence of the capacitance C_m.

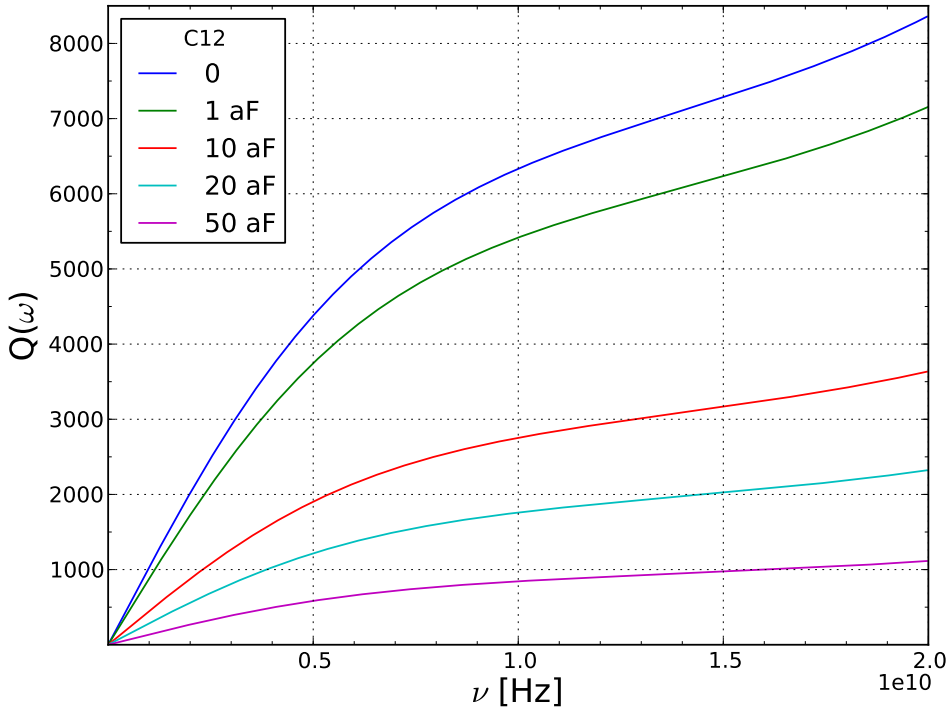

Figure 4.14: Quality factor as a function of operating frequency for temperature $T = 150$ mK and inter-capacitive couplings $C_{12} = 0$, 1.3 , 10, 20, and 50 aF. The circuit parameters utilized are presented in Table 4.6.

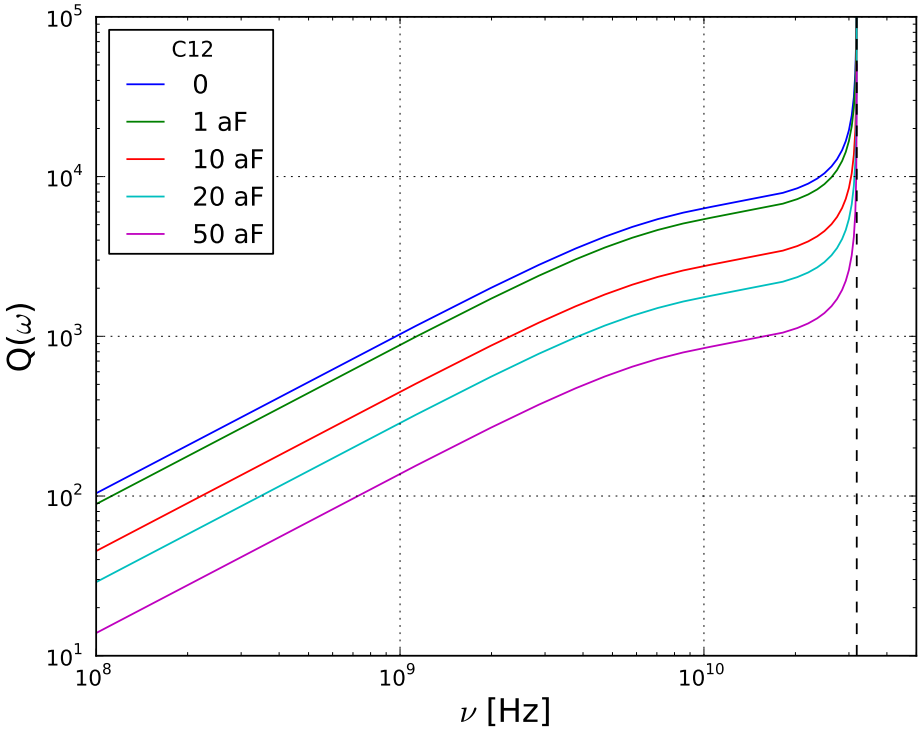

Figure 4.15: Logarithmic representation of the qubit factor as a function of operating frequency for temperature $T = 150$ mK and inter-capacitive couplings $C_{12} = 0$, 1.3, 10, 20, and 50 aF. The circuit parameters utilized are the same as in Fig. 4.14.

We present below in Tables 4.7.2 and 4.7.2 the results of calculations for the decoherence time T_2 and the Q factor for several different values of temperature T and inter-capacitive coupling C_{12}. It is easy to understand why higher temperatures degrade decoherence times in qubit operations. We can consider two extreme cases, namely, one where the electrical leads are inside a dilution refrigerator and another where they are at room temperature. We will also consider an operating frequency $\nu = \omega/2\pi$ of 10 GHz. First, let us assume that leads connected to the gate electrode are inside the dilution refrigerator. In this case,

a temperature $T = 150$ mK results in a relaxation time $T_1 = 88$ ns and a decoherence time of $T_2 = 176$ ns. This scenario yields a quality factor of $Q \approx 1,760$. If we consider now the case where the leads are at room temperature, we estimate the relaxation time and the dephasing time to be approximately 76 ps and 152 ps, respectively, resulting in a quality factor of $Q \simeq 1.5$, more than 1000 times lower.

A much more interesting analysis stems from varying the inter-capacitive coupling between the transmission lines. For higher values of C_{12}, it would be intuitive to expect both transmission lines to be more strongly coupled, meaning that decoherence in the system would be weaker since voltage fluctuations in the two lines would be correlated. As it turns out, however, the stronger coupling between transmission lines results in larger off-diagonal terms in the matrix of voltage correlations defined in Eq. (4.104). If we look at Eq. (4.119) once more, it is easy to see that larger off-diagonal terms subtracted from the main diagonal correlation terms results in smaller Q factors, as evidenced by the behavior of the family of Q factor curves in Fig. 4.14 for different values of inter-capacitive coupling and the calculated values presented in Table 4.7.2.

Table 4.3: Estimates for the dephasing times T_2 for different values of temperature T and interline capacitive coupling C_{12}.

Dephasing time T_2 [ns]					
T [K]	C_{12} [aF]				
	0	$\sim$1	10	20	50
50×10^{-3}	688	588	300	191	92
150×10^{-3}	633	542	275	176	84
250×10^{-3}	511	437	222	142	68
500×10^{-3}	306	262	133	85	41
1	161	138	70	45	22
300	0.55	0.47	0.24	0.15	0.07

Table 4.4: Estimates of Q factors for different values of temperature T and inter-capacitive coupling C_{12}.

Q factor					
T [K]	C_{12} [aF]				
	0	$\sim$1	10	20	50
50×10^{-3}	6878	5884	2990	1910	917
150×10^{-3}	6333	5418	2753	1760	844
250×10^{-3}	5108	4369	2220	1418	681
500×10^{-3}	3059	2617	1329	850	408
1	1614	1380	702	448	215
300	5.5	4.7	2.4	1.5	0.7

CHAPTER FIVE: CONCLUSION

In this chapter we present conclusions provenient from our study of decoherence originating from coupling to phonon modes and electromagnetic fluctuations, as seen in Chapters 3 and 4, respectively. We also discuss ideas for future research building upon our conclusions. Finally, we briefly discuss another leading candidate for dominant decoherence source in solid state charge based qubit systems, namely interactions between electrons in the quantum dots and fluctuating charges trapped in the substrate.

5.1 Phonon coupling

In this dissertation I have shown that, whereas there are no simple ways to completely protect charge qubits based on quantum dots from decoherence by gapless bosonic modes propagating in the substrate, a homogeneous charge distribution throughout the qubit is the most advantageous setup and provides the best possible protection against decoherence. This result applies not only to the charge qubits in semiconductor-heterostructures that we focused on here, but, in principle, to charge qubits in general. Whereas certain aspects of the discussion need to be changed for, say, self-assembled quantum dots, single-donor charge qubits [48], or Si-based quantum dot structures [47], this does not affect the universal mechanism underlying our central result, namely that a specific (homogeneous) charge distribution within the qubit enables the cancellation of (certain) decoherence modes.

Contrary to spin-based quantum dot qubits, where decoherence-free subspaces can be created by combining quantum dots into logical units, charge-based qubits are much more

difficult to isolate from the environment. In order to have decoherence-free subspaces for charge qubits one would need to restrict the operation to a subspace where charge is homogeneously distributed in space, no matter which basis states are chosen. However, this contradicts the very nature of a charge qubit (where readout depends on charge imbalance) and thus cannot be achieved. In our example of the three-dot qubit these facts become evident in the existence of two phonon modes that *cannot cancel due to geometric constraints* inherent to the qubit.

Decoherence can be mitigated in a number of other ways. For instance, for the three-dot qubit case we have studied, a substantial improvement with respect to the double-dot qubit can be achieved due to the lower frequency of operation and to an enhancement of the relaxation time by a factor of three.

Another effective way to reduce the coupling to gapless bosonic modes is to choose a computational basis with a multipole charge configuration. As we have shown, the multipole geometry attenuates the coupling to long wavelength acoustic phonons by a factor proportional to a power law of the operation frequency. This power law grows rapidly with the multipole order. Thus, multipole configurations of charge can lead to quality factors enhanced by orders of magnitude in comparison to those obtained for double-dot qubits. However, the effect is reversed at high frequencies of operation. The crossover frequency separating the two regimes is given by the inverse traversal time for a phonon to propagate across the qubit. For typical GaAs setups, this time is of the order of 30 ps (for dots 120 nm apart), indicating a crossover frequency in the range of 30 GHz. Since tunnel amplitudes usually vary from tens to a few hundreds of μeV, yielding quantum oscillations of about

2-20 GHz, there is a real advantage in moving toward multiple-dot qubits for current setups. However, since phonons are not the only leading mechanism for decoherence in charge qubits [60], as operation frequencies go down other sources of decoherence, not necessarily modeled by bosonic environments, may become dominant. In that case multiple-dot qubits might become less appealing.

Finally, it is worth mentioning that a recent work has shown that gate optimization is also a very effective way of minimizing the coupling to bosonic environments in solid-state quantum dot charge qubits subject to decoherence [69]. Optimal control theory may be employed to design such gates that will in turn control the qubit system. Since the system takes some time to become entangled with the environment, it is possible during this time to channel back quantum coherence from the environment to the system by using appropriately designed control.

5.2 Electromagnetic fluctuations

In this dissertation I have also modeled noise introduced by gate voltage fluctuations in double quantum dot systems. I attempted to model the circuits leading to the DQD in a way that put us as close to real experimental values as possible, while still being able to estimate all the relevant parameters and calculate decoherence rates and quality factors. I chose to place our noise sources in our gates because we believe they give the largest contribution to decoherence during qubit operations. For additional considerations, noise sources could also be placed, for example, in the drain and source electrodes.

I have estimated the effect of fluctuations in the electrodes feeding the quantum dots

and shown the influence that parameters such as temperature and inter-capacitive coupling between electrodes have on decoherence in qubit operation. I have also shown that, similarly to decoherence by phonon coupling, temperature degrades coherence in the state superpositions, reinforcing the need for efficient refrigeration of the leads. This effect can be explained analogously to the radiation of a black body, which increases with temperature.

Contrary to what was initially expected, it was found that a stronger inter-capacitive coupling between electrodes actually introduces stronger decoherence in the qubit system. Thus, in order to mitigate this effect, it is important to keep the leads gating each quantum dot in the system as isolated as possible from each other.

I have ultimately found that electromagnetic fluctuations in DQD systems do not introduce a dominating decoherence effect. The quality factors calculated for our system at low temperature (~ 5000) are still well above the Q factors found in systems under the effect of phonon coupling (~ 50) [60, 61, 62, 100]. If we compare these results with the experimental results ($\sim 3 - 9$) for Q factors, the discrepancy is even larger [44, 46, 47].

There are a few possible refinements to the model presented in this dissertation. One such improvement includes adding the electrical resistance in the leads, which in practice requires the use of a lossy transmission line model for the effective circuit. It may also be important to take into account the drag effect on the leads due to the proximity to the 2DEG. This effect will change the effective circuit parameters, thus influencing the calculation of relaxation and dephasing times.

The disagreement between theoretical estimates and measured decoherence times in charge based DQD system leads us to believe that there must be another noise source that

accounts for the short decoherence times observed in these systems. However, in order to identify the leading decoherence mechanism in charge-based qubits, it would be very helpful if the dependence of the Q-factor on the operating frequency ν were measured, as this would yield the spectral function of the (possibly) bosonic environmental modes, so we could determine whether the the dissipative process occuring in these systems is mainly subohmic, ohmic or superohmic. With this information in hand, one could perhaps trace back the physical process underlying the decoherence mechanism. A candidate for such source is the presence of fluctuating background charges trapped in the insulating substrate or at the GaAS/GaAlAs interface.

Finally, there is also a need to estimate the effects of environmental electromagnetic fluctuations in the case of spin-based qubit systems.

5.3 Concluding remarks

The question of what are the dominating mechanisms of decoherence in semiconducting quantum dot qubit systems remains open. This remains an obstacle for building large scale quantum computers with this technology. It is thus important to turn our attention to other possible candidates as dominating decoherence processes besides the ones considered in this dissertation. One such candidate is the presence of fluctuating background charges (FBCs) embedded in an insulating layer close to the electronic bath. The fluctuating charges create a dynamical electric field that affect qubit states. This effect can be seen in both semiconductor and superconductor charge-based qubits alike.

It has been argued that electrostatic coupling to fluctuating background charges hy-

bridized with the conduction electrons in the reservoir may contribute significantly to the decoherence of a double quantum dot charge qubit. Models for FBCs have been developed [101, 102, 103, 104, 105, 106, 107, 108, 109] in analogy with the spin-fluctuator model of the spectral diffusion in glasses. These models, however, underestimated the efficiency of this noise source since they do not account for a large enough number of effective fluctuators so that decoherence originating from them could be experimentally observed. On the other hand, decoherence and dephasing with origin in these fluctuators has been already experimentally observed in the context of superconducting qubits [110], which has led to the conclustion that these models were still incomplete. Further research of this decoherence mechanism has recently [111] yielded new results. It has been found that by including short-range Coulomb interactions in those previous models enhances the number of effective fluctuators and their contributions to decoherence.

Further work remains to be done in estimating numerical values for the relaxation and dephasing rates originated in qubit systems affected by FBCs. It will be valuable to know whether these estimates will reconcile with the experimental measurements performed in these systems, establishing fluctuating background charges as the dominant decoherence mechanism in charge qubit systems. If this is not the case, further study will be necessary in identifying other possible candidates that may help circumvent this important obstacle in designing a full scale quantum computer.

APPENDIX A: THE TWO-QUBIT REDUCED HAMILTONIAN

The Hamiltonian of two three-dot qubits coupled by their bases [see Fig. 3.3(b)] with inter-qubit couplings t' and t'' has the following matrix form in the basis of Eqs. (3.11)-(3.20) (the lower off-diagonal block is omitted):

$$H_{\mathrm{I-II}}^{\mathrm{base}} = \begin{pmatrix}
0 & 0 & 0 & 0 & -\frac{t'e^{i\beta}}{3} & -\frac{t''e^{-i\beta}}{3} & \frac{t'e^{-i\beta}}{3} - \frac{t''e^{i\beta}}{3} & \frac{t''e^{i\beta}}{3} & \frac{t'e^{-i\beta}}{3} & \frac{t'e^{i\beta}}{3} - \frac{t''e^{-i\beta}}{3} \\
0 & 0 & 0 & 0 & -\frac{t'e^{-i\beta}}{3} & \frac{t''e^{i\beta}}{3} & \frac{t'}{3} - \frac{t'\prime}{3} & \frac{t''e^{i\beta}}{3} & \frac{t'e^{-i\beta}}{3} & \frac{t'}{3} - \frac{t'\prime}{3} \\
0 & 0 & 0 & 0 & -\frac{t'e^{i\beta}}{3} & -\frac{t''e^{-i\beta}}{3} & \frac{t'}{3} - \frac{t'\prime}{3} & \frac{t''e^{-i\beta}}{3} & \frac{t'e^{i\beta}}{3} & \frac{t'}{3} - \frac{t'\prime}{3} \\
0 & 0 & 0 & 0 & -\frac{t'e^{-i\beta}}{3} & -\frac{t''e^{i\beta}}{3} & \frac{t'e^{i\beta}}{3} - \frac{t''e^{-i\beta}}{3} & \frac{t''e^{-i\beta}}{3} & \frac{t'e^{i\beta}}{3} & \frac{t'e^{-i\beta}}{3} - \frac{t''e^{i\beta}}{3} \\
 & & & & U_i & v & -v & 0 & 0 & 0 \\
 & & & & v & U_i & v & 0 & 0 & 0 \\
 & & & & -v & v & U_i & 0 & 0 & 0 \\
 & & & & 0 & 0 & 0 & U_i & v & -v \\
 & & & & 0 & 0 & 0 & v & U_i & v \\
 & & & & 0 & 0 & 0 & -v & v & U_i
\end{pmatrix} \tag{A.1}$$

[Note that the Hamiltonian for the tip-tip configuration is recovered by setting $t'' = 0$ in Eq. (A.1).] This Hamiltonian can be projected onto the two-qubit computational subspace by means of a Schrieffer-Wolff transformation. From Eq. (A.1), we see that the Hamiltonian has the form $H_{\mathrm{I-II}}^{\mathrm{base}} = H_0 + H_1$, where

$$H_0 = \begin{pmatrix} 0 & 0 \\ 0 & M \end{pmatrix}, \quad H_1 = \begin{pmatrix} 0 & T \\ T^\dagger & 0 \end{pmatrix}, \tag{A.2}$$

and M and T are 6×6 and 4×6 matrices, respectively. Performing the Schrieffer-Wolff transformation and expanding to second order in H_1[76], we get $\tilde{H}_{\mathrm{I-II}}^{\mathrm{base}} \approx H_0 + (1/2)[S, H_1]$,

where

$$S = \begin{pmatrix} 0 & -T\,M^{-1} \\ -M^{-1}\,T^{\dagger} & 0 \end{pmatrix}. \tag{A.3}$$

Thus the Hamiltonian has the block diagonal structure

$$\tilde{H}^{\rm base}_{\rm I-II} \approx \begin{pmatrix} H^{\rm red}_{\rm I-II} & 0 \\ 0 & M \end{pmatrix}, \tag{A.4}$$

where $H^{\rm red}_{\rm I-II} = -T\,M^{-1}\,T^{\dagger}$. The matrix M can be broken into two identical 3×3 diagonal blocks,

$$M = \begin{pmatrix} B & 0 \\ 0 & B \end{pmatrix}, \tag{A.5}$$

and T can be broken into two distinct 4×3 blocks,

$$T = \begin{pmatrix} T_{\rm I} & T_{\rm II} \end{pmatrix}. \tag{A.6}$$

As a result, $H^{\rm red}_{\rm I-II} = -T_{\rm I}\,B^{-1}\,T^{\dagger}_{\rm I} - T_{\rm II}\,B^{-1}\,T^{\dagger}_{\rm II}$. After some algebra, one finds that

$$B^{-1} = \frac{1}{3}\begin{pmatrix} 2u_1+u_2 & u_1-u_2 & -u_1+u_2 \\ u_1-u_2 & 2u_1+u_2 & u_1-u_2 \\ -u_1+u_2 & u_1-u_2 & 2u_1+u_2 \end{pmatrix}, \tag{A.7}$$

where $u_1 = (U_i+v)^{-1}$ and $u_2 = (U_i-2v)^{-1}$. The structure of B^{-1} can be substantially simplified by assuming $v \ll U_i$ and neglecting v. This yields $H^{\rm red}_{\rm I-II} = (-1/U_i)\left(T_{\rm I}\,T^{\dagger}_{\rm I} + T_{\rm II}\,T^{\dagger}_{\rm II}\right)$. Carrying out the matrix multiplications and setting $t'' = 0$, we obtain Eq. (3.23).

APPENDIX B: SOLUTION TO THE INFINITE LADDER NETWORK

To find the solution for an infinite transmission line, we start with a more general model of an infinite ladder network, as seen in Ref. [87].

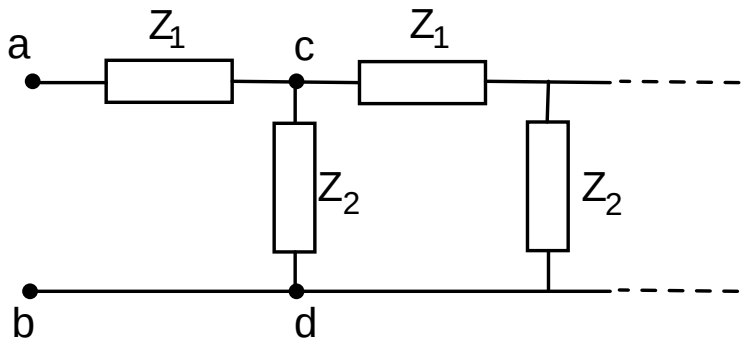

Figure B.1: Infinite ladder network.

Consider the infinite ladder network depicted in Fig. B.1. The key idea is that when we connect an extra section to the first two terminals of the infinite network, the resultant circuit is still the same infinite network. If we define the impedance between terminals a and b to be $Z_0(\omega)$, we can easily verify that the impedance between terminals c and d is also $Z_0(\omega)$, as seen in Fig. B.2.

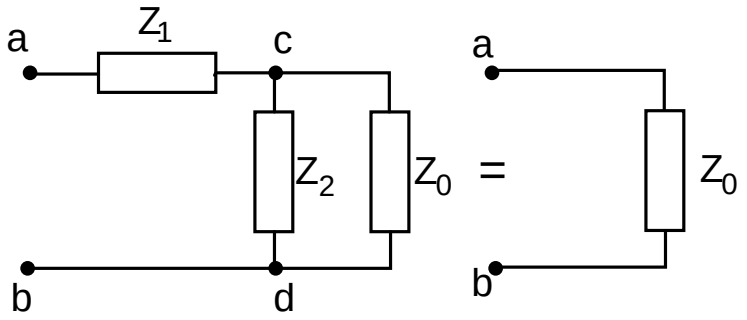

Figure B.2: Effective impedance of an infinite ladder network.

By combining the impedances $Z_1(\omega)$ $Z_2(\omega)$, and $Z_0(\omega)$, we find that

$$\begin{aligned} Z(\omega) &= Z_1(\omega) + \frac{1}{1/Z_2(\omega) + 1/Z_0(\omega)} \\ &= Z_1(\omega) + \frac{Z_2(\omega) + Z_0(\omega)}{Z_2(\omega)Z_0(\omega)}, \end{aligned} \tag{B.1}$$

but since this is also equal to $Z_0(\omega)$, we can solve

$$Z_0(\omega) = Z_1(\omega) + \frac{Z_2(\omega) + Z_0(\omega)}{Z_2(\omega)Z_0(\omega)} \tag{B.2}$$

for the characteristic impedance $Z_0(\omega)$ of the infinite network, resulting in

$$Z_0(\omega) = \frac{Z_1(\omega)}{2} + \frac{1}{2}\sqrt{Z_1^2(\omega) + 4Z_1(\omega)Z_2(\omega)}. \tag{B.3}$$

If we consider now the special case where $Z_1(\omega) = i\omega L$ and $Z_2(\omega) = (i\omega C)^{-1}$, we obtain

$$Z_0(\omega) = \frac{1}{2}\left(i\omega L + \sqrt{-\omega^2 L^2 + 4\frac{L}{C}}\right). \tag{B.4}$$

APPENDIX C: SOLUTION TO THE DECOUPLED TRANSMISSION LINE PROBLEM

In order to solve the decoupled transmission line problem, we utilize a method developed by Lieb, Schultz, and Mattis [96] to solve models of semi-infinite antiferromagnetic linear chains with nearest neighbor interactions.

Consider the Hamiltonian in second quantization form (up to a constant term) of a decoupled transmission line connected to a gate capacitance C_g

$$\begin{aligned} H &= \frac{\hbar\omega}{2}\Big\{ -\sum_{i=0}^{\infty}(\hat{a}_i^\dagger\hat{a}_{i+1}+\hat{a}_{i+1}^\dagger\hat{a}_i) - \sum_{i=0}^{\infty}(\hat{a}_i^\dagger\hat{a}_{i+1}^\dagger+\hat{a}_i\hat{a}_{i+1}+\frac{1}{2}\sum_{i=1}^{\infty}(\hat{a}_i^\dagger\hat{a}_i^\dagger+\hat{a}_i\hat{a}_i) \\ &\quad +\frac{1}{2}(1-\lambda)(\hat{a}_0^\dagger\hat{a}_0^\dagger+\hat{a}_0\hat{a}_0)+3\sum_{i=1}^{\infty}\hat{a}_i^\dagger\hat{a}_i+(1+\lambda)\hat{a}_0^\dagger\hat{a}_0\Big\}, \end{aligned} \tag{C.1}$$

where $\lambda = C_{ti}/C_{gi}$. We would like to rewrite it as a Hamiltonian of the form

$$H = \sum_{ij} A_{ij}(\hat{a}_i^\dagger\hat{a}_j+\hat{a}_j^\dagger\hat{a}_i)+\sum_{ij}\frac{1}{2}B_{ij}(\hat{a}_i^\dagger\hat{a}_j^\dagger+\hat{a}_i\hat{a}_j), \tag{C.2}$$

in units such that $\bar{\omega}/2 = 1$. If $\hat{a}_i$ and $\hat{a}_j$ are bosonic operators. A and B must be real symmetric matrices

$$A_{ij} = \begin{cases} 1+\lambda, & j=i=0 \\ 3, & j=i>0 \\ -1, & j>i\geq 0 \end{cases}, \tag{C.3}$$

$$B_{ij} = \begin{cases} 1-\lambda, & j=i=0 \\ 1, & j=i>0 \\ -1, & j>i\geq 0 \end{cases}, \tag{C.4}$$

and $[\hat{a}_i,\hat{a}_j]=\delta_{ij}$. We define now the matrix M as

$$M = \begin{pmatrix} A & B \\ B & A \end{pmatrix}. \tag{C.5}$$

Let

$$\eta M = \begin{pmatrix} A & B \\ -B & -A \end{pmatrix}. \tag{C.6}$$

We wish to find the matrix T such that $T\eta T^{\dagger}\eta = I$, or equivalently, $T\eta M T^{-1} = \Omega$ where Ω is diagonal. If

$$v_n = \begin{pmatrix} g_n \\ h_n \end{pmatrix} \tag{C.7}$$

and

$$w_n = \begin{pmatrix} h_n^* \\ g_n^* \end{pmatrix}, \tag{C.8}$$

we can have

$$\eta M \cdot v_n = \omega_n v_n \tag{C.9}$$

$$\eta M \cdot w_n = -\omega_n w_n, \tag{C.10}$$

for $\omega_n > 0$. Let then

$$\begin{pmatrix} A & B \\ -B & -A \end{pmatrix} \begin{pmatrix} g_n \\ h_n \end{pmatrix} = \omega_n \begin{pmatrix} g_n \\ h_n \end{pmatrix}. \tag{C.11}$$

Rewriting Eq. (C.11) as a system of two equations, we obtain

$$Ag_n + Bh_n = \omega_n g_n \tag{C.12}$$

$$-Bg_n - Ah_n = \omega_n h_n, \tag{C.13}$$

which can be rearranged into

$$A(g_n - h_n) - B(g_n - h_n) = \omega_n(g_n + h_n) \tag{C.14}$$

$$A(g_n + h_n) + B(g_n + h_n) = \omega_n(g_n - h_n). \tag{C.15}$$

We can then define

$$\psi_n \equiv g_n - h_n \tag{C.16}$$

$$\phi_n \equiv g_n + h_n, \tag{C.17}$$

and insert them in Eq. (C.11), resulting in

$$\begin{aligned} (A - B)\phi_n &= \omega_n^2 \phi_n \\ (A + B)\psi_n &= \omega_n^2 \psi_n, \end{aligned} \tag{C.18}$$

After some algebra, we find

$$\begin{aligned} (A - B)(A + B)\phi_n &= \omega_n^2 \phi_n \\ (A + B)(A - B)\psi_n &= \omega_n^2 \psi_n, \end{aligned} \tag{C.19}$$

where

$$(A+B)_{ij} = \begin{cases} 2, & j = i = 0 \\ 4, & j = i > 0 \\ -2, & j > i \geq 0 \end{cases}, \tag{C.20}$$

$$(A-B)_{ij} = \begin{cases} 2\lambda - \lambda, & j = i = 0 \\ 2, & j = i > 0 \\ 0, & j > i \geq 0 \end{cases}, \tag{C.21}$$

Omitting the index n for the sake of simplicity, we shall now attempt to find a phase shift solution of the type

$$\sum_j [(A+B)(A-B)]_{ij}\varphi(j) = \omega^2\varphi(i), \tag{C.22}$$

where

$$\begin{aligned}[(A+B)(A-B)]_{ij} &= \sum_k [(A+B)_{ik}(A-B)]_{kj} \\ &= [(A+B)_{ij}(A-B)]_{jj} \end{aligned} \tag{C.23}$$

and only the $j = i \pm 1$ (nearest neighbor) terms and $j = i$ contribute in the sum. If we use the Ansatz

$$\varphi(j) = \begin{cases} a\cos(kj+\delta), & \text{if } j > 0 \\ b, & \text{if } j = 0 \end{cases}, \tag{C.24}$$

in Eq. (C.22), we have for $i = 0$

$$\omega^2\varphi(0) = \sum_{i=0}^{N}(A+B)_{0i}(A-B)_{ii}\varphi(i) \tag{C.25}$$

$$= (A+B)_{00}(A-B)_{00}\varphi(0) + \sum_{i=1}^{N}(A+B)_{0i}(A-B)_{ii}\varphi(i) \tag{C.26}$$

$$\omega^2 b = 4\lambda\varphi(0) - 4\varphi(1). \tag{C.27}$$

Similarly, we obtain

$$\begin{aligned}\omega^2\varphi(1) &= -4\lambda\varphi(0) + 8\varphi(1) - 4\varphi(2) \\ \omega^2 a\cos(kj+\delta) &= -4\lambda b + 8a\cos(kj+\delta) - 4a\cos(2kj+\delta)\end{aligned} \tag{C.28}$$

and

$$\omega^2\varphi(2) = -4\varphi(1) + 8\varphi(2) - 4\varphi(3), \tag{C.29}$$

for $i = 1$ and $i = 2$, respectively. The equations for $i > 2$ present the same form of Eq. C.29. From the same equation, we obtain

$$\omega^2 a \cos(kj + \delta) = -4a \cos(kj - k + \delta) + 8a \cos(kj + \delta) - 4a \cos(kj + k + \delta), \quad \text{(C.30)}$$

which after some algebra and trigonometric identities can be solved for ω

$$\omega^2 \cos(kj + \delta) = 8 \cos(kj + \delta)[1 - \cos(k)], \quad \text{(C.31)}$$

$$\omega^2 = 16 \left[\frac{1 - \cos(k)}{2}\right], \quad \text{(C.32)}$$

resulting in the dispersion relation

$$\omega = 4 \sin\left(\frac{k}{2}\right). \quad \text{(C.33)}$$

Using this result in Eq. (C.28), we obtain after some algebraic manipulation

$$\lambda\left(\frac{b}{a}\right) = \cos\delta, \quad \text{(C.34)}$$

which can be plugged into Eq. (C.29) to give the transcendental equation

$$\frac{2\cos\delta}{\lambda} - \cos\delta - \frac{2\cos k \cos\delta}{\lambda} = \sin k \sin\delta - \cos k \cos\delta. \quad \text{(C.35)}$$

It is easy to see that for the trivial case $\lambda = 1$

$$\cos\delta = \cos(k - \delta), \quad \text{(C.36)}$$

which has the solution $\delta = k/2$.

APPENDIX D: NUMERICAL CALCULATIONS OF THE INTERCAPACITIVE COUPLING C_{12}

We present here the numerical calculations to estimate the capacitive coupling C_{12} existing between the quantum dot plunger leads, as shown in Fig. 4.1. For these calculations, we made use of numerical multipole expansion calculations performed by FastCap fast field solver software [95]. We used as input a set of 5 long electrodes and two shorter plunger gates alternated in between them, representing the gate setup for the DQD. The electrodes were assumed to have a 30 nm $\times$60 nm cross section, and several simulations were run for different electrode lengths, ranging from $\sim$ 1 through 10 μm. We show below in Fig. D.1 a schematic representation of the electrodes that gate the double quantum dot setup.

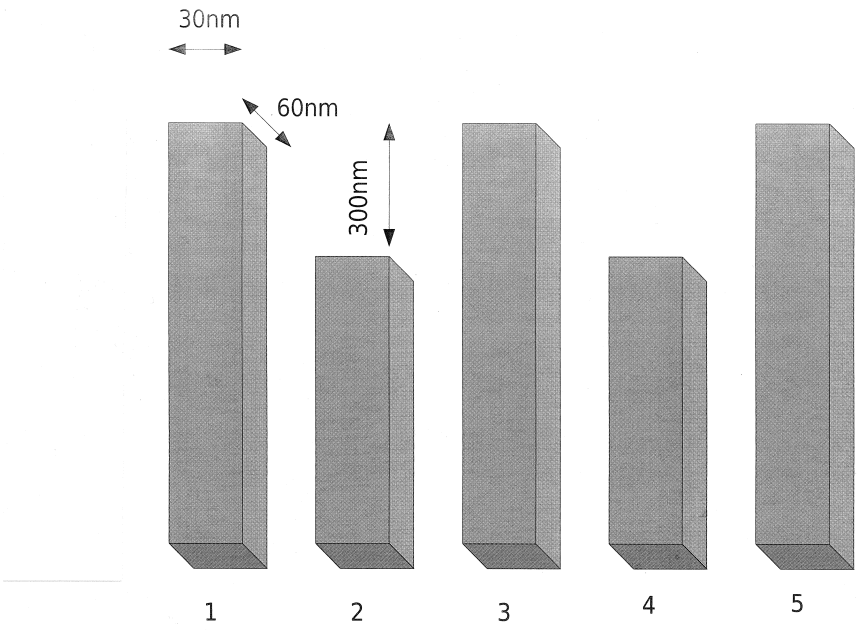

Figure D.1: Design of the electrodes in the double quantum dot system.

We present below in Fig. D.2 a snapshot of the output of the FastCap capacitance

calculations. We made use of a multipole expansion up to fourth order to obtain these results. The output is a capacitance matrix that depicts the capacitance of each electrode in the main diagonal, and the capacitive couplings between each pair of electrodes as off-diagonal elements. We are mainly interested in the calculation of the capacitive coupling between electrodes 2 and 4, as shown in Fig. D.1, and for an electrode length of $\simeq 10$ μm. This is C_{12} in our model, and its value corresponds to $\simeq 20$ aF as seen in the capacitance matrix in Fig. D.2.

```
      number of extra evaluation points: 0
      translation: (0 1.2e-07 0)
    GROUP4
     sgate.qui, conductor
      title: `6e-08mX3e-08mX1.02e-05m cube (n=3 e=0.1)'
      outer permittivity: 1
      number of panels: 3708
      number of extra evaluation points: 0
      translation: (0 1.8e-07 0)
    GROUP5
     lgate.qui, conductor
      title: `6e-08mX3e-08mX1.05e-05m cube (n=3 e=0.1)'
      outer permittivity: 1
      number of panels: 3816
      number of extra evaluation points: 0
      translation: (0 2.4e-07 0)
  Date: Thu Oct 11 17:21:38 2007
  Host: scyld.ucf.edu

INPUT SUMMARY
  Expansion order: 4
  Number of partitioning levels: 8
  Overall permittivity factor: 1
  Total number of panels: 18864
    Number of conductor panels: 18864
    Number of dielectric interface panels: 0
    Number of thin conductor on dielectric interface panels: 0
  Number of conductors: 5
No expansions at level 8 (lowest)
Percentage of multiplies done by multipole: 96.4%

ITERATION DATA
Starting on column 1 (1%GROUP1)
1 2 3 4 5 6 7 8 9
Starting on column 2 (1%GROUP2)
1 2 3 4 5 6 7 8
Starting on column 3 (1%GROUP3)
1 2 3 4 5 6 7 8 9
Starting on column 4 (1%GROUP4)
1 2 3 4 5 6 7 8
Starting on column 5 (1%GROUP5)
1 2 3 4 5 6 7 8 9

CAPACITANCE MATRIX, attofarads
                    1          2          3          4          5
1%GROUP1 1      396.6     -281.8     -32.34     -16.31      -23.7
1%GROUP2 2     -281.8      597.2     -263.2     -19.57     -16.39
1%GROUP3 3     -32.34     -263.2      607.7     -263.3     -32.36
1%GROUP4 4     -16.31     -19.57     -263.3        597     -281.6
1%GROUP5 5      -23.7     -16.39     -32.36     -281.6      396.5
[dcastelo@scyld bin]$
```

Figure D.2: Simulation results for the mutual capacitances among the electrodes in the double quantum dot system.

LIST OF REFERENCES

[1] R. Landauer, *Irreversibility and heat generation in the computing process*, IBM J. Res. Dev. **5**, 183 (1961).

[2] C. H. Bennett, *Logical reversibility of computation*, IBM J. Res. Dev. **17**, 6 (1973).

[3] T. Toffoli, *Conservative Logic*, Technical Report MIT/LCS/TM-151 (1980).

[4] E. Fredkin and T. Toffoli, *Conservative Logic*, Int. J. Theor. Phys. **21**, 3/4 (1982).

[5] R. P. Feynman, *Simulating physics with computers*, International Journal of Theoretical Physics **21**, 467 (1982).

[6] R. P. Feynman, *The Feynman Lectures on Computation*, edited by R.W. Allen and T. Hey (Perseus Publishing, 2000).

[7] S. Lloyd, *Universal quantum simulators*, Science **273**, 1073 (1996).

[8] R. P. Feynman, *Quantum Mechanical Computers*, Opt. News **11**, 11 (1985).

[9] J. Preskill, *Quantum Computation*, Lecture notes (Caltech, 1999).

[10] M. A. Nielsen and I. L. Chuang, *Quantum Computation and Quantum Information* (Cambridge University Press, Cambridge, U.K., 2000).

[11] *Lectures on Quantum Information*, edited by D. Bruβ and G. Leuchs (Wiley-VCH, Germany, 2007).

[12] G. Benenti, G. Casati, and G. Strini *Principles of Quantum Computation and Information* vols. I and II (World Scientific Publishing Company, Singapore, 2004 and 2007).

[13] N. D. Mermin *Quantum Computer Science: An Introduction* (Cambridge University Press, U.K., 2007).

[14] A. Yu. Kitaev, A. H. Shen, M. N. Vyalyi *Classical and Quantum Computation*, Graduate Studies in Mathematics (American Mathematical Society, USA, 2002).

[15] *The Physics of Quantum Information: Quantum Cryptography, Quantum Teleportation, Quantum Computation*, edited by D. Bouwmeester, A. K. Ekert, and A. Zeilinger, (Springer, Germany, 2001).

[16] *Introduction to Quantum Computation and Information*, edited by H.-K. Lo, S. Popescu, and T. Spiller (World Scientific Publishing Company, Singapore, 2000).

[17] D. Deutsch, *Quantum theory, the Church-Turing principle and the universal quantum computer*, Proceedings of the Royal Society of London; Series A, Mathematical and Physical Sciences **400**, 1818, 97-117 (1985).

[18] P. W. Shor, *Algorithms for quantum computation: Discrete logarithms and factoring*, Proc. 35nd Annual Symposium on Foundations of Computer Science (Shafi Goldwasser, ed.), IEEE Computer Society Press, 124-134 (1994).

[19] L. K. Grover, *A fast quantum mechanical algorithm for database search*, Proceedings of the 28th Annual ACM Symposium on the Theory of Computing (STOC), 212-219 (1996).

[20] C. H. Bennett, F. Bessette, G. Brassard, L. Salvail and J. Smolin *Experimental Quantum Cryptography*, Journal of Cryptology **5**, 1, 3-28 (1992).

[21] Y. Aharonov, L. Davidovich, and N. Zagury, *Quantum random walks*, Phys. Rev. A, **48** (2):16871690 (1993).

[22] A. M. Childs, R. Cleve, E. Deotto, E. Farhi, S. Gutmann, and D. A. Spielman, *Exponential algorithmic speedup by quantum walk*, Proc. 35th ACM Symposium on Theory of Computing, pp. 5968, (2003).

[23] R. Liboff, *Introductory Quantum Mechanics*, 4th Edition (Addison-Wesley, 2002).

[24] A. Einstein, B. Podolsky, and N. Rosen, *Can quantum-mechanical description of reality be considered complete?*, Phys. Rev. **47**, 777 (1935).

[25] V. B. Braginsky and F. Y. Khalili, *Quantum Measurement* (Cambridge University Press, 1992).

[26] P. W. Shor, *Fault-tolerant quantum computation*, in Proceedings of 37th Annual Symposium on Foundations of Computer Science, **56** (IEEE Press, 1996).

[27] A. M. Steane, *Error correction codes in quantum information processing*, Phys. Rev. Lett. **77**, 793 (1996).

[28] D. Aharonov and M. Ben-Or, *Fault-tolerant quantum computation with constant error*, in Proceedings of the 29th Annual ACM Symposium on the Theory of Computation (STOC), 176188 (ACM Press, New York, New York, 1996).

[29] A. Y. Kitaev, *Quantum error correction with imperfect gates*, in Quantum Communication, Computing, and Measurement, edited by A.S. Holevo, O.Hirota and C.M. Caves, 181 (Springer, 1997).

[30] A. Y. Kitaev, *Quantum computations: Algorithms and error correction* Russian Math. Surveys **52**, 11911249 (1997).

[31] D. Gottesman, *Stabilizer Codes and Quantum Error Correction*, PhD thesis, Calif. Inst. Tech, Pasadena, California, (1997).

[32] J. Preskill, *Reliable quantum computers*, Proc. R. Soc. Lond. A **454**, 385410 (1998).

[33] E. Knill, R. Laflamme, and W. H. Zurek, *Resilient quantum computation*, Science **279**, 342345 (1998).

[34] D. Aharonov and M. Ben-Or, *Fault-tolerant quantum computation with constant error rate*, SIAM J. Comput. **38**, 4, 1207-1282 (1999).

[35] A. M. Steane, *Overhead and noise threshold of fault-tolerant quantum error correction*, Phys. Rev. A **68**, 042322 (2003).

[36] *Semiconductor Spintronics and Quantum Computation*, edited by D. D. Awschalom, D. Loss, and N. Samarth, (Springer, Berlin, 2002).

[37] D. Loss and D. P. DiVincenzo, *Quantum computation with quantum dots*, Phys. Rev. A **57**, 120 (1998).

[38] R. H. Blick and H. Lorenz, in *Possible definition of quantum bits in coupled quantum dots*, *Proceedings of the IEEE International Symposium on Circuits and Systems*, edited by J. Calder (IEEE, Piscataway, NJ, 2000), Vol. II, p. 245.

[39] D. P. DiVincenzo, D. Bacon, J. Kempe, G. Burkhard, and K. B. Whaley, *Universal quantum computation with the exchange interaction*, Nature (London) **408**, 339, (2000).

[40] J. R. Petta, A. C. Johnson, J. M. Taylor, E. A. Laird, A. Yacoby, M. D. Lukin, C. M. Marcus, M. P. Hanson, and A. C. Gossard, *Coherent Manipulation of Coupled Electron Spins in Semiconductor Quantum Dots*, Science **309**, 2180 (2005).

[41] F. H. L. Koppens, C. Buizert, K. J. Tielrooij, I. T. Vink, K. C. Nowack, T. Meunier, L. P. Kouwenhoven, and L. M. K. Vandersypen, *Driven coherent oscillations of a single electron spin in a quantum dot*, Nature (London) **442**, 766 (2006).

[42] T. Tanamoto, *Quantum gates by coupled quantum dots and measurement procedure in Si MOSFET*, Physica B **272**, 45 (1999).

[43] T. Tanamoto, *Quantum gates by coupled asymmetric quantum dots and controlled-not-gate operation*, Phys. Rev. A **61**, 022305 (2000).

[44] T. Hayashi, T. Fujisawa, H. D. Cheong, Y. H. Jeong, and Y. Hirayama, *Coherent Manipulation of Electronic States in a Double Quantum Dot*, Phys. Rev. Lett. **91**, 226804 (2003).

[45] T. Fujisawa, T. Hayashi, H. D. Cheong, Y. H. Jeong, and Y. Hirayama, *Rotation and phase-shift operations for a charge qubit in a double quantum dot*, Physica E **21**, 1046 (2004).

[46] J. R. Petta, A. C. Johnson, C. M. Marcus, M. P. Hanson, and A. C. Gossard, *Manipulation of a Single Charge in a Double Quantum Dot*, Phys. Rev. Lett. **93**, 186802 (2004).

[47] J. Gorman, E. G. Emiroglu, D. G. Hasko, and D. A. Williams, *Charge-Qubit Operation of an Isolated Double Quantum Dot*, Phys. Rev. Lett. **95**, 090502 (2005).

[48] L. C. L. Hollenberg, A. S. Dzurak, C. Wellard, A. R. Hamilton, D. J. Reilly, G. J. Milburn, and R. G. Clark, *Charge-based quantum computing using single donors in semiconductors*, Phys. Rev. B **69**, 113301 (2004).

[49] S. E. S. Andresen, R. Brenner, C. J. Wellard, C. Yang, T. Hopf, C. C. Escott, R. G. Clark, A. S. Dzurak, D. N. Jamieson, and L. C. L. Hollenberg, *Charge State Control and Relaxation in an Atomically Doped Silicon Device* , Nano Lett. **7**, 2000 (2007).

[50] J. Levy, *Universal Quantum Computation with Spin-1/2 Pairs and Heisenberg Exchange*, Phys. Rev. Lett. **89**, 147902 (2002).

[51] Y. S. Weinstein and C. S. Hellberg, *Energetic suppression of decoherence in exchange-only quantum computation*, Phys. Rev. A **72**, 022319 (2005).

[52] Y. S. Weinstein and C. S. Hellberg, *Scalable Architecture for Coherence-Preserving Qubits*, Phys. Rev. Lett. **98**, 110501 (2007).

[53] Yu. A. Pashkin, T. Yamamoto, O. Astafiev, Y. Nakamura, D. V. Averin, and J. S. Tsai, *Quantum oscillations in two coupled charge qubits*, Nature (London) **421**, 823 (2003).

[54] D. Vion, A. Aassime, A. Cottet, P. Joyez, H. Pothier, C. Urbina, D. Estève, and M. H. Devoret, *Manipulating the Quantum State of an Electrical Circuit*, Science **296**, 886 (2002).

[55] A. Blais, J. Gambetta, A. Wallraff, D. I. Schuster, S. M. Girvin, M. H. Devoret, and R. J. Schoelkopf, *Quantum-information processing with circuit quantum electrodynamics*, Phys. Rev. A **75**, 032329 (2007).

[56] J. Koch, T. M. Yu, J. Gambetta, A. A. Houck, D. I. Schuster, J. Majer, A. Blais, M. H. Devoret, S. M. Girvin, R. J. Schoelkopf, *Charge-insensitive qubit design derived from the Cooper pair box*, Phys. Rev. A **76**, 042319 (2007).

[57] L. Fedichkin, M. Yanchenko, and K. A. Valiev, *Coherent charge qubits based on GaAs quantum dots with a built-in barrier*, Nanotechnology **11**, 387 (2000).

[58] L. Fedichkin and A. Fedorov, *Error rate of a charge qubit coupled to an acoustic phonon reservoir*, Phys. Rev. A **69**, 032311 (2004).

[59] T. Brandes and T. Vorrath, *Adiabatic transfer of electrons in coupled quantum dots*, Phys. Rev. B **66**, 075341 (2002).

[60] S. Vorojtsov, E. R. Mucciolo, and H. U. Baranger, *Phonon decoherence of a double quantum dot charge qubit*, Phys. Rev. B **71**, 205322 (2005).

[61] Z.-J. Wu, K.-D. Zhu, X.-Z. Yuan, Y.-W. Jiang, and H. Zheng, *Charge qubit dynamics in a double quantum dot coupled to phonons*, Phys. Rev. B **71**, 205323 (2005).

[62] V. N. Stavrou and X. Hu, *Charge decoherence in laterally coupled quantum dots due to electron-phonon interactions*, Phys. Rev. B **72**, 075362 (2005).

[63] A. C. Johnson, J. R. Petta, J. M. Taylor, A. Yacoby, M. D. Lukin, C. M. Marcus, M. P. Hanson, and A. C. Gossard, *Triplet-singlet spin relaxation via nuclei in a double quantum dot*, Nature (London) **435**, 925 (2005).

[64] J. M. Taylor, J. R. Petta, A. C. Johnson, A. Yacoby, C. M. Marcus, and M. D. Lukin, *Relaxation, dephasing, and quantum control of electron spins in double quantum dots*, Phys. Rev. B **76**, 035315 (2007).

[65] J. Kempe, D. Bacon, D. A. Lidar, and K. B. Whaley, *Theory of decoherence-free fault-tolerant universal quantum computation*, Phys. Rev. A **63**, 042307 (2001).

[66] D. K. L. Oi, S. G. Schirmer, A. D. Greentree, and T. M. Stace, *Robust charge-based qubit encoding*, Phys. Rev. B **72**, 075348 (2005).

[67] M. Thorwart, J. Eckel, and E. R. Mucciolo, *Non-Markovian dynamics of double quantum dot charge qubits due to acoustic phonons*, Phys. Rev. B **72**, 235320 (2005).

[68] M. J. Storcz, U. Hartmann, S. Kohler, and F. K. Wilhelm, *Intrinsic phonon decoherence and quantum gates in coupled lateral quantum-dot charge qubits*, Phys. Rev. B **72**, 235321 (2005).

[69] U. Hohenester, *Optimal quantum gates for semiconductor qubits*, Phys. Rev. B **74**, 161307R (2006).

[70] I. O. Kulik, T. Hakioğlu, and A. Barone, *Quantum computational gates with radiation free couplings*, Eur. Phys. J. B **30**, 219 (2002).

[71] P. N. Argyres and P. L. Kelley, *Theory of Spin Resonance and Relaxation*, Phys. Rev. **134**, A98 (1964).

[72] M. Korkusinski, I. P. Gimenez, P. Hawrylak, L. Gaudreau, S. A. Studenikin, and A. S. Sachrajda, *Topological Hunds rules and the electronic properties of a triple lateral quantum dot molecule*, Phys. Rev. B **75**, 115301 (2007).

[73] F. Delgado, Y.-P. Shim, M. Korkusinski, and P. Hawrylak, *Theory of spin, electronic, and transport properties of the lateral triple quantum dot molecule in a magnetic field*, Phys. Rev. B **76**, 115332 (2007).

[74] J. E. Mooij, T. P. Orlando, L. Levitov, L. Tian, C. H. van der Wal, and S. Lloyd, *Josephson Persistent-Current Qubit*, Science **285**, 1036 (1999).

[75] L. Tian and P. Zoller, *Quantum computing with atomic Josephson junction arrays*, Phys. Rev. A **68**, 042321 (2003).

[76] J. R. Schrieffer and P. A. Wolff, *Relation between the Anderson and Kondo Hamiltonians*, Phys. Rev. **149**, 491 (1966).

[77] N. Schuch and J. Siewert, *Natural two-qubit gate for quantum computation using the XY interaction*, Phys. Rev. A **67**, 032301 (2003).

[78] E. R. Mucciolo, S. Vorojtsov, and H. U. Baranger, in *Phonon decoherence in quantum dot qubits*, *Quantum Information and Computation III*, edited by E. J. Donkor, A. R. Pirich, and H. E. Brandt, Proceedings of the SPIE **5815**, 53 (2005).

[79] A. J. Leggett, S. Chakravarty, A. T. Dorsey, M. P. A. Fisher, A. Garg, and W. Zwerger, *Dynamics of the dissipative two-state system*, Rev. Mod. Phys. **59**, 1 (1987).

[80] W. T. Pollard and R. A. Friesner, *Solution of the Redfield equation for the dissipative quantum dynamics of multilevel systems*, J. Chem. Phys. **100**, 5054 (1994).

[81] H. Bruus, K. Flensberg, and H. Smith, *Magnetoconductivity of quantum wires with elastic and inelastic scattering*, Phys. Rev. B **48**, 11144 (1993).

[82] C. P. Slichter, *Principles of Magnetic Resonance*, 3rd. edition (Springer, Berlin, 1996).

[83] U. Weiss, *Quantum Dissipative Systems* (World Scientific, Singapore, 1999), Sec. 21.5.2.

[84] W. G. van der Wiel, S. De Franceschi, J. M. Elzerman, T. Fujisawa, S. Tarucha, and L. P. Kouwenhoven, *Electron transport through double quantum dots*, Rev. Mod. Phys. Vol. **75**, 1 (2003).

[85] L. P. Kouwenhoven, C. M. Marcus, P. L. McEuen, S. Tarucha, R. M. Westervelt, and N. S. Wingreen, *Electron Transport in Quantum Dots*, Nato ASI conference proceedings, ed. by L. P. Kouwenhoven, G. Schon, and L.L. Sohn (Kluwer, Dordrecht, 1997).

[86] G.-L. Ingold and Yu. V. Nazarov, *Charge Tunneling Rates in Ultrasmall Junctions*, in: *Single Charge Tunneling*, ed. by H. Grabert and M. H. Devoret, NATO ASI Series B, Vol. 294, p. 21107 (Plenum, 1992).

[87] R. Feynman, R. B. Leighon, and M. L. Sands, *The Feynman Lectures on Physics, Commemorative Issue* Vol 2 (Addison-Wesley, Reading, MA, 1964 & 1989).

[88] R. Kubo, *The fluctuation-dissipation theorem*, Rep. Prog. Phys. **29**, 255-284 (1966).

[89] R. Hanson, *Electron spins in semiconductor quantum dots*, Ph.D. thesis, Delft University of Technology, 2005.

[90] N. W. Ashcroft and N. D. Mermin, *Solid State Physics* (Brooks Cole, USA, 1976).

[91] C. W. J. Beenakker and H. van Houten, *Quantum Transport in Semiconductor Nanostructures*, Solid State Physics, **44**, 1, 228 (1991).

[92] J. B. Kycia, J. Chen, R. Therrien, Ç. Kurdak, K. L. Campman, A. C. Gossard, and John Clarke, *Effects of Dissipation on a Superconducting Single Electron Transistor*, Phys. Rev. Lett. **87**, 017002 (2001).

[93] E. B. Rosa and F. W. Grover, *Formulas and Tables for the Calculation of Mutual and Self Induction [Revised]*, Bulletin of the National Bureau of Standards, Vol 8, No. 1, Section 8, pages 150 - 166 (USA, 1912).

[94] C. W. J. Beenakker, *Theory of Coulomb-blockade oscillations in the conductance of a quantum dot*, Phys. Rev. B **44**, 1646-1656 (1991).

[95] E. di Lorenzo, FastCap 2 software, MIT Research Lab of Electronics, Cambridge, MA, 1992.

[96] E. Lieb, T. Schultz, and D. Mattis, *Two soluble models of an antiferromagnetic chain*, Annals of Physics **16**, 407 (1961).

[97] P. Cedraschi and M. Büttiker, *Quantum Coherence of the Ground State of a Mesoscopic Ring*, Annals of Physics **289**, 1 (2001).

[98] K. Le Hur, *Coulomb Blockade of a Noisy Metallic Box: A Realization of Bose-Fermi Kondo Models*, Phys. Rev. Lett. **92**, 196804 (2004).

[99] M. Li and K. Le Hur, *Double-Dot Charge Qubit and Transport via Dissipative Cotunneling*, Phys. Rev. Lett. **93**, 176802 (2004).

[100] M. Hentschel, D. C. B. Valente, E. R. Mucciolo, and H. U. Baranger, *Improving intrinsic decoherence in multiple-quantum-dot charge qubits*, Phys. Rev. B **76**, 235309 (2007).

[101] E. Paladino, L. Faoro, G. Falci, and R. Fazio, *Decoherence and* $1/f$ *Noise in Josephson Qubits*, Phys. Rev. Lett. **88**, 228304 (2002).

[102] Y. M. Galperin, B. L. Altshuler, and D. V. Shantsev, *Non-Gaussian Low-Frequency Noise as a Source of Qubit Decoherence*, Phys. Rev. Lett. **96**, 097009 (2006).

[103] L. Faoro, J. Bergli, B. L. Altshuler, and Y. M. Galperin, *Models of Environment and T_1 Relaxation in Josephson Charge Qubits*, Phys. Rev. Lett. **95**, 046805 (2005).

[104] A. Grishin, I. V. Yurkevich, and I. V. Lerner, *Low-temperature decoherence of qubit coupled to background charges*, Phys. Rev. B **72**, 060509(R) (2005).

[105] R. de Sousa, K. B. Whaley, F. K. Wilhelm, and J. von Delft, *Ohmic and Step Noise from a Single Trapping Center Hybridized with a Fermi Sea*, Phys. Rev. Lett. **95**, 247006 (2005).

[106] Y. M. Galperin, B. L. Altshuler, J. Bergli, and D. V. Shantsev, *Non-Gaussian Low-Frequency Noise as a Source of Qubit Decoherence*, Phys. Rev. Lett. **96**, 097009 (2006).

[107] S. Montangero, T. Calarco, and R. Fazio, *Robust Optimal Quantum Gates for Josephson Charge Qubits*, Phys. Rev. Lett. **99**, 170501 (2007).

[108] E. Paladino, M. Sassetti, G. Falci, and U. Weiss, *Characterization of coherent impurity effects in solid-state qubits*, Phys. Rev. B **77**, 041303(R) (2008).

[109] B. Abel and F. Marquardt, *Decoherence by quantum telegraph noise: A numerical evaluation*, Phys. Rev. B **78**, 201302(R) (2008).

[110] Y. A. Pashkin, O. Astafiev, T. Yamamoto, Y. Nakamura, and J. S. Tsai, *Josephson charge qubits: a brief review*, Quantum Inf. Process. **8**, 55 (2009).

[111] I. V. Yurkevich, J. Baldwin, I. V. Lerner, and B. L. Altshuler, *Decoherence of charge qubit coupled to interacting background charges*, preprint arXiv:0909.4952v1 (2009).